

Search for Heavy Neutral Leptons with LHCb

Présentée le 22 septembre 2023

Faculté des sciences de base
Laboratoire de physique des hautes énergies LS
Programme doctoral en physique

pour l'obtention du grade de Docteur ès Sciences

par

Serhii CHOLAK

Acceptée sur proposition du jury

Prof. R. Houdré, président du jury
Prof. L. Shchutska, directrice de thèse
Prof. S. Lowette, rapporteur
Prof. X. Cid Vidal, rapporteur
Prof. L. Caminada, rapporteuse

I am dedicating this thesis to the brave men and women of Ukraine, who are sacrificing their
lives to defend my homeland and keep my family safe...

Acknowledgements

When signing the contract for this PhD with the end date in 2023, it sounded tremendously long back then. Yet here we are, at the end of my journey with the LPHE laboratory at EPFL, which would not be even a half-great without the people that I met here. I would like to thank the people on whose shoulders are standing the particle physics at EPFL and the LPHE group: Lesya Shchutska, Olivier Schneider, Aurelio Bay, Tatsuya Nakada, Frédéric Blanc, Radoslav Marchevski and Guido Hafaedi. A separate word for my supervisor, Prof. Lesya Shchutska, whose hard work and scientific achievements made it possible to open this PhD project. With constant support, scientific input, and yet plenty of freedom, I enjoyed performing this challenging work with Lesya. A big thank you also belongs to Guido for kindly letting me work with him on the hardware projects and introducing me to the subject. I had the great pleasure of sharing my analysis work with the postdocs from the LHCb collaboration: Martino Borsato, to whom I would always go with the technical puzzles, Fede, who would nobly fight for our analysis at the working group meetings, and Louis Henry, who was of great help towards the end of my thesis. I am also very grateful to Maarten, who was an excellent supervisor during the summer school and then came to work at EPFL as well to supervise me just a bit more :) Esther and Corinne were always helpful, cheerful and were organising awesome lab events. I was happy to share the burden of this "tough" PhD life with my comrades-students and postdocs of the previous, my and the next generation, who made the atmosphere in our lab so joyful. I was extremely lucky to start and finish my PhD with colleagues who became friends: Sara and Carina, who would always be there for me. Of course, I should also mention my dear friends, Pavol, Lino, Vlado, Veronica and Elena. Then Matt, Sonia and Guillaume, the best next-door officemates, would always teach me a bit of French. And surely, it would not be that much fun without Paul, Anna, Seb, Marie, Ettore, Maria, Anni, Ana Bárbara, Raphael, Dimitris, Fede, Arvind and Surapat. Special thanks also to my local Ukrainian friends: Mykyta, Sasha, Artem, Mykhailo and Andrii, for all the fun activities in the area.

Frankly, I am not in possession of such words to describe how grateful I am to my wonderful wife, Valeriia, who always supported me in our common journey in physics and life. I think the toughest part of this PhD was that Lausanne is so far away from Paris, from you.

Last but not least, I would like to thank my family for the amount of love and support I grew up with. Although I went that far away from my home, you are always here with me, in my heart. Дякую!

Abstract

This thesis presents a search for a beyond the Standard Model (SM) heavy neutral lepton (HNL), which does not interact via any of the SM interactions. This hypothetical particle has been proposed by multiple theories as an extension to the SM, and it could solve one or several experimental puzzles of the modern high energy physics. The search is done using the dataset collected by the LHCb experiment during the years 2016-2018, corresponding to an integrated luminosity of 5.0 fb^{-1} . Its signature consists in a heavy neutrino decaying to $\mu^\pm \pi^\mp$ final state, while the heavy neutrino is produced in B meson decays to $\mu^\pm N$ or $\mu^\pm NX$, where X is not reconstructed. Results of this research work are presented as the limit on the mixing parameter $|U_\mu|^2$ between the HNL and the SM muon neutrino as a function of the HNL mass and lifetime that were considered. It improves the previous LHCb result by more than one order of magnitude, and is being competitive with the world-best limit. Additionally, this manuscript describes a contribution to the development, commissioning and operation of the PLUME luminometer. This is a new subdetector of the LHCb experiment, which is dedicated to the luminosity measurement and is crucial for the operation of the detector.

Keywords: particle physics, LHCb, LHC, heavy neutral lepton, HNL, PLUME

Résumé

Cette thèse présente la recherche d'un lepton lourd neutre (HNL) au-delà du modèle standard (SM), et n'étant régi par aucune des interactions fondamentales. Cette particule hypothétique a été proposée par de nombreuses théories comme une extension du SM, qui pourrait justifier certaines observations expérimentales en physique moderne des particules, jusqu'alors inexpliquées. Cette recherche est effectuée à partir de l'ensemble des données collectées par l'expérience LHCb au cours des années 2016-2018, correspondant à une luminosité intégrée de 5.0 fb^{-1} . Sa signature est composée d'un neutrino lourd se désintégrant en $\mu^\pm \pi^\mp$, et produit à partir de désintégrations de mésons B en $\mu^+ N$ ou $\mu^+ NX$, où X n'est pas reconstruit. Les résultats de ce travail de recherche sont présentés sous forme de la limite du paramètre de mélange $|U_\mu|^2$ entre le HNL et le neutrino muonique SM en fonction de la masse et de la durée de vie du HNL correspondantes. Ce résultat apporte une amélioration de plus d'un ordre de grandeur par rapport à la mesure précédente de LHCb, et est compétitif avec la meilleure limite mondiale actuelle. De plus, ce manuscrit décrit une contribution au développement, à la mise en service et à l'exploitation du luminomètre PLUME. Il s'agit d'un nouveau sous-détecteur de l'expérience LHCb, dédié à la mesure de la luminosité et crucial pour le fonctionnement du détecteur.

Mots-clés : physique des particules, LHCb, LHC, lepton neutre lourd, HNL, PLUME

Абстракт

Ця дисертація присвячена пошуку важкого нейтрального лептона (ВНЛ), який виходить за межі Стандартної моделі (СМ) і не взаємодіє із жодною із взаємодій, які описує ця теорія. Ця гіпотетична частинка була запропонована багатьма теоріями-доповненнями до стандартної моделі, які могли б вирішити одну або декілька експериментальних проблем сучасної фізики високих енергій. Пошук здійснено в даних, зібраних експериментом LHCb протягом 2016-2018 років, відповідаючих інтегральній світності 5.0 fb^{-1} . Досліджуваний розпад складається з важкого нейтрино, що розпадається на $\mu^\pm \pi^\mp$, при чому саме нейтрино утворюється у розпаді B мезона на $\mu^+ N$ або $\mu^+ NX$, де X не реконструюється. Результати цієї дослідницької роботи представлено у вигляді обмеження на параметр змішування $|U_\mu|^2$ між ВНЛ і мюонним нейтрино стандартної моделі як функцію маси і часу життя ВНЛ. Це покращує попередній результат LHCb більш ніж на один порядок і конкурує з найкращою світовою межею. Крім того, цей рукопис описує внесок у розробку, введення в експлуатацію та підтримку роботи детектору PLUME. Це новий люмінометр, розроблений для експерименту LHCb, який призначений для вимірювання світності та має ключове значення для роботи детектора.

Ключові слова: фізика елементарних частинок, LHCb, ВНЛ, PLUME

Contents

| | |
|--|------------|
| Acknowledgements | i |
| Abstract (English/Français/Українська) | iii |
| Introduction | 1 |
| 1 Theory and experimental motivation | 3 |
| 1.1 General introduction to the Standard Model | 3 |
| 1.1.1 Neutrino in the SM | 4 |
| 1.1.2 Masses of the SM neutrinos | 5 |
| 1.2 General introduction to heavy neutral leptons and ν MSM | 7 |
| 1.3 Previous HNL searches | 8 |
| 2 The LHCb detector | 11 |
| 2.1 The Large Hadron Collider | 11 |
| 2.2 The Large Hadron Collider Beauty experiment | 13 |
| 2.2.1 The tracking system | 14 |
| 2.2.2 Calorimeters | 20 |
| 2.2.3 The Muon system | 22 |
| 2.2.4 Particle Identification | 22 |
| 2.2.5 The trigger system | 26 |
| 2.2.6 Data processing and simulation | 29 |
| 2.3 Luminosity measurement | 30 |
| 3 Probe for LUMinosity MEasurement in LHCb | 33 |
| 3.1 PLUME overview | 33 |
| 3.2 PLUME detector | 34 |
| 3.3 Detector performance | 43 |
| 4 Inclusive search for heavy neutral leptons in $B \rightarrow X\mu^+N$ with $N \rightarrow \mu^\pm\pi^\mp$ | 45 |
| 4.1 Search strategy | 45 |
| 4.2 Signal expectation | 48 |
| 4.3 Data and simulation samples | 50 |
| 4.3.1 Integrated luminosity | 50 |
| 4.3.2 Simulation samples | 50 |

Contents

| | | |
|----------|--|------------|
| 4.3.3 | Inclusive MC model for $B \rightarrow \mu^+ NX$ | 51 |
| 4.4 | Reconstruction and selection of the signal candidates | 53 |
| 4.4.1 | Signal reconstruction | 53 |
| 4.4.2 | Reconstruction categories | 54 |
| 4.4.3 | Trigger | 55 |
| 4.4.4 | Offline selection | 57 |
| 4.4.5 | Multivariate analysis selection | 62 |
| 4.4.6 | Optimisation of the particle identification selection | 68 |
| 4.5 | Signal efficiency | 71 |
| 4.5.1 | Fiducial volume efficiency | 71 |
| 4.5.2 | Pruning of reconstruction categories | 72 |
| 4.5.3 | Selection efficiency | 73 |
| 4.5.4 | Correction of MC efficiencies | 78 |
| 4.6 | Peaking backgrounds in the search mass region | 83 |
| 4.6.1 | Statistical background subtraction | 83 |
| 4.6.2 | Swap of the mass hypotheses | 83 |
| 4.6.3 | The ABCD method | 85 |
| 4.7 | Search for the signal peak in the invariant mass spectrum | 90 |
| 4.7.1 | Signal parameterisation | 90 |
| 4.7.2 | Background parameterisation | 91 |
| 4.7.3 | Fit to data | 93 |
| 4.7.4 | CL_s method | 94 |
| 4.7.5 | HNL production as a parameter of interest | 96 |
| 4.7.6 | HNL coupling as a parameter of interest | 97 |
| 4.7.7 | Scan in the HNL lifetime dimension and interpretation of the results | 97 |
| 4.7.8 | Generation of pseudoexperiments | 98 |
| 4.8 | Expected sensitivity | 101 |
| 4.8.1 | Blinded results of Majorana and Dirac scenarios interpretation | 102 |
| 4.9 | Uncertainties summary | 104 |
| 4.9.1 | Integrated luminosity | 104 |
| 4.9.2 | HNL production BR calculation | 104 |
| 4.9.3 | Signal efficiency | 104 |
| 4.9.4 | PDFs parameterisation | 105 |
| 5 | Conclusions and outlook | 107 |
| A | Additional figures and tables | 109 |
| A.1 | HLT efficiency tables | 109 |
| A.2 | MVA efficiencies | 111 |
| A.3 | 2D efficiency maps | 112 |
| A.4 | 2D L0 correction maps | 113 |
| A.5 | Mass fits | 116 |

| | |
|-------------------------|------------|
| Bibliography | 119 |
| Curriculum Vitae | 127 |

Introduction

The Standard Model (SM) of particle physics and the theory of General Relativity form the base of modern physics. In particular, the SM describes phenomena observed in particle physics, but despite its great success, currently there exist several experimental observations that contradict the current state of this theory: neutrino oscillations, the cosmological origin of the baryonic matter in the universe, the composition and origin of the dark matter (DM). Among extensions of the SM that have been proposed to solve one or several of these issues, the introduction of heavy neutral leptons (HNLs) would potentially address all three inconsistencies.

Heavy neutral leptons are hypothetical additional neutrinos, which unlike the SM ones, do not interact via any of the fundamental interactions of the SM, are heavy, and right-handed. In all existing nowadays models HNLs are feebly coupling to the SM neutrinos, and therefore there is a small window into the experimental constraints. Due to a feeble coupling, these hypothetical particles were not observed yet, and the research work outlined in this thesis is dedicated to the search for their production and decay.

This search is performed using the data of proton-proton (pp) collisions at the LHC collected by the LHCb detector. It is a general hunt for a particle with unknown mass, m_N , and lifetime, τ_N . Results of this research work are presented as the model-dependent limit on the mixing parameter $|U_\mu|^2$ between the HNL and the SM muon neutrino as a function of the HNL mass and lifetime, improving the previous LHCb result, and are being competitive with the world-best limit.

1 Theory and experimental motivation

1.1 General introduction to the Standard Model

The Standard Model (SM) of particle physics [1–4] describes all discovered fundamental particles and their interactions. It unifies three fundamental interactions: strong, weak and electromagnetic. This theory is constructed as a non-abelian, local gauge-invariant theory under the direct product on these three groups $G_{\text{SM}} = \text{SU}(3)_C \otimes \text{SU}(2)_L \otimes \text{U}(1)_Y$.

$\text{SU}(3)_C$ is the group of the special unitary 3×3 matrices describing the strong force field, where C is the colour charge, and is described by quantum chromodynamics (QCD). Left-handed (L) and hypercharge (Y) components represent the weak and electromagnetic interactions, which are unified into the electroweak interaction.

Within this theory, all particles are split into two groups, based on their properties (see Figure 1.1, left):

- **Fermions** have half-integer spin and follow the Fermi-Dirac statistics. There are 6 leptons: massive particles are electron (e^-), muon (μ^-), tau lepton (τ^-) and their associated massless (in the scope of the SM) neutrinos (ν_e, ν_μ, ν_τ). Also, there are 6 quarks: the up-type, with the electric charge $+2/3$, up (u), charm (c), top (t); and down-type, charge $-1/3$, down (d), strange (s) and bottom/beauty (b). Additionally, quarks have a colour charge of red, green or blue. Every fermion has a corresponding antiparticle with the same mass but opposite quantum numbers.
 - **Bosons**, have integer spin and described by the Bose-Einstein statistics. They are the mediators of the fundamental forces. The massless gluons, g , and photons, γ , are the mediators of the strong and electromagnetic forces, respectively. To accommodate the strong interaction of quarks, gluons have a combination of two colour charges (one of red, green, or blue and one of antired, antigreen, or antiblue). The massive Z and W^\pm bosons are the mediators of the weak interaction, responsible for the neutral and charged currents correspondingly.
- Finally, the last missing piece of the puzzle which was predicted a long time ago [5],

| Three Generations of Matter (Fermions) spin 1/2 | | | | | | Three Generations of Matter (Fermions) spin 1/2 | | | | | |
|---|--|--|--|-------|-------|---|--|--|--|-------|-------|
| I | | II | | III | | I | | II | | III | |
| mass → | 2.4 MeV | 1.27 GeV | 173.2 GeV | | | mass → | 2.4 MeV | 1.27 GeV | 173.2 GeV | | |
| charge → | 2/3 | 2/3 | 2/3 | | | charge → | 2/3 | 2/3 | 2/3 | | |
| name → | Left u up | Left c charm | Left t top | Right | Right | name → | Left u up | Left c charm | Left t top | Right | Right |
| Quarks | 4.8 MeV | 104 MeV | 4.2 GeV | | | Quarks | 4.8 MeV | 104 MeV | 4.2 GeV | | |
| | -1/3 | -1/3 | -1/3 | | | | -1/3 | -1/3 | -1/3 | | |
| | Left d down | Left s strange | Left b bottom | Right | Right | | Left d down | Left s strange | Left b bottom | Right | Right |
| Leptons | 0 | 0 | 0 | | | Leptons | 0 | 0 | 0 | | |
| | Left ν_e electron neutrino | Left ν_μ muon neutrino | Left ν_τ tau neutrino | Right | Right | | Left ν_e electron neutrino | Left ν_μ muon neutrino | Left ν_τ tau neutrino | Right | Right |
| | 0.511 MeV | 105.7 MeV | 1.777 GeV | | | | 0.511 MeV | 105.7 MeV | 1.777 GeV | | |
| | -1 | -1 | -1 | | | | -1 | -1 | -1 | | |
| | Left e electron | Left μ muon | Left τ tau | Right | Right | | Left e electron | Left μ muon | Left τ tau | Right | Right |
| | | | | | | | | | | | |
| | | | | | | | | | | | |
| | | | | | | | | | | | |
| | | | | | | | | | | | |
| | | | | | | | | | | | |
| | | | | | | | | | | | |
| | | | | | | | | | | | |
| | | | | | | | | | | | |
| | | | | | | | | | | | |
| | | | | | | | | | | | |
| | | | | | | | | | | | |
| | | | | | | | | | | | |
| | | | | | | | | | | | |
| | | | | | | | | | | | |
| | | | | | | | | | | | |
| | | | | | | | | | | | |
| | | | | | | | | | | | |
| | | | | | | | | | | | |
| | | | | | | | | | | | |
| | | | | | | | | | | | |
| | | | | | | | | | | | |
| | | | | | | | | | | | |
| | | | | | | | | | | | |
| | | | | | | | | | | | |
| | | | | | | | | | | | |
| | | | | | | | | | | | |
| | | | | | | | | | | | |
| | | | | | | | | | | | |
| | | | | | | | | | | | |
| | | | | | | | | | | | |
| | | | | | | | | | | | |
| | | | | | | | | | | | |
| | | | | | | | | | | | |
| | | | | | | | | | | | |
| | | | | | | | | | | | |
| | | | | | | | | | | | |
| | | | | | | | | | | | |
| | | | | | | | | | | | |
| | | | | | | | | | | | |
| | | | | | | | | | | | |
| | | | | | | | | | | | |
| | | | | | | | | | | | |
| | | | | | | | | | | | |
| | | | | | | | | | | | |
| | | | | | | | | | | | |
| | | | | | | | | | | | |
| | | | | | | | | | | | |
| | | | | | | | | | | | |
| | | | | | | | | | | | |
| | | | | | | | | | | | |
| | | | | | | | | | | | |
| | | | | | | | | | | | |
| | | | | | | | | | | | |
| | | | | | | | | | | | |
| | | | | | | | | | | | |
| | | | | | | | | | | | |
| | | | | | | | | | | | |
| | | | | | | | | | | | |
| | | | | | | | | | | | |
| | | | | | | | | | | | |
| | | | | | | | | | | | |
| | | | | | | | | | | | |
| | | | | | | | | | | | |
| | | | | | | | | | | | |
| | | | | | | | | | | | |
| | | | | | | | | | | | |
| | | | | | | | | | | | |
| | | | | | | | | | | | |
| | | | | | | | | | | | |
| | | | | | | | | | | | |
| | | | | | | | | | | | |
| | | | | | | | | | | | |
| | | | | | | | | | | | |
| | | | | | | | | | | | |
| | | | | | | | | | | | |
| | | | | | | | | | | | |
| | | | | | | | | | | | |
| | | | | | | | | | | | |
| | | | | | | | | | | | |
| | | | | | | | | | | | |
| | | | | | | | | | | | |
| | | | | | | | | | | | |
| | | | | | | | | | | | |
| | | | | | | | | | | | |
| | | | | | | | | | | | |
| | | | | | | | | | | | |
| | | | | | | | | | | | |
| | | | | | | | | | | | |
| | | | | | | | | | | | |
| | | | | | | | | | | | |
| | | | | | | | | | | | |
| | | | | | | | | | | | |
| | | | | | | | | | | | |
| | | | | | | | | | | | |
| | | | | | | | | | | | |
| | | | | | | | | | | | |
| | | | | | | | | | | | |
| | | | | | | | | | | | |
| | | | | | | | | | | | |
| | | | | | | | | | | | |
| | | | | | | | | | | | |
| | | | | | | | | | | | |
| | | | | | | | | | | | |
| | | | | | | | | | | | |
| | | | | | | | | | | | |
| | | | | | | | | | | | |
| | | | | | | | | | | | |
| | | | | | | | | | | | |
| | | | | | | | | | | | |
| | | | | | | | | | | | |
| | | | | | | | | | | | |
| | | | | | | | | | | | |
| | | | | | | | | | | | |
| | | | | | | | | | | | |
| | | | | | | | | | | | |
| | | | | | | | | | | | |
| | | | | | | | | | | | |
| | | | | | | | | | | | |
| | | | | | | | | | | | |
| | | | | | | | | | | | |
| | | | | | | | | | | | |
| | | | | | | | | | | | |
| | | | | | | | | | | | |
| | | | | | | | | | | | |
| | | | | | | | | | | | |
| | | | | | | | | | | | |
| | | | | | | | | | | | |
| | | | | | | | | | | | |
| | | | | | | | | | | | |
| | | | | | | | | | | | |
| | | | | | | | | | | | |
| | | | | | | | | | | | |
| | | | | | | | | | | | |
| | | | | | | | | | | | |
| | | | | | | | | | | | |
| | | | | | | | | | | | |
| | | | | | | | | | | | |
| | | | | | | | | | | | |
| | | | | | | | | | | | |
| | | | | | | | | | | | |
| | | | | | | | | | | | |
| | | | | | | | | | | | |
| | | | | | | | | | | | |
| | | | | | | | | | | | |
| | | | | | | | | | | | |
| | | | | | | | | | | | |
| | | | | | | | | | | | |
| | | | | | | | | | | | |
| | | | | | | | | | | | |
| | | | | | | | | | | | |
| | | | | | | | | | | | |
| | | | | | | | | | | | |
| | | | | | | | | | | | |
| | | | | | | | | | | | |
| | | | | | | | | | | | |
| | | | | | | | | | | | |
| | | | | | | | | | | | |
| | | | | | | | | | | | |
| | | | | | | | | | | | |
| | | | | | | | | | | | |
| | | | | | | | | | | | |
| | | | | | | | | | | | |
| | | | | | | | | | | | |
| | | | | | | | | | | | |
| | | | | | | | | | | | |
| | | | | | | | | | | | |
| | | | | | | | | | | | |
| | | | | | | | | | | | |
| | | | | | | | | | | | |
| | | | | | | | | | | | |
| | | | | | | | | | | | |
| | | | | | | | | | | | |
| | | | | | | | | | | | |
| | | | | | | | | | | | |
| | | | | | | | | | | | |
| | | | | | | | | | | | |
| | | | | | | | | | | | |
| | | | | | | | | | | | |
| | | | | | | | | | | | |
| | | | | | | | | | | | |
| | | | | | | | | | | | |
| | | | | | | | | | | | |
| | | | | | | | | | | | |
| | | | | | | | | | | | |
| | | | | | | | | | | | |
| | | | | | | | | | | | |
| | | | | | | | | | | | |
| | | | | | | | | | | | |
| | | | | | | | | | | | |
| | | | | | | | | | | | |
| | | | | | | | | | | | |
| | | | | | | | | | | | |
| | | | | | | | | | | | |
| | | | | | | | | | | | |
| | | | | | | | | | | | |
| | | | | | | | | | | | |
| | | | | | | | | | | | |
| | | | | | | | | | | | |
| | | | | | | | | | | | |
| | | | | | | | | | | | |
| | | | | | | | | | | | |
| | | | | | | | | | | | |
| | | | | | | | | | | | |
| | | | | | | | | | | | |
| | | | | | | | | | | | |
| | | | | | | | | | | | |
| | | | | | | | | | | | |
| | | | | | | | | | | | |
| | | | | | | | | | | | |
| | | | | | | | | | | | |
| | | | | | | | | | | | |
| | | | | | | | | | | | |
| | | | | | | | | | | | |
| | | | | | | | | | | | |
| | | | | | | | | | | | |
| | | | | | | | | | | | |
| | | | | | | | | | | | |
| | | | | | | | | | | | |
| | | | | | | | | | | | |
| | | | | | | | | | | | |
| | | | | | | | | | | | |
| | | | | | | | | | | | |
| | | | | | | | | | | | |
| | | | | | | | | | | | |
| | | | | | | | | | | | |
| | | | | | | | | | | | |
| | | | | | | | | | | | |
| | | | | | | | | | | | |
| | | | | | | | | | | | |
| | | | | | | | | | | | |
| | | | | | | | | | | | |
| | | | | | | | | | | | |
| | | | | | | | | | | | |
| | | | | | | | | | | | |
| | | | | | | | | | | | |
| | | | | | | | | | | | |
| | | | | | | | | | | | |
| | | | | | | | | | | | |
| | | | | | | | | | | | |
| | | | | | | | | | | | |
| | | | | | | | | | | | |
| | | | | | | | | | | | |
| | | | | | | | | | | | |
| | | | | | | | | | | | |
| | | | | | | | | | | | |
| | | | | | | | | | | | |
| | | | | | | | | | | | |
| | | | | | | | | | | | |
| | | | | | | | | | | | |
| | | | | | | | | | | | |
| | | | | | | | | | | | |
| | | | | | | | | | | | |
| | | | | | | | | | | | |
| | | | | | | | | | | | |
| | | | | | | | | | | | |
| | | | | | | | | | | | |
| | | | | | | | | | | | |
| | | | | | | | | | | | |
| | | | | | | | | | | | |
| | | | | | | | | | | | |
| | | | | | | | | | | | |
| | | | | | | | | | | | |
| | | | | | | | | | | | |
| | | | | | | | | | | | |
| | | | | | | | | | | | |
| | | | | | | | | | | | |
| | | | | | | | | | | | |
| | | | | | | | | | | | |
| | | | | | | | | | | | |
| | | | | | | | | | | | |
| | | | | | | | | | | | |
| | | | | | | | | | | | |
| | | | | | | | | | | | |
| | | | | | | | | | | | |
| | | | | | | | | | | | |

which after spontaneous symmetry breaking leads to the charged lepton masses expressed by

$$m_{\alpha\beta}^{\text{lep}} = Y_{\alpha\beta}^{\text{lep}} \frac{v}{\sqrt{2}}, \quad (1.2)$$

where v is the vacuum expectation value of the Higgs field and $Y_{\alpha\beta}^{\text{lep}}$ is the Yukawa coupling coefficients. Consequently, since the SM does not contain right-handed neutrinos, such Yukawa term can not be build for them and makes them massless by construction.

1.1.2 Masses of the SM neutrinos

It is already more than two decades since the puzzle of neutrino mass exists and already several times it was updated with more experimental evidence, brand-new dedicated experiments and theories. In order to fully introduce the problem which this thesis work is dedicated to, it is important to start with historical aspects of the recent neutrino physics and theoretical implications that were drawn from them that are very well summarised in Ref. [9] and are mentioned further.

The discovery of neutrino oscillations in 1998 by the Super-Kamiokande experiment [10], followed by the evidence of neutrino flavours transformation by the SNO experiment [11], has indicated that neutrino have masses and that the lepton mixing exists. It greatly affected our understanding of particle physics, since it is the first case of physics beyond the SM which is confirmed in the laboratory. After that, data from the deep underground detectors, several reactor and accelerator experiments have brought more knowledge, so now we have accurate enough measurements of Δm_{21}^2 and $|\Delta m_{32}^2|$, where $\Delta m_{ij}^2 = m_{\nu i}^2 - m_{\nu j}^2$, and the three Euler angles parameterising the Pontecorvo–Maki–Nakagawa–Sakata (PMNS) matrix [12], θ_{12} , θ_{13} , and θ_{23} . The PMNS matrix is a mixing matrix of neutrino in the eigenstates of the weak interaction, $(\nu_e, \nu_\mu, \nu_\tau)$, and the mass eigenstates (ν_1, ν_2, ν_3) , defined as

$$\begin{bmatrix} \nu_e \\ \nu_\mu \\ \nu_\tau \end{bmatrix} = \begin{bmatrix} U_{e1} & U_{e2} & U_{e3} \\ U_{\mu 1} & U_{\mu 2} & U_{\mu 3} \\ U_{\tau 1} & U_{\tau 2} & U_{\tau 3} \end{bmatrix} \begin{bmatrix} \nu_1 \\ \nu_2 \\ \nu_3 \end{bmatrix}, \quad (1.3)$$

where $U_{\alpha i}$ corresponds to the amplitude of mass eigenstate i in flavour α basis. It can be parameterised by the three Euler angles θ_{12} , θ_{13} , θ_{23} and a phase angle δ_{CP}

$$\begin{aligned} & \begin{bmatrix} 1 & 0 & 0 \\ 0 & c_{23} & s_{23} \\ 0 & -s_{23} & c_{23} \end{bmatrix} \begin{bmatrix} c_{13} & 0 & s_{13}e^{-i\delta_{CP}} \\ 0 & 1 & 0 \\ -s_{13}e^{i\delta_{CP}} & 0 & c_{13} \end{bmatrix} \begin{bmatrix} c_{12} & s_{12} & 0 \\ -s_{12} & c_{12} & 0 \\ 0 & 0 & 1 \end{bmatrix} \\ &= \begin{bmatrix} c_{12}c_{13} & s_{12}c_{13} & s_{13}e^{-i\delta_{CP}} \\ -s_{12}c_{23} - c_{12}s_{23}s_{13}e^{i\delta_{CP}} & c_{12}c_{23} - s_{12}s_{23}s_{13}e^{i\delta_{CP}} & s_{23}c_{13} \\ s_{12}s_{23} - c_{12}c_{23}s_{13}e^{i\delta_{CP}} & -c_{12}s_{23} - s_{12}c_{23}s_{13}e^{i\delta_{CP}} & c_{23}c_{13} \end{bmatrix}, \end{aligned} \quad (1.4)$$

where s_{ij} and c_{ij} are $\sin\theta_{ij}$ and $\cos\theta_{ij}$, respectively.

Chapter 1. Theory and experimental motivation

Their values have been obtained from a global fit [13], and for the normal mass ordering (NO) or for the inverted mass ordering (IO) are equal to

$$\begin{aligned}\theta_{12} &= 33.44^{+0.71}_{-0.74}^\circ \text{ (NO)} & \theta_{12} &= 33.45^{+0.78}_{-0.75}^\circ \text{ (IO)} \\ \theta_{23} &= 49.20^{+0.90}_{-1.10}^\circ \text{ (NO)} & \theta_{23} &= 49.90^{+0.90}_{-1.10}^\circ \text{ (IO)} \\ \theta_{13} &= 8.57^{+0.13}_{-0.12}^\circ \text{ (NO)} & \theta_{13} &= 8.60^{+0.13}_{-0.12}^\circ \text{ (IO)} \\ \delta_{CP} &= 197^{+27}_{-24}^\circ \text{ (NO)} & \delta_{CP} &= 282^{+26}_{-30}^\circ \text{ (IO)},\end{aligned}$$

where the NO assumption is $m_3 > m_2 > m_1$ and the IO corresponds to $m_2 > m_1 > m_3$. Unlike for the quark sector, these angles are sizable and there was a first hint of CP-violation with $\delta_{CP} = -90^\circ$ but then it was shifted to CP-conservation $\delta_{CP} \approx 180^\circ$ value with the recent data. It is expected that in the coming years, the long baseline experiments DUNE and Hyper-Kamiokande [14, 15] will be able to measure the δ_{CP} value with clarification on leptonic CP-violation.

The measured mass-squared differences of neutrinos are:

$$\begin{aligned}\Delta m_{12}^2 &= +7.420^{+0.210}_{-0.200} \cdot 10^{-5} \text{eV}^2 \text{ (NO)} & \Delta m_{12}^2 &= +7.420^{+0.210}_{-0.200} \cdot 10^{-5} \text{eV}^2 \text{ (IO)} \\ \Delta m_{32}^2 &= +2.517^{+0.026}_{-0.028} \cdot 10^{-3} \text{eV}^2 \text{ (NO)} & \Delta m_{32}^2 &= -2.498^{+0.028}_{-0.028} \cdot 10^{-3} \text{eV}^2 \text{ (IO)},\end{aligned}$$

from what one can deduce that there are at least two massive neutrinos ordered in two possible ways:

- Normal ordering (NO): $m_{32}^2 > 0$ with $m_3 > m_2 > m_1$
- Inverted ordering (IO): $m_{32}^2 > 0$ with $m_2 > m_1 > m_3$.

With these relations, as stated in [9], we obtain important benchmarks for the absolute scale of neutrino masses:

$$\sum_{j=1}^3 m_j \geq \begin{cases} 60 \text{ meV (NO)} \\ 100 \text{ meV (IO)} \end{cases}. \quad (1.5)$$

Taking into account the recent upper limit on the effective electron anti-neutrino mass defined as $m_\nu \equiv \sqrt{\sum_{j=1,2,3} |U_{ej}|^2 m_j^2} < 0.8 \text{ eV}^1$ by KATRIN [16], where U_{ej} are elements of the PNMS matrix, and cosmological searches constraint $\sum_{j=1,2,3} m_j < 0.12 \text{ eV}$ [17], there are still several crucial questions unanswered:

- What are the absolute values of the neutrinos masses and how are they generated?
- What is the nature of neutrinos, i.e. are they Dirac or Majorana particles?
- Is the standard three-flavours neutrino picture correct or are there additional sterile neutrinos?

¹Natural units are used throughout the text

Together with aforementioned problems, the leptonic mixing parameters of a very different structure compared to the quarks, hint about a different origin of neutrino masses. One of the scenarios could be the right-handed neutrinos, i.e heavy neutral leptons (HNLs), that are the main subject of the study in this thesis.

1.2 General introduction to heavy neutral leptons and ν MSM

HNLs are hypothetical right-handed neutrinos, ν_R , that do not interact via any of the fundamental interaction of the SM. When extending the SM, by adding a singlet ν_R , see Figure 1.1, right, one can accommodate the SM neutrino masses via the see-saw mechanism [18]. This mechanism, among other theories, proposes to solve the issue of the recently observed small masses of the SM neutrinos by introducing a very heavy right-handed neutrino whose mass is coupled to that of its left-handed counterpart. Additionally, they could provide a dark matter particle as a very long-lived HNL [18–20] and even explain the matter-antimatter asymmetry of the universe [21–23].

The HNL is sterile with respect to the SM gauge groups and couples through the so-called neutrino portal

$$\mathcal{L}_{\text{Neutrino portal}} = F_\alpha (\bar{L}_\alpha \cdot \tilde{H}) N + \text{h.c.} , \quad (1.6)$$

where L_α is the SM lepton doublet, \tilde{H} is a conjugated SM Higgs doublet and F_α is dimensionless Yukawa coupling.

Therefore, the HNL couples to the W and Z bosons in the same way as SM neutrinos but with a strength suppressed by the small mixing parameter U_α , as summarised in a review of the phenomenology of HNLs [24]:

$$\mathcal{L}_{\text{int}} = \frac{g}{2\sqrt{2}} W_\mu^+ \bar{N}^c \sum_\alpha U_\alpha^* \gamma^\mu (1 - \gamma_5) \ell_\alpha^- + \frac{g}{4\cos\theta_W} Z_\mu \bar{N}^c \sum_\alpha U_\alpha^* \gamma^\mu (1 - \gamma_5) \nu_\alpha + \text{h.c.} . \quad (1.7)$$

The full model is called Neutrino Minimal Standard Model (ν MSM) [22,25], that has additional three right-handed neutrinos $N_{1,2,3}$ (see Fig.1.1, right). The heaviest $N_{2,3}$ generate the masses of active neutrinos via the Seesaw mechanism. The same two $N_{2,3}$ neutrinos could also generate the baryon asymmetry of the Universe (BAU) if they are nearly mass-degenerate. Finally, the lightest sterile neutrino N_1 is a perfect DM candidate with the tiny Yukawa coupling, which makes it almost massless. From the see-saw mechanism principles, it is possible to put the limitations on the mass of HNL: using the assumption $m_\nu \ll M_N$, masses of the active neutrino are much smaller than the scale of M_N and the electroweak scale. In this way, the most natural solutions are a GeV or TeV scale M_N . For now, the HNLs with the TeV-scale masses are not within the range of current accelerator experiments, but the GeV-scale masses (and Yukawa couplings $\mathcal{O}(10^{-5})$) could be efficiently searched for with experimental technologies that exist nowadays.

In that scale, the most efficient way to hunt for HNLs is looking at their decays to the SM particles, i.e. to perform a direct search. HNLs are decaying into the SM particles because of its mixing with the active neutrinos and therefore could be found in the final states with two charged leptons:

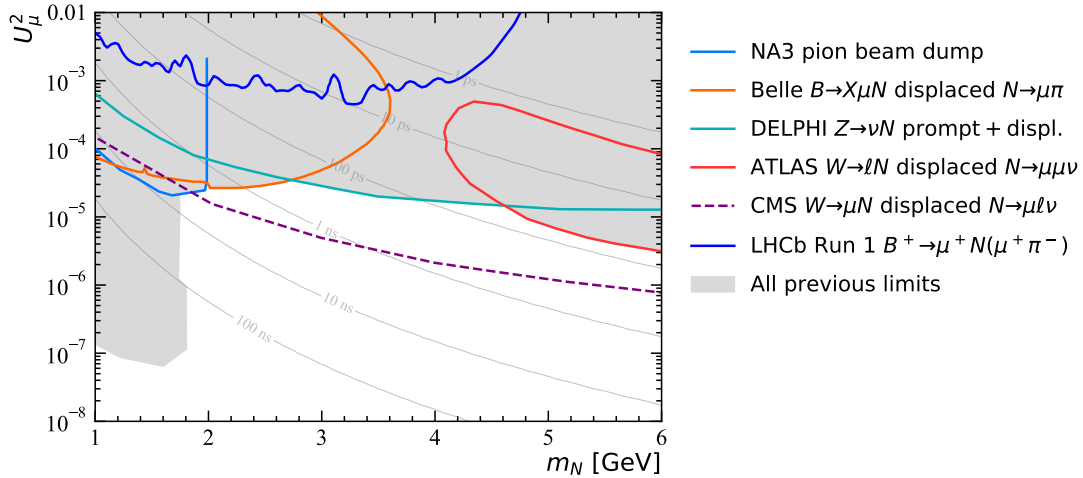
$$N \rightarrow e^+ e^- \nu, \quad \mu^+ \mu^- \nu, \quad \mu^+ e^- \nu, \quad \text{etc}, \quad (1.8)$$

or with charged hadrons:

$$N \rightarrow \pi^+ e^-, \quad \pi^+ \mu^-, \quad K^+ \pi^- \nu, \quad \text{etc}. \quad (1.9)$$

In the scope of this thesis, the case of detecting only 1 sterile neutrino is covered, which needs only 4 parameters: mass M_N and sterile neutrino mixings with all three active neutrinos U_α . Particularly, the main focus is on the HNL that mix with ν_μ and could be detected with the LHCb experiment, which is introduced further in Chapter 2.

1.3 Previous HNL searches



[b]

Figure 1.2 – Regions of the U_μ^2 versus m_N parameter space that are excluded by previous experiments. More details and references in the main text.

The current excluded regions in the U_μ^2 versus m_N parameter space are shown in Fig. 1.2. It shows the most interesting for us GeV range. HNLs that are light enough to be produced in D meson decays are strongly constrained to the level of $U_\mu^2 < 10^{-7}$ and $c\tau_N > 100$ m, which is not accessible to LHCb with current dataset. In the HNL mass region below 2 GeV, the main constraints come from the NA3 [26] and CHARM [27] experiments, which were both beam-dump experiments located at CERN SPS. They used beams of 300 GeV π^- and 400

GeV protons correspondingly. NA3 has covered exhaustive list of final state decays: $\mu^+\mu^-$, e^+e^- , $e\mu$, $\mu\pi$, $\pi^+\pi^-$, as well as kaons. While CHARM focused on neutrinos decaying into the leptonic final states only and has put the strongest limit of $|U_e|^2$, $|U_\mu|^2 < 10^{-7}$. Then goes Belle [28], which is an experiment at a e^+e^- collider, searching for HNLs produced in B -hadron decays. Specifically, $B \rightarrow X l N$, $N \rightarrow l \pi$, with $l = e, \mu$ with displaced N vertexes. It overlaps with exclusion curve of the DELPHI [29] experiment, which was a 4π detector at the LEP collider, predecessor of the LHC. This search studied prompt and displaced signatures of $Z \rightarrow \nu N$, $N \rightarrow \nu l \bar{l}$, $\nu q \bar{q}$, $l q \bar{q}'$, with $l = e, \mu, \tau$; $q = u, d, s, c, b$ and $q \bar{q}' = u \bar{d}, c \bar{s}$ and, predictably, using a large phase-space available from the mass of Z boson, covered a wide range of M_N . ATLAS [30] and the CMS [31] experiments covered displaced decays of $N \rightarrow ll\nu$ with N being produced in $W \rightarrow N l$ decays. With an excellent sensitivity to this type of decays (as they are *general purpose detectors*) and high luminosity of proton-proton collisions at the LHC they put the strongest to date limits on U_μ^2 mixing for HNL masses above 2 GeV. Finally, a search was performed at LHCb with Run 1 data [32] using the exclusive decay channel $B^+ \rightarrow \mu^+ N (\rightarrow \mu^+ \pi^-)$, but is not competitive with previous limits (note that the exclusion region was revised in [33] due to a wrong theoretical assumption in the original LHCb paper). HNLs with masses larger than about 5 GeV are produced mostly in Z or W bosons decays and are searched most effectively with the ATLAS [30, 34] and CMS [31, 35, 36] detectors.

In this thesis a new search for HNLs with LHCb data is presented, which takes into account the experience and results of the previous searches and yet employs new techniques to reach the sensitivity that was not achieved with LHCb before.

2 The LHCb detector

This chapter is mainly about the LHCb detector, its design, performance and upgrade. In addition, it includes a short introduction about the Large Hadron Collider to provide an experimental environment of this thesis, since it has great influence on the search strategy and experimental techniques that were used and introduced further.

2.1 The Large Hadron Collider

The Conseil Européen pour la Recherche Nucléaire (CERN) hosts the largest accelerator complex in the world (see Figure 2.1) where the Large Hadron Collider (LHC), the most powerful proton-proton and heavy ion collider, is located. The LHC is build in the already existing 27 km long and about 100 m deep underground tunnel, replacing the Large Electron-Positron collider (LEP).

Before filling up the LHC, proton bunches are handled by several intermediate machines, called the injector chain, as shown in Figure 2.1. At first, hydrogen ions are accelerated to the momentum of 160 MeV and injected into the Proton Synchrotron Booster (PSB), where they are accelerated to 2 GeV. Then they are injected into the Proton Synchrotron (PS). At the PS, the beam is further shaped and is accelerated to obtain nominal for the LHC bunch parameters, and it gains momentum of 26 GeV. Finally, the bunches are injected into the Super Proton Synchrotron (SPS), accelerated to 450 GeV and transfered via the two different lines into two opposite-directional beam pipes of the LHC. Contrary to protons, heavy ions injection chain starts from the Electron-Cyclotron Resonance (ECR) ion source. $^{208}\text{Pb}^{+29}$ ions are selected by a spectrometer, then accelerated by the LINAC3 and by the Low Energy Ion Ring (LEIR), finally injected into the SPS and, subsequently, the LHC. At several stages of this process ions are being stripped of their electrons increasing their charge to the state of $^{208}\text{Pb}^{+82}$.

To reach its target momentum of about 7 TeV, LHC operates superconducting magnets with dipolar magnetic field of 8.3 T. The operation frequency is 40 MHz, which leads to operation of 2808 bunches (with 1.2×10^{11} protons each) per beam. After the acceleration, during the

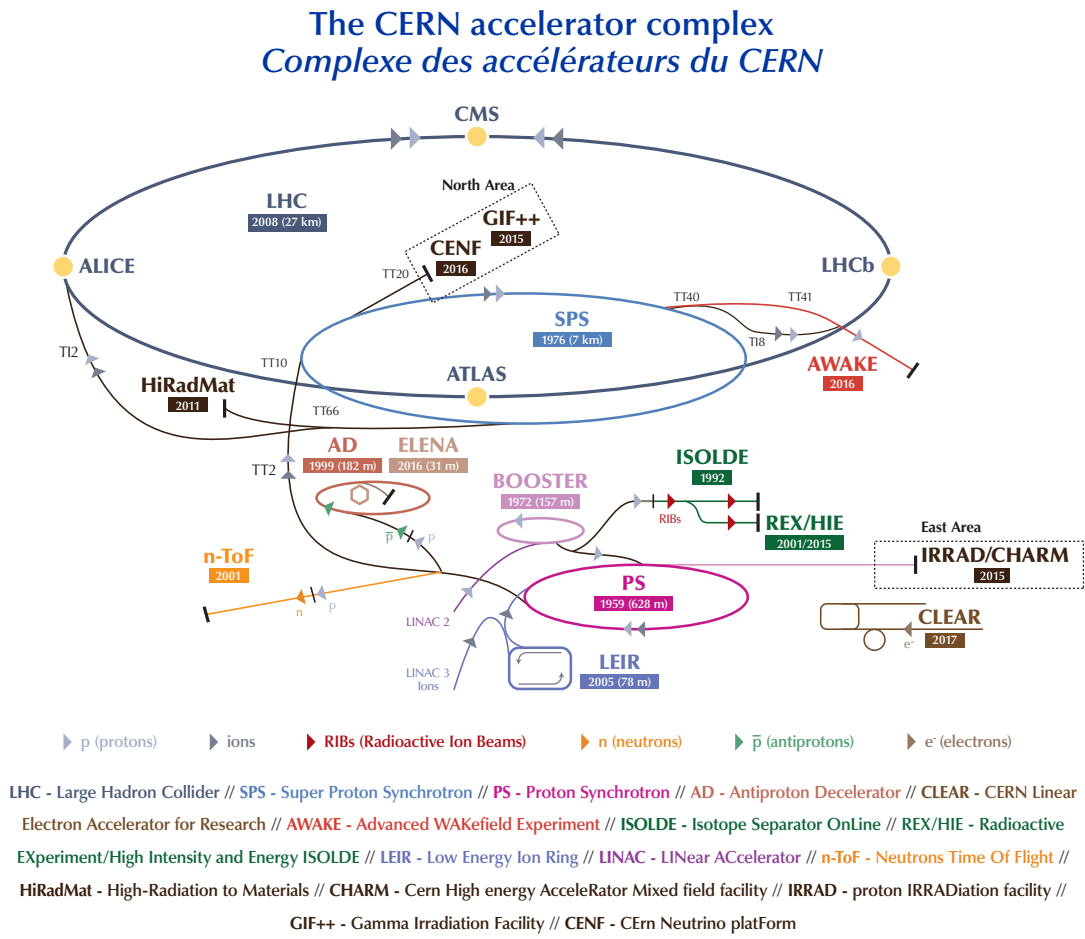


Figure 2.1 – Schematic layout of the CERN accelerator complex [37].

data taking, beams are colliding in four crossing points, where the large experiments are located. CMS [38] and ATLAS [39] are general purpose detectors; ALICE [40] is focused on the heavy-ion program; and LHCb [41]. In Run 1, during 2010-2011 LHC operated collisions at a centre-of-mass energy of 7 TeV, 2011-2012 at 8 TeV and then the Run 2 was in 2015-2018, with the energy of 13 TeV.

The performance of a particle collider and experiment is generally quantified by the beam energy and luminosity. While the energy is crucial to cross the threshold of needed energy in the center of mass to produce the particles of interest and to extend the reach of possible searches for new physics, luminosity defines the number of useful interactions. Luminosity \mathcal{L} is the proportionality factor between the rate of events of a given process of interest and its cross section σ_p ,

$$\frac{dN}{dt} = \mathcal{L} \cdot \sigma_p. \quad (2.1)$$

The equation above, in a sense, lays in the base of this research, meaning that it is used to describe a probability of observing the hypothetical phenomena that is studied. In the following chapters it will be expanded¹ once the subject is developed further but before doing that, it is important to introduce the experimental medium and tools that were used for it.

2.2 The Large Hadron Collider Beauty experiment

The LHCb experiment is a dedicated heavy flavour experiment built to make precision measurements of CP violation and of the rare decays of beauty and charm hadrons. Since the angular distribution of $b\bar{b}$ quark pairs produced in the proton-proton collision is maximal in the forward region (see Figure 2.3), the LHCb experiment was designed as a single arm forward spectrometer with an angular coverage of approximately 15 mrad to 300 mrad. When redefined as a pseudorapidity, $\eta = -\ln\left[\tan\frac{\theta}{2}\right]$, where θ is the angle between the beam direction and the particle momentum, this corresponds to $1.8 < \eta < 4.9$.

As shown in Figure 2.2, the layout of the LHCb spectrometer is composed of several subdetectors along the beam axis, z . Following one after another, these subdetectors are providing bits of complementary information needed to reconstruct all essential particles that are produced in an event of proton-proton collision.

The LHCb experiment is designed to operate [43] with a luminosity roughly 10 times lower than that of ATLAS or CMS. This is achieved by introducing a transverse beam offset between colliding bunches, and consequently, lowering the number of simultaneous pp collisions in a bunch crossing, called *pile-up*. This technique is called *luminosity leveling* [44], and is essential for keeping detector occupancy at designed level but also to avoid extra radiation damage. Integrated luminosity collected during previously defined Run 1-Run 2 is summarised in Table 2.1.

¹The Equation 4.1 from Section 4.2 is meant here.

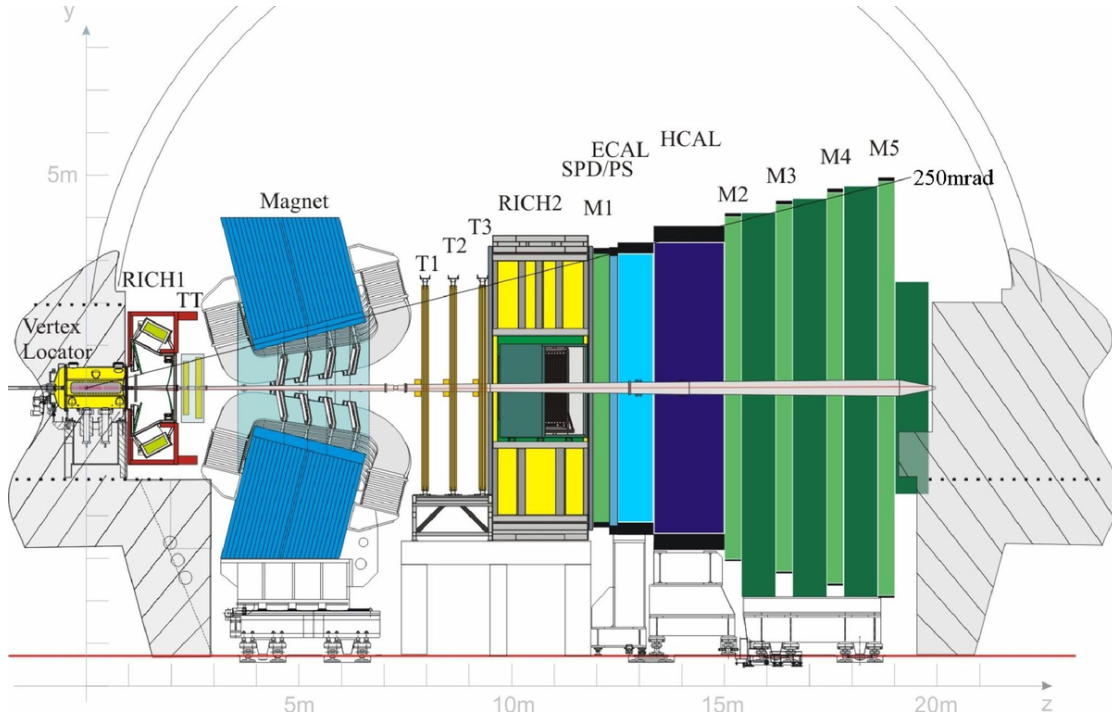


Figure 2.2 – Schematic view of the LHCb detector operating in Run 1-Run 2 [41].

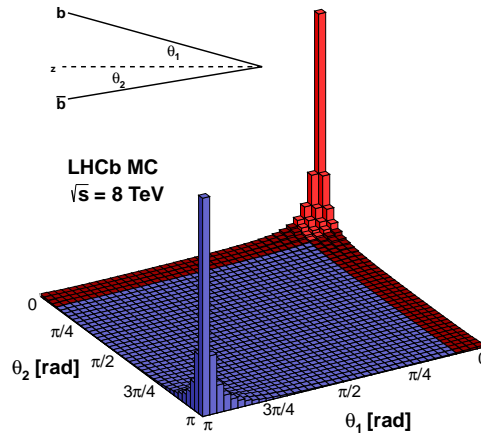


Figure 2.3 – Angular distribution of $b\bar{b}$ quark pairs produced from proton-proton collision at LHC in terms of polar angles [42].

2.2.1 The tracking system

When a charged particle passes through a tracking detector, it interacts with the detector material and leaves signatures of the passage (energy deposits, or hits), which are precisely located and then combined and reconstructed into the track object. If the tracker is placed in

2.2. The Large Hadron Collider Beauty experiment

Table 2.1 – Integrated luminosity collected by LHCb during Run 1-2.

| | Year | \sqrt{s} [TeV] | $\int \mathcal{L}$ [fb ⁻¹] |
|-------|------|------------------|--|
| Run 1 | 2011 | 7 | 1.0 |
| | 2012 | 8 | 2.0 |
| Run 2 | 2016 | 13 | 1.6 |
| | 2017 | 13 | 1.7 |
| | 2018 | 13 | 2.2 |

a precisely calibrated magnetic field it is possible to determine the momentum of a particle candidate from the reconstructed curvature of the track for known (or assumed) charge of a particle. When going from the left to right on Figure 2.2, the tracking system of LHCb includes the VERtex LOCator (VELO), which is located around the interaction point, the Tracker Turicensis (TT), a dipole magnet and three tracking stations right after (T1, T2, T3).

VERtex LOCator

The VERtex LOCator (VELO) is built around the interaction point inside a vacuum tank and contains 42 silicon modules arranged along the beam axis. Each module has silicon micro-strip sensors oriented in a radial and azimuthal directions providing a measurement of the r and ϕ coordinates, as shown in Figure 2.4. The strip pitch within a module increases radially from 38 μm to 102 μm . In order to fulfill the requirements from the LHCb physics programme to precisely measure b and c -hadrons, which have a sufficient lifetime to travel macroscopic distances [45], the VELO is placed very closely to the beam (8.2 mm). The main task of the VELO is to locate the primary vertex (PV), where the pp collision occurs and all the primary tracks origin from, and to reconstruct the displaced secondary vertex (SV), which is formed by the decay products of the heavy hadron.

As summarised in the VELO performance paper [46], this subdetector achieves the PV resolution of 13 μm in the transverse to the beam plane and of 71 μm in the plane along the beam axis for a vertex with 25 tracks. For tracks with the transverse momentum greater than 1 GeV, an impact parameter resolution is less than 35 μm , where the impact parameter of a track is defined as the distance between the track and the PV at the point of the closest approach.

For the detector safety, the VELO detector is composed of two halves that can move horizontally. This is done to be able to increase the distance between two modules during the LHC beam injection and to close it back only during the stable beams.

The LHCb dipole magnet

The LHCb detector has a warm dipole magnet of a large aperture, shown in Figure 2.5, to bend the trajectory of charged particles within its acceptance.

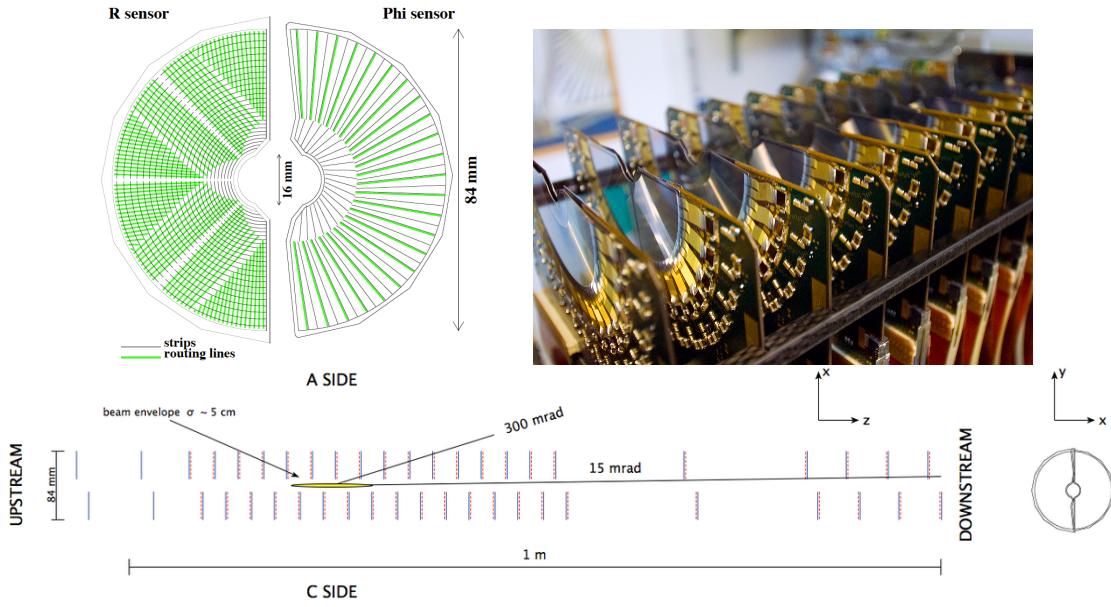


Figure 2.4 – Schematic view of an R and Φ sensor (left). One side of the VELO during assembly showing the silicon sensors, readout and modules support (right). (bottom) Schematic cross-section in the xz plane at $y = 0$ [46].

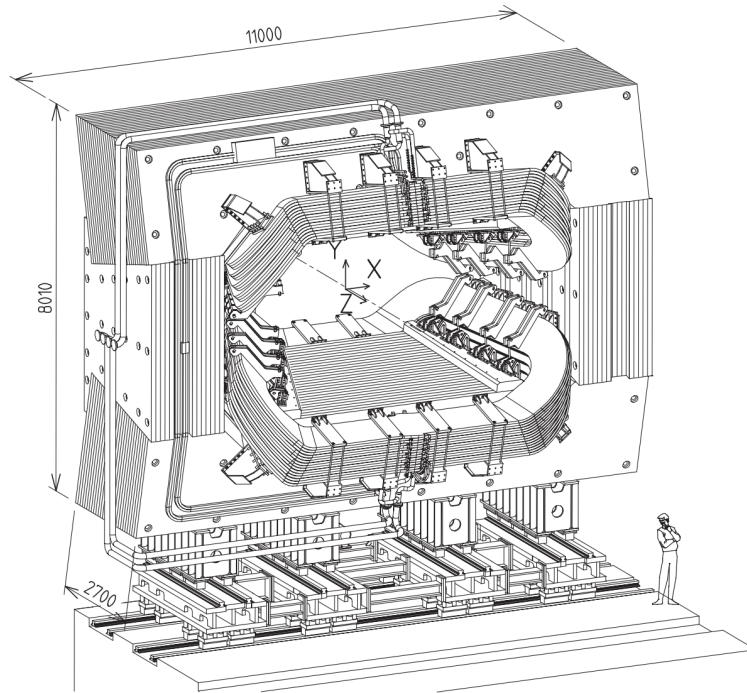


Figure 2.5 – Schematic view of the LHCb dipole magnet [41].

The spectrometer magnet provides an integrated field of about 4 Tm (see Figure 2.6) along the tracking system, bending the particles in the horizontal xz plane. The field polarity is regularly

switched during the detector operation and data taking, forming two configurations called *MagUp* and *MagDown*, to check for the possible asymmetries of the detector performance. This procedure allows to cancel out most detector asymmetries, and study systematic biases induced by them. The LHCb dipole has also an impact on the LHC beam dynamics, so three additional dipole magnets are used to compensate for this effect.

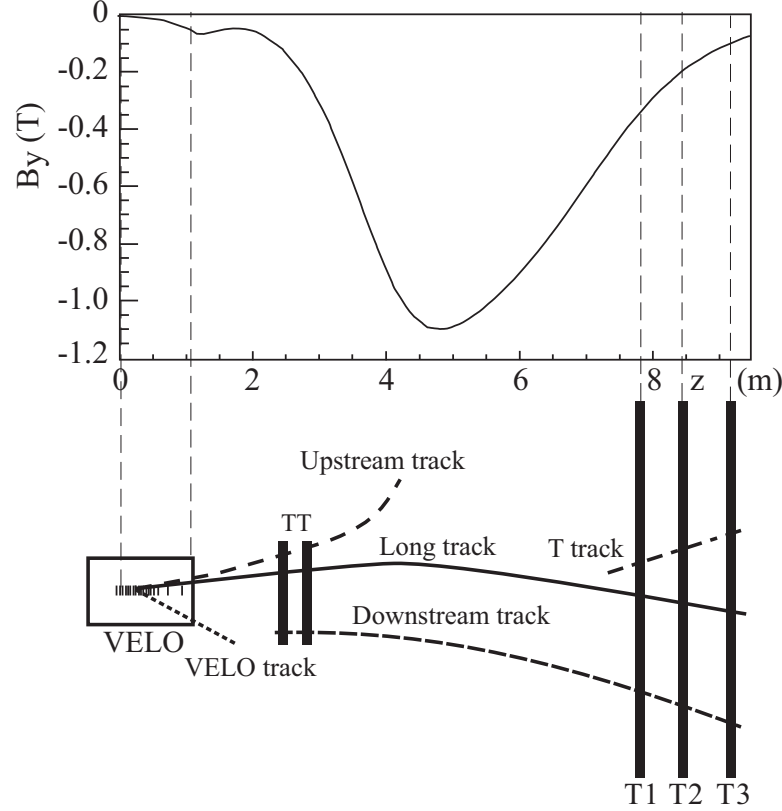


Figure 2.6 – Magnetic flux density as a function of z coordinate along the beam axis (top) with projected schematic cartoon of the tracking system (bottom) with illustrated various track types [41].

The Tracker Turicensis

The TT stations [47] are placed before the magnet and are about 150 cm wide and 130 cm high, with a total active area of around 8 m^2 . This subdetector uses $500 \mu\text{m}$ thick silicon microstrip sensors with 512 strips. These strips have a pitch of $183 \mu\text{m}$, providing a resolution on the hit position of $50 \mu\text{m}$. Modules are composed of 4 layers (see Figure 2.7) and displaced along z by 27 cm into two stations: TTA and TTb. These four detection layers have a $x - u - v - x$ arrangement, with vertical strips in x layers and strips rotated by a stereo angle of $+5^\circ$ and -5° in the u and v layers, respectively. Such a tilted structure is more efficient for the ghost tracks elimination than a usual perpendicular grid-like arrangement. The TT modules have read-out sectors with one, two, three or four sensors bonded together, and are arranged such that the

single-sensor sectors (with finer spatial resolution) are closest to the beam-pipe axis, where the flux of particles is the highest.

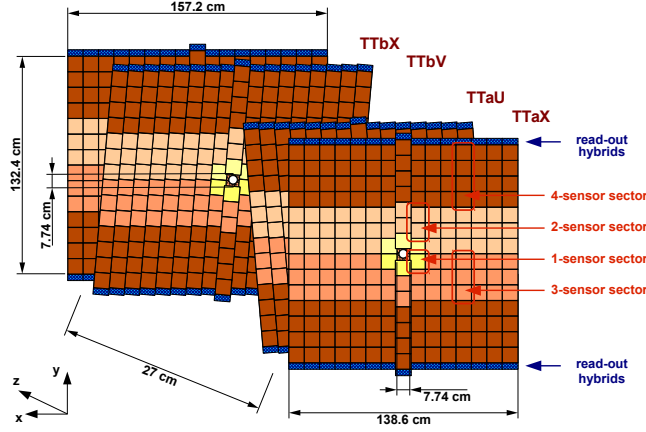


Figure 2.7 – Schematic view of the TT layers [48].

The Inner Tracker

The T1, T2 and T3 stations are located downstream from the magnet. In the region closer to the beam pipe, the acceptance is covered by the Inner Tracker (IT) [49]. Similar to the TT, microstrip technology of $410\ \mu\text{m}$ thick strips with a pitch of $198\ \mu\text{m}$ is used. The IT covers a 120 cm wide and 40 cm high cross-shaped region in the centre of the T1-T3 tracking stations (see Figure 2.8), providing the hit position resolution of $50\ \mu\text{m}$.

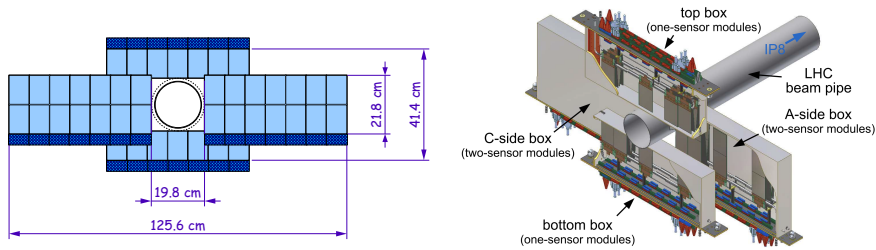


Figure 2.8 – A single IT layer (left) and the 3D layout (right) [41].

The Outer Tracker

The Outer Tracker (OT) [50], hence the name, covers the remaining acceptance around the IT. It employs a drift-tube technology with approximately 200 gas-tight, 2.4 m long, straw-tube modules with a drift-time readout. Every module is composed of two staggered layers of drift-tubes of 4.9 mm diameter (see Figure 2.9, a). As a drift medium, a mixture of Ar (70%), CO_2 (28.5%) and O_2 (1.5%) is used to provide a drift time below 50 ns and spatial hit resolution

of $200\ \mu\text{m}$.

The OT and IT have the same $x - u - v - x$ layout as the one described for the TT.

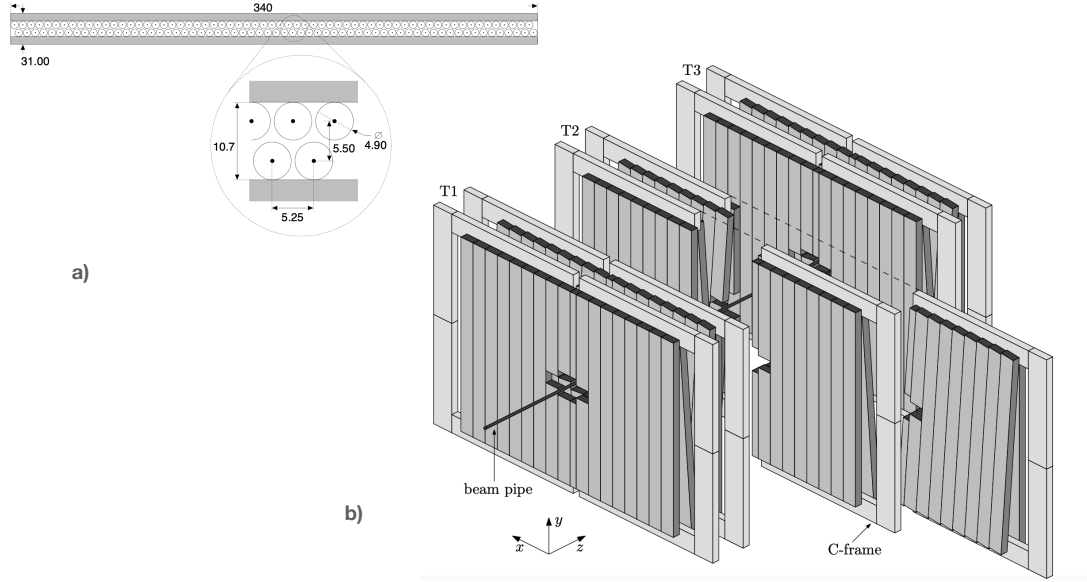


Figure 2.9 – The OT module cross section (a) and the 3D layout (b) [41].

Track reconstruction

All recorded hits from the aforementioned tracking subdetectors are combined to reconstruct trajectories of the charged particles traversing LHCb. Depending on which subsystem they were reconstructed with or on the path they made through the spectrometer, tracks are divided into the following categories, as illustrated in Figure 2.6:

- **Long tracks** traverse the whole detector, leaving hits in both the VELO and the T stations, and optionally in the TT. They travel along the full magnetic field, therefore have the most precise momentum estimate and are the most essential for the physics analyses.
- **Downstream tracks** pass through the TT and T stations. They are reconstructed without the hits from the VELO, which leads to worsened resolution on momentum, impact parameter, and consequently mass of the candidates they form. Nevertheless, these tracks are important for the reconstruction of long-lived particles that decay outside the VELO.
- **Upstream tracks** pass only through the VELO and TT stations. If a particle did not reach the T stations it is usually due to the too low momentum to traverse the magnetic field. Although, they pass through the RICH1 detector and used to study the backgrounds in the particle identification algorithms.
- **VELO tracks** are passing through the VELO only, which are usually large-angle or back-

ward tracks, and are outside the acceptance of other subdetectors. They are used to reconstruct the PV.

- **T tracks** are typically produced in secondary interactions and pass only through the T stations.

Performance

The great performance in the measurement of the low-level objects (such as hits, clusters, tracks etc) and thorough alignment of the aforementioned subsystems leads to an excellent performance of the spectrometer in high-level physics measurements. The full performance summary is provided in [43] but in the scope of this thesis it is important to highlight an excellent momentum resolution of 0.5 – 1%, which allows for a measurement of the mass of decaying particles with an exceptional precision (see Figure 2.10). This makes it possible to employ a powerful approach of searching for the new decaying states in the mass spectrum, as discussed in Section 4.7.

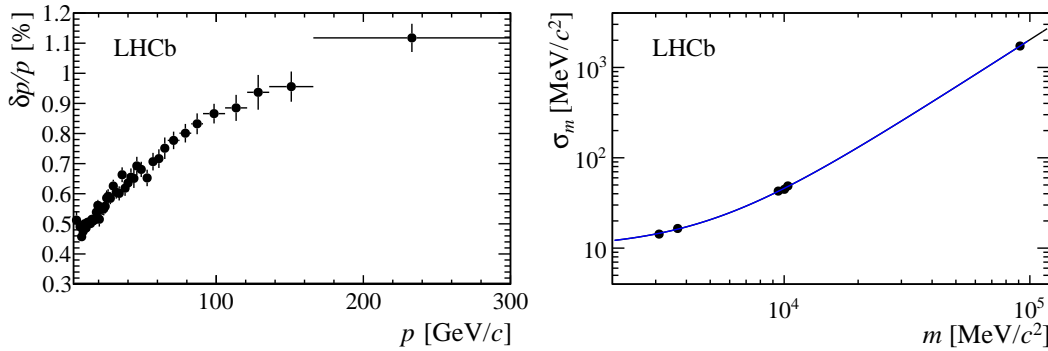


Figure 2.10 – Relative momentum resolution versus momentum (left) for the long tracks in the LHCb data obtained using J/ψ decays. Mass resolution (right) as a function of the mass of the dimuon resonance. It is evaluated for six different resonances decaying to pair of muons: the J/ψ , $\psi(2S)$, $\Upsilon(1S)$, $\Upsilon(2S)$ and $\Upsilon(3S)$ mesons, and the Z^0 boson [43].

2.2.2 Calorimeters

In general terms, calorimeter in high energy physics experiment measures the energy deposited by a neutral or charged particle that passes through or is absorbed in the calorimeter medium. Different species of particles have different ways of interacting with matter:

- **Electrons** have mainly radiative losses, emitting high energy **photons** (bremsstrahlung), which at high energies predominantly interact by producing e^+e^- pairs. Then, if the energy is large enough, these particles produce a cascade of photons and electrons forming an electromagnetic shower with a total energy equal to the one of initial particle. To characterise an electromagnetic shower, a radiation length (X_0) is used. It is defined by a length of absorber that is needed to reduce the energy of an incoming electron by a

factor of e . Additionally, when an electron propagates through the spectrometer, it emits bremsstrahlung photons that have to be detected in order to measure the full energy of the candidate.

- **Hadrons**, when colliding with nuclei of the calorimeter material, produce secondary particles such as pions, kaons, and other hadrons. Then, these secondaries produce a cascade of particles called hadronic shower, which due to the nature of inelastic interactions spreads further and wider than the electromagnetic one. For this reason, hadrons are harder to stop and require a hadronic calorimeter made of a denser material right after the electromagnetic one. Hadronic showers are characterised by an interaction length λ_I in the material, which is the average distance that a high-energy hadron can travel before undergoing an inelastic collision or other interaction resulting into production of the secondaries.
- **Muons** have much smaller energy loss comparing to the other particles, and they mainly penetrate the whole detector and are detected by the muon stations after the calorimeter.

The calorimeter system of LHCb is composed of four systems [41]: the Scintillating Pads Detector (SPD), Pre-Shower (PS), Electromagnetic Calorimeter (ECAL) and Hadronic Calorimeter (HCAL), as shown in Figure 2.2. It performs several functions: selects high transverse energy (E_T) hadron, electron and photon candidates for the first trigger level (L0); provides the identification of hadrons, electrons and photons as well as provides an energy measurement associated with a position.

Depending on the nature and energy of the incoming particle it has the energy loss of a different type, and this requires a complex construction of the calorimetry system. Structure of the LHCb calorimeter was designed to keep an optimal identification of electrons, which is the most demanding. The SPD and the PS are made of a scintillator tiles, that are separated by a thin lead layer. The ECAL and HCAL are composed of the shashlik type cells, which are made of the alternating layers of an active material (plastic scintillator) and of a passive material (heavy absorber). In all four systems, the light produced in the plastic scintillators is transmitted to the photomultiplier tubes (PMT) by optical fibers coupled to them.

To reject a high background of charged pions, detected electromagnetic shower has to be longitudinally segmented. This is done by adding the PS before the ECAL, where the lead thickness is optimised to compromise between the trigger performance and the energy resolution. The electron trigger has to be capable of rejecting a background of high E_T π^0 's, which is achieved by adding the SPD plane to select charged particles. To achieve an optimal energy resolution calorimeter has to fully absorb the showers from high energy photons. Hence, the ECAL thickness was chosen to be 25 radiation lengths. At the same time, there were no trigger requirements on the containment of the hadronic showers, so the HCAL thickness is set to 5.6 hadronic interaction lengths, and is mainly constrained by the space limitations.

Similarly to the tracking stations, all the calorimeter subsystems adopt a variable lateral segmentation.

2.2.3 The Muon system

As was mentioned before, muons pass through the whole detector and require an additional subdetector to be identified. Indeed, if one detects a particle after the thick layers of the absorber (or calorimeter), it is most likely a muon. This very simple principle lays in the base of a muon triggering at LHCb introduced in Section 2.2.5. The muon system, as shown in Figure 2.11, has five rectangular stations M1-M5, placed along the beam axis, with 80 cm thick iron absorber (muon filters) from station two to five.

Station M1 is placed in front of the calorimeter and is used for improving the measurement of muon p_T in the trigger. This station, due to the higher occupancy, also uses a different technology compared to M2-M5. It employs triple Gas Electron Multiplier (GEM) detector, while the latter ones are based on Multi Wire Proportional Chambers (MWPC). Stations M1-M3 have a higher spatial resolution along the bending x plane because they are used to calculate the p_T of the muon candidate at the trigger level with a resolution of 20%. Hence, stations M4 and M5, with lower spatial resolution, are used for the identification of penetrating particles and require a muon to have a momentum of 6 GeV to fire all five stations.

Each muon station has four regions (see Figure 2.11, right) R1, R2, R3, R4 that have segmentation ratios of 1:2:4:8. This ensures the flux and channel occupancy to be roughly the same over all the regions.

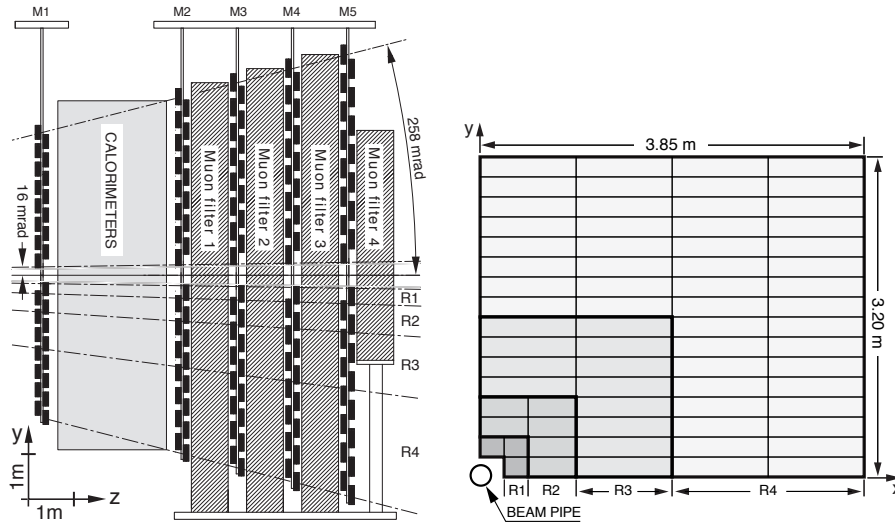


Figure 2.11 – Side view of the muon system (left). Front view of a quadrant of a muon station (right), where each rectangle represents one chamber [51]

2.2.4 Particle Identification

One of the notable examples of particle identification (PID) experiments that comes to mind is the discovery of the positron, which is shown in Figure 2.12, left, where unknown at that time charged candidate behaves under applied magnetic field as a positively charged particle. It has much smaller mass than the already known proton, which is deduced by the track curvatures

2.2. The Large Hadron Collider Beauty experiment

and the energy loss induced by a 6 mm lead plate. Since then, similar ideas are followed in experimental HEP where a traditional particle physics experiment is usually designed to have a layered structure as it is summarized in a sketch 2.12, right. This is done not only to allow for an identification of different signatures in different parts of the detector, but also to place the low material budgeted detectors first, so they would not affect the measurement of the next subdetectors.

PID is a key feature of LHCb, as it is essential to the physics programme of the experiment

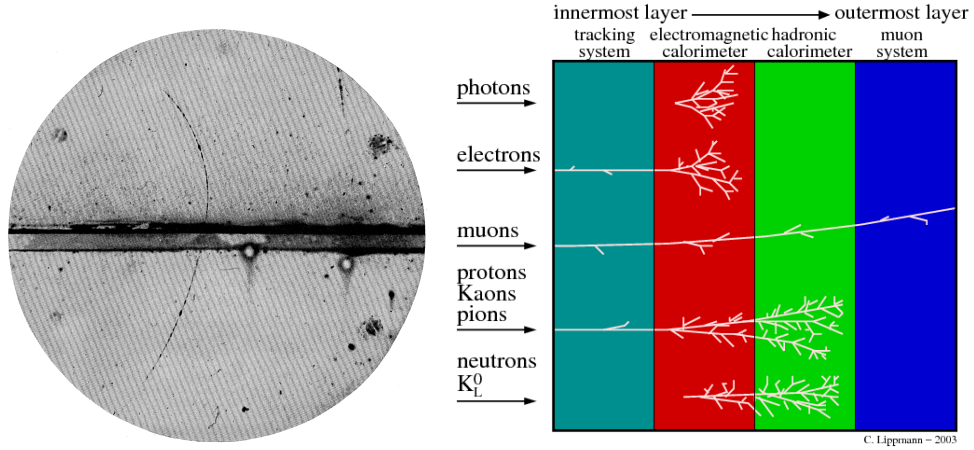


Figure 2.12 – Cloud chamber picture of cosmic radiation from 1932 [52] (left). Sketch of a traditional particle physics experiment (right), where each particle could be identified by its own signature that it leaves in a certain subdetector [53].

to distinguish between, *e.g.*, pions and kaons in *b*-hadron decays. While the calorimeter and the muon stations contribute to the identification neutral particles and muons, the LHCb experiment has two dedicated subdetectors for the identification of charged hadrons.

The Ring-Imaging Cherenkov (RICH) detector is based on Cherenkov radiation. When a charged particle travels in a medium with a higher velocity v than the speed of light c_m in that material, it emits a cone of blue light with an opening θ_c , defined as:

$$\cos\theta_c = \frac{1}{n\beta}, \quad (2.2)$$

where n is the refractive index of that material, also called the radiator, and $\beta = v/c$. This cone of light is then focused and transported by a system of spherical and plane mirrors on the photodetectors to focus the light in a shape of a ring, with a radius proportional to θ_c . This allows for the measurement of the particle's velocity, which in combination with the momentum as measured by the tracking system, provides us its mass for the identification.

At small angles with respect to the beam axis, the momentum spectrum is harder, while it is softer at large angles. The momentum range of a single Cherenkov radiator is constrained, since for a single value of n , according to Equation (2.2), emission angles at high momentum

will accumulate to a limit value and make discrimination impossible. Therefore, the LHCb detector features two complementary RICH subdetectors working with different acceptance angles to cover the range of interest. Both RICH subdetectors are using the Hybrid Photon Detectors (HPDs) to detect Cherenkov photons in the wavelength of 200-600 nm. To reconstruct the rings, HPDs are designed to measure the spatial position of the photons. The HPD is a vacuum photon detector in which a photoelectron, similarly to the classical PMT, released from the photocathode, is accelerated by a high voltage of 10 to 20 kV onto a reverse-biased silicon detector. The silicon detector, which is an array of 32x32 pixels ($500 \times 500 \mu\text{m}$ each), provides the needed spatial imaging.

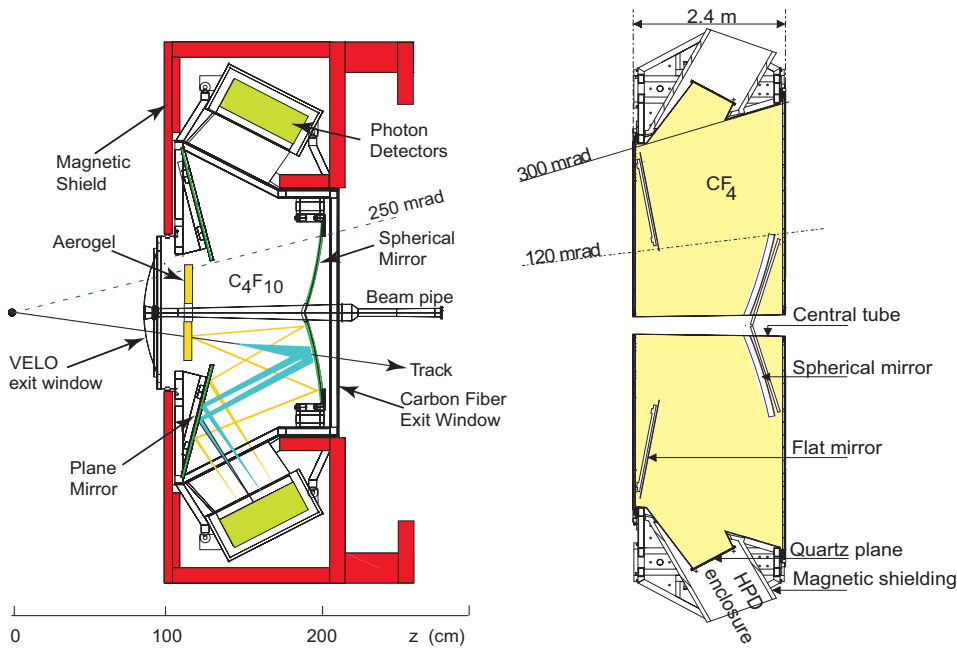


Figure 2.13 – Side view schematic of the RICH1 (left) and top view schematic of the RICH2 (right) detectors [41].

RICH 1

The upstream detector, RICH1, which is located before the magnet, covers the low momentum particles range of 1–60 GeV employing aerogel and C_4F_{10} radiators (see Figure 2.13, left). In the RICH1 the optical layout is vertical and is designed to reflect the image out of the spectrometer acceptance. This is caused by the need of magnetic shielding around the HPDs for proper functioning, which would produce a lot of secondary particles in the acceptance if placed there.

RICH 2

The downstream detector, RICH2, which is located after the magnet, covers the momentum particles range from 15 GeV up to and beyond 100 GeV using CF_4 radiator (see Figure 2.13, right), and unlike the RICH1 has horizontal layout of the optical system. The total radiation length of RICH2 with the gas radiator is about $0.15 X_0$, where X_0 is the radiation length defined in Section 2.2.2.

Likelihood-based PID

As seen in Figure 2.14, left, when the measured Cherenkov angles are combined with the reconstructed momentum, charged particles are well distinguished for a certain momentum range. To classify all the particle species, an overall event log-likelihood algorithm is used, where all the tracks that have signatures in both RICH detectors are considered simultaneously. At first, all the tracks are assigned a default pion hypothesis, since they are the most commonly produced particles in the pp collision. This log-likelihood is computed for a given set of hypotheses from the distribution of Cherenkov photons hits and associated tracks and their errors. This likelihood is then recomputed iteratively for each track in the event, changing the mass hypothesis to μ , e , π , K and proton, and repeated until the maximum likelihood is found. The final result of the PID are the differences in the log-likelihood values $\Delta \log \mathcal{L}$, which give the change in the overall event log-likelihood when that track is changed from the pion hypothesis to the other considered before. Performance of this algorithm is shown in Figure 2.14, right, where the kaon PID efficiency for different thresholds of $\Delta \log \mathcal{L}(K - \pi)$ is computed.

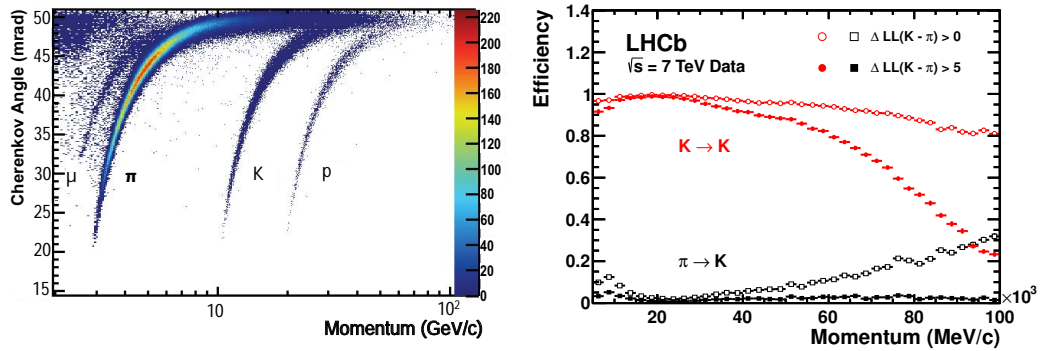


Figure 2.14 – Reconstructed Cherenkov angle as a function of track momentum in the C_4F_{10} radiator (left). Kaon identification efficiency and pion misidentification rate measured on data as a function of particle momentum (right) [54].

Inputs from the calorimeter system to PID

As described in Section 2.2.2, the calorimeter system is used to identify photons, electrons and π^0 candidates. Neutral particles are identified by the absence of a matching track to the calorimeter cluster. The shape of that cluster is then used to distinguish between photons and π^0 candidates. Additionally, for the photon hypothesis, the possibility of photon conversion in the upstream material is taken into account. To identify electrons, information from the ECAL, PS and HCAL is combined into signal and background likelihood distribution, and then the log-likelihood difference between electrons and hadrons is derived.

Inputs from the muon system to PID

If a track reconstructed by the tracking system has associated hits around its extrapolated trajectory in the muon system, it is identified as a muon. An algorithm searches for hits within rectangular windows around the extrapolation points. The xy coordinates of the windows are parameterised as a function of the track momentum at each station. This parameterisation is optimised to maximise the efficiency and to minimise the misidentification rate. The same criteria are applied to define the number of stations required to have hits from a track.

Combined PID

To make PID more robust, information from the muon, RICH, and calorimeter systems is combined into a set of more powerful variables. There are two different approaches. The first one is based on the same idea as the one described in Section 2.2.4, combining the likelihood information from each subdetector and adding it linearly, to form a combined likelihood,

$$\Delta \log \mathcal{L}_{comb}(X - \pi), \quad (2.3)$$

with X being either e , μ , K or p . The second approach, in addition to the PID likelihoods, includes correlations between the subdetectors and supplementary kinematic information. This set of variables is treated using multivariate techniques, providing a single probability value for each particle X , defined as $ProbNN_X$. These global approaches to PID reduce the hadrons misidentification probabilities to 0.6%, with a total muon efficiency greater than 93%. And at the end, 60% of the muon misidentification comes from pions and kaons decaying in flight into muons.

2.2.5 The trigger system

The trigger selects events containing interactions that are of potential interest for physics analysis. It is designed to have high efficiency, which should be precisely known, and to not introduce any bias affecting the physics result. At the same time, there are present high-rate physics processes that are not relevant to the measurement program and must be rejected

or minimised. Since the trigger algorithms have to be executed at a high rate, they need to be fast and efficient. The pp collisions at the LHCb interaction point happen at a 40 MHz repetition rate, and to comply with all aforementioned requirements, the trigger system of LHCb is composed of several dedicated stages, which are outlined in Figure 2.15.

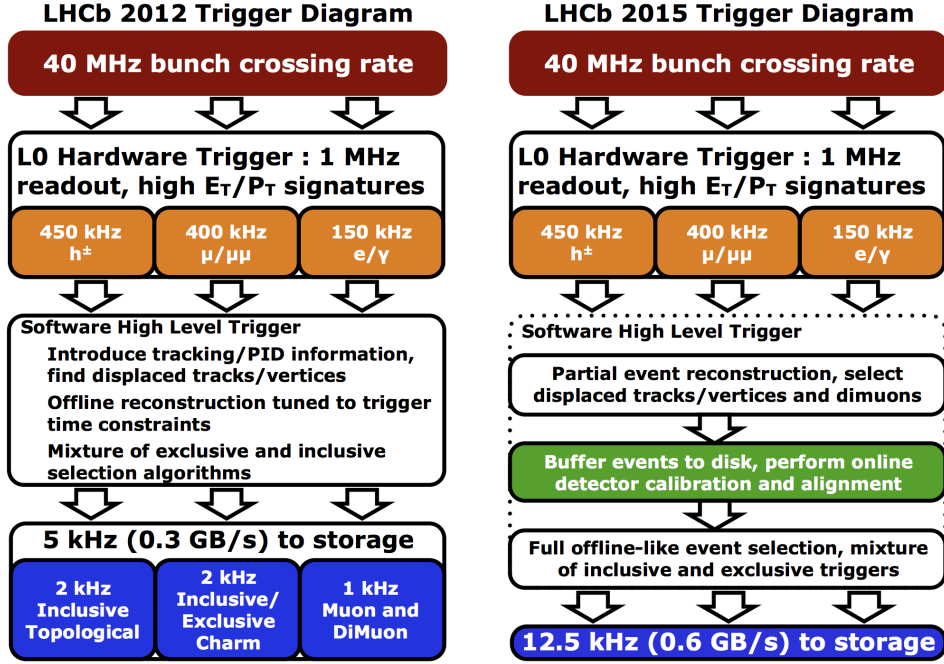


Figure 2.15 – An outline of the LHCb trigger levels in Run 1 (left), which was improved by implementation of the online calibration and alignment in Run 2 (right), increasing the rate of saved events from 5 kHz to 12.5 kHz [55].

The Level-0 (L0) is a hardware-based trigger. It is implemented on the Field-Programmable Gate Arrays (FPGAs) that have very low latency, can perform parallel computing and are re-programmable according to the user case. This allows to collect the most essential basic information from the needed subdetectors and almost instantly apply a decision on the event. The L0 algorithms, or trigger lines, use information from the SPD, PS, ECAL, HCAL and Muon system. The L0Hadron line selects the highest E_T cluster that also has a matching ECAL cluster. The L0Photon line selects the highest E_T ECAL cluster that has 1 or 2 PS hits associated to the ECAL ones and no hit in the SPD. The L0Electron line is similar to L0Photon except that it does require a hit in the SPD detector. If the corresponding configurable E_T threshold is crossed, the candidate fires the trigger line. Additionally, a total number of the SPD hits is computed and is used to reject events with a too high multiplicity. Those events are too complex to be handled timely by the trigger system, and would saturate the available computation time in the next trigger level. The L0 stage reduces the event rate from 40 MHz to 1 MHz.

The High Level Trigger (HLT) is a set of software algorithms running on the event filter farm,

which takes a further decision on events accepted by L0. It has 29,500 instances, each running the trigger algorithms that have selection parameters for a specific class of events. As the L0 stage has significantly reduced the event rate, the HLT algorithms have more time to work with a higher level objects than the ones used in L0. The HLT is divided in two levels. In the first one (HLT1), the VELO tracks are reconstructed, as well as the PVs, and the impact parameter information of the VELO tracks with respect to those PVs is calculated. Also, VELO tracks are combined with the information from the other tracking stations to form the Long tracks. The second level (HLT2) does the forward tracking of all VELO tracks, reconstructs the secondary vertexes (SV), and applies a set of decay-specific selections using high-level objects, such as reconstructed mass, flight distance, or decay topologies.

Events that pass the HLT selections are stored and later processed with a more accurate alignment and calibration of the subdetectors, that slightly increases accuracy, executed PID hypotheses evaluation and other computationally heavy algorithms. The next step is the so-called data *stripping*, which is introduced in Section 2.2.6.

Trigger decision categories

A reconstructed signal candidate might be a part of the trigger decision, *i.e.* fire a trigger line, or otherwise be a part of an event where some other (not relevant to the signal selection) trigger line was fired and caused the event to be saved. Therefore, as defined in [56], the following categories exist:

- Triggered On Signal (TOS): events for which the presence of the signal is sufficient to generate a positive trigger decision.
- Triggered Independent of Signal (TIS): the “rest” of the event is sufficient to generate a positive trigger decision, where the rest of the event is defined through an operational procedure consisting in removing the signal and all detector hits belonging to it.
- Triggered On Both (TOB): these are events that are neither TIS nor TOS; neither the presence of the signal alone nor the rest of the event alone are sufficient to generate a positive trigger decision, but rather both are necessary.

There is a set of requirements to define to which category a triggered candidate belongs. Briefly, if a reconstructed object, such as a track, has more than around 70% (depending on the subdetector) match of the online reconstructed hits to the set of all the hits from all offline reconstructed signal parts, this candidate is marked as TOS. For a composite candidate, for example a topological line, the whole combination of all individual candidates in the trigger is compared to the set of offline candidates.

2.2.6 Data processing and simulation

Reconstruction and Stripping

The LHC provides pp collisions to LHCb 40 million times per second, which would result in ~ 1 TB of data saved every second if we were to accept all the events. After the trigger stages, collisions recorded by the LHCb detector go through a specific data flow developed to have a high data-taking efficiency and data quality. Raw events containing reconstructed charged and neutral tracks, PID information etc. are stored in Data Summary Tape (DST) files, which still takes massive amount of storage and are not freely available to the physicists due to computing restrictions. To further reduce it, data are filtered through a set of selection called the Stripping, where the analysis-specific combination algorithms are applied and events are stored in several streams that are grouped by the final states or containing similar selections. Then, this *stripped* data are saved on specialized GRID storage, making it available to the users.

Simulation

Monte-Carlo (MC) event simulation is crucial to high energy particle physics. It is used to simulate the features of the signal processes and their backgrounds and to relate experimentally measured variables to the parameters of a probed theory. Development of every HEP experiment starts with simulation as it helps to define the operational requirements in a scope of the physics program. LHCb is not an exception and has its own complex simulation framework which is organised in multiple steps, that are somehow following the chronology of particles “lifetime”:

- Proton-proton collisions are simulated with PYTHIA [57] and a specific to B_c^+ mesons generator BCVEGPY [58].
- Decays of produced particles are simulated with EvtGen [59] and the final-state radiation is described by Photos [60].
- Then, as particles propagate through the detector, their interaction with material and subdetectors responses are simulated with Geant4 [61] framework.

After that, the generated events are passed through the emulation of trigger, reconstruction and stripping stages that are identical to the ones used to process data coming from the detector. Due to the theoretical or detector models limitations several physics processes require additional calibration or corrections to the MC simulation and performed on per analysis basis. Such corrections are required for the PID variables, event multiplicity, trigger efficiency etc., and are usually evaluated on data samples of already well studied decays. Mechanisms of several aforementioned corrections are described in the following chapters as they were relevant for this analysis.

MC truth variables

Such a complex scheme of preprocessing simulated events is not unnatural for a HEP experiment. In this way, simulated samples resemble reconstructed data of well measured processes as much as possible allowing for MC samples to be used in estimation of crucial processes in the analyses. Features of simulated particles that were emulated using reconstruction software form the reconstructed level information of an event, while the same exact features that were set by a particle generator are called the *truth* variables.

2.3 Luminosity measurement

The precise determination of instantaneous luminosity \mathcal{L} is crucial for the LHCb experiment, not only for the reliable measurement of the cross section of studied processes, which is heavily relying on the values of integrated luminosity, but also to ensure the correct leveling of the \mathcal{L} -value at the IP. The luminosity of a machine with number of colliding bunches n_b that operates with the revolution frequency of f is defined as

$$\mathcal{L} = \frac{\mu \cdot n_b \cdot f}{\sigma}, \quad (2.4)$$

where μ is the average number of inelastic collisions per bunch-crossing and σ is the cross section of a process which needs to be determined. This equation has to be slightly modified in order to shift from the absolute values μ and σ to the ones measured by the experiment (visible). When the efficiency of the event observation by the experiment, ϵ , is introduced the equation above transforms into

$$\mathcal{L} = \frac{\mu \cdot n_b \cdot f}{\sigma} = \frac{\mu_{vis} \cdot n_b \cdot f}{\epsilon \sigma} = \frac{\mu_{vis} \cdot n_b \cdot f}{\sigma_{vis}}, \quad (2.5)$$

with $\mu_{vis} \equiv \epsilon \mu$ and $\sigma_{vis} \equiv \epsilon \sigma$ being the average number of visible collisions and the visible cross section, respectively. The luminosity at LHCb is measured by counting the visible interactions per bunch-crossing μ_{vis} , defined by the presence of hits in the detector. Despite the large intensity of colliding beams at the LHC ($\sim 10^{11}$ protons), in the bunch-bunch collision, only few protons actually collide and produce the detected final states. For this reason the “logZero” method [62, 63] is used, which is relying on Poisson statistics to count the fraction of events without interaction P_0 , and is defined as

$$\mu_{vis} = -\log P_0 = -\log \frac{N_0}{N} - \frac{1}{2} \left(\frac{1}{N_0} - \frac{1}{N} \right), \quad (2.6)$$

where N_0 is a number of empty events, and N is the total number of events. The second term of the equation describes the second-order correction.

The last missing bit is the σ_{vis} value that is determined during the dedicated luminosity calibrations. One of the methods used at LHCb is the van der Meer scan [64]. This method

is performed for two colliding beams, by varying the position of one beam with respect to the other one and registering the change of the interactions rate. This technique measures the integral of the beam overlap assuming that the particle density in the colliding beams is distributed according to the Gaussian. For the given luminosity counter (subdetector) the calibrated cross section is defined as

$$\sigma = \iint \frac{\mu(\Delta x, \Delta y)}{n_1 n_2} d\Delta x d\Delta y, \quad (2.7)$$

where $\mu/\langle n_1 n_2 \rangle$ is measured as a function of the beam separation Δx and Δy during the scan, and $\langle n_1 n_2 \rangle$ is the product of bunch populations averaged over the two colliding bunch pairs.

3 Probe for LUMinosity MEasurement in LHCb

During the Long Shutdown 2 (LS2) of the LHC, the LHCb collaboration has upgraded the detector to 40 MHz readout with a very flexible, fully software-based trigger [65]. It is estimated that this upgrade, compared to the annual signal yield obtained by LHCb in 2011, will bring a factor ten increase of the muonic b decays and more than twenty increase of the decays to hadronic final states available for an offline analysis. Additionally to the increase of sensitivity to heavy-flavour physics, the detector will be able to trigger on other signatures, for example long-lived particles. These developments also hinge on the expected 5-fold increase of instantaneous luminosity which comes with the growth of the number of visible interaction per bunch crossing, denoted by μ_{vis} .

In Run 3, LHCb uses the same luminosity leveling approach as in Run 1-2. It is also expected to have to deal with a strong variation of luminosity and accelerator-induced backgrounds. In order to ensure the correct luminosity leveling behavior, the real time measurement of the instantaneous luminosity at LHCb interaction point (IP) is crucial for the LHC. During the Run 1-2 operation, the calorimeter and the muon system hits were used to infer the average μ_{vis} at the LHCb IP, where μ_{vis} is the number of visible interactions as defined in Section 2.3. It was based on the hardware-implemented L0 trigger, which is removed in the upgraded LHCb. For this reason, a new detector capable of measuring the luminosity and beam conditions at LHCb was proposed, designed, and built. Contribution to the Probe for LUMinosity MEasurement (PLUME) detector [62] was a significant part of this thesis and is described further.

3.1 PLUME overview

The new PLUME detector is designed to fulfil the following tasks:

- deliver the online luminosity and μ_{vis} measurements for the luminosity leveling;
- perform these measurements per bunch;
- cross-check the LHC filling scheme in real time;
- measure the radiation background induced by the accelerator or bad vacuum, produce

- alarms, measure the level of the ghost charges;
- contribute to the centrality determination in the fixed-target program;
- provide accurate offline luminosity determination.

The detector concept is based on the registering Cherenkov light in a quartz radiator, induced by particles that are produced in the interaction point. A photomultiplier tube (PMT) is used as an elementary detector unit. It has a quartz entrance window with an additional coupled quartz table to act as the Cherenkov radiator. The detector unit has a small diameter of 10 mm to achieve the expected occupancy of around 1% with negligible probability of a hit by two particles within the same bunch crossing, which allows to employ the “LogZero” method [63] of luminosity measurement, defined in Section 2.3, which is based on the number of hits counting.

3.2 PLUME detector

The PLUME detector is positioned upstream from the collision region, behind the VELO, between 1680 mm and 1900 mm from the nominal interaction point. A set of elementary detectors form a two-plane hodoscope to select tracks pointing to the collision region, as shown in Figure 3.1. The presented design and the detector technology choice is based on a number of studies that are outlined in the detector proposal [66].

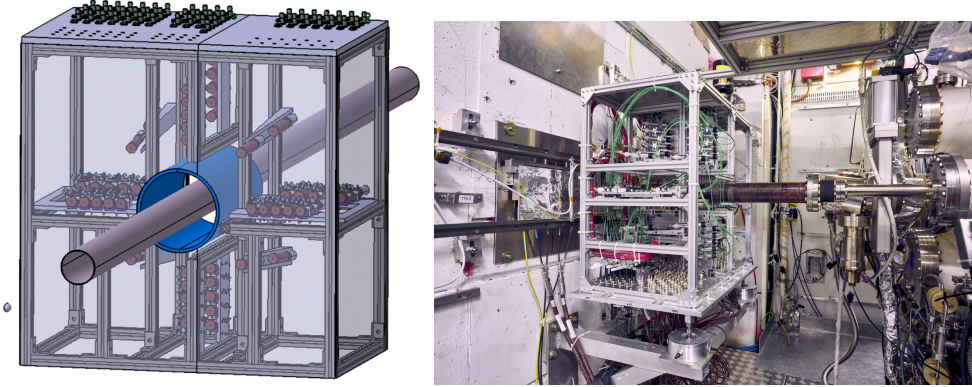


Figure 3.1 – PLUME 3D layout (left), and a picture of PLUME installed (right) around the LHCb beampipe, near the VELO [67].

Choice of detector technology

The choice of detector concept is dictated by a set of technological requirements and exploitation considerations. A short in time signal is required to be well within 25 ns window of two consecutive bunch crossings of the LHC, and to have a significant amplitude to mediate influence of the threshold drift, which is expected during the operation, on the quality of luminosity measurement. The use of radiation-resistant technology is required by the proximity to the

pp collision point.

Before converging on the current detector technology, several alternative options were developed and evaluated using a test beam [66], with electrons at an energy of 5.6 GeV:

- A quartz fiber bundle acting as the Cherenkov radiator and transporter of the generated light to a remote photon detector (see Figure 3.2), where 50 quartz fibers were bundled together and positioned at an angle of 45° with respect to the incoming particles. This placement corresponds to the Cherenkov cone opening angle that maximises the light guiding efficiency in quartz. The main idea of this setup is to use the bundle as a radiator medium and at the same time to transport collimated Cherenkov light out of the high-radiation zone. The signal shape and the histogram of integrated charge are shown in Figure 3.3, featuring very fast but rather small amplitude of the signal.

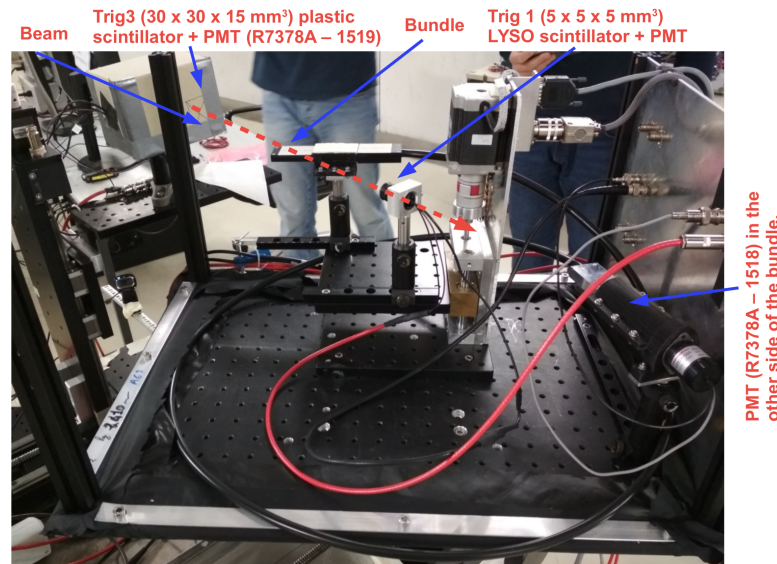


Figure 3.2 – Picture of the test setup for the quartz fibers bundle.

- The garnet scintillator coupled to the quartz fiber bundle. This material is a radiation resistant test sample with fast signal developed by the Institute of Scintillation Materials [68] for this setup. The fiber bundle from the previous option is used to transport the light produced in the garnet scintillator. In this setup, the scintillator crystal is coupled to the bundle on one side with the light being detected by a PMT coupled to the other side of the bundle (see Figure 3.4).

The small light yield, as shown in Figure 3.5, which is equal to 4 photo-electrons (p.e.) per incoming electron, could be increased by optimising the crystal size. At the same time, this setup has too long in time signal that would require optimisation of the readout, which was already predefined for this project.

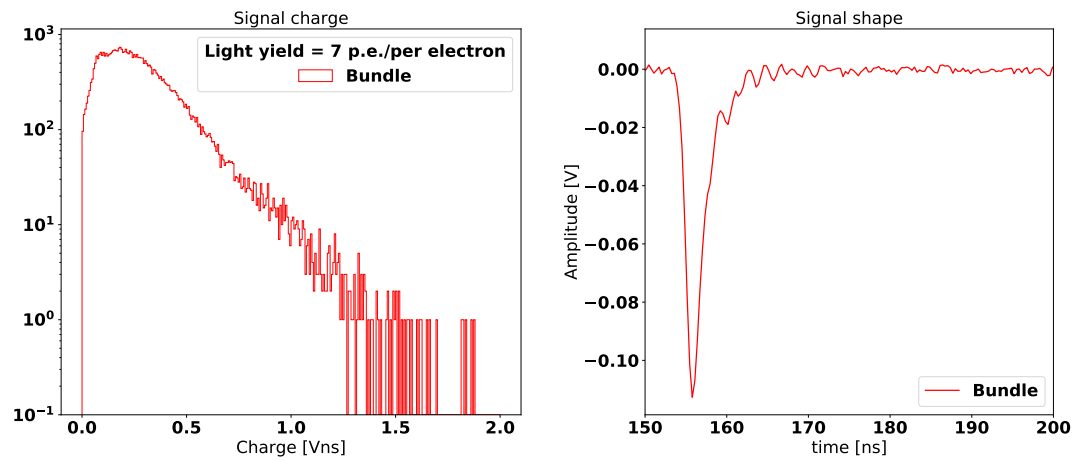


Figure 3.3 – Response (left) and signal shape (right) of the tested quartz fiber bundle.

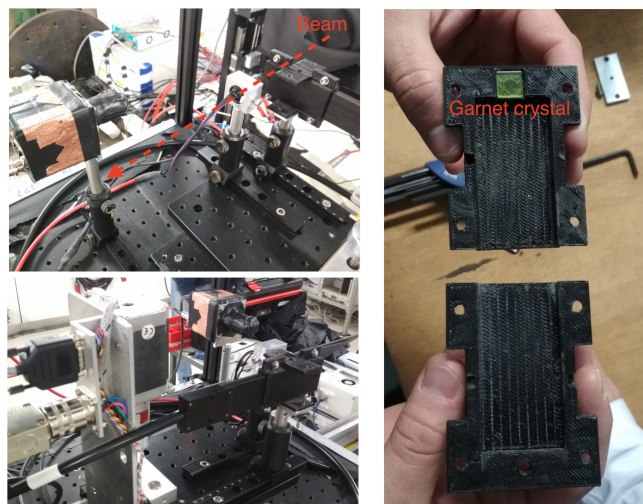


Figure 3.4 – Picture of the test setup for the bundle and garnet crystal combination.

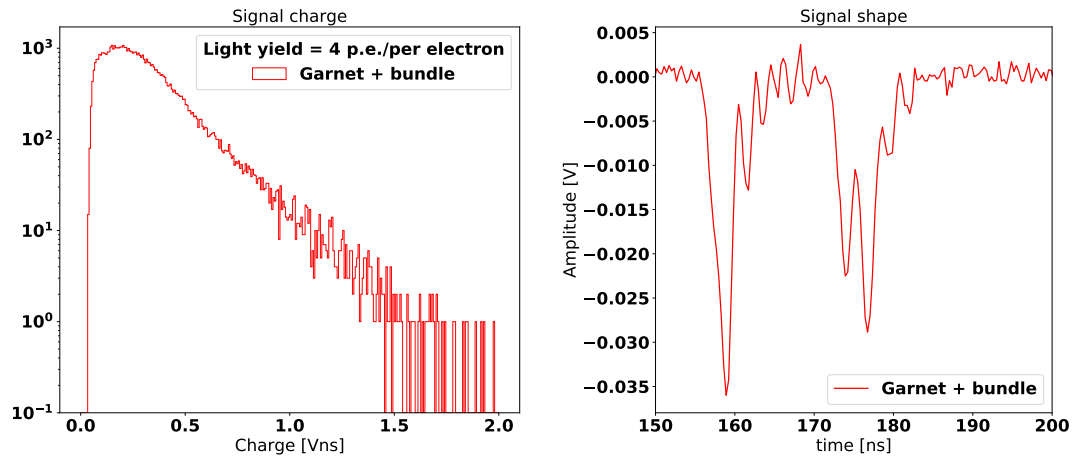


Figure 3.5 – Integrated charge (left) and signal shape (right) of the tested quartz fibre bundle, coupled to the garnet crystal.

Chapter 3. Probe for LUMinosity MEasurement in LHCb

- The garnet scintillator coupled to the PMT (see Figure 3.6). This option would require to have a radiation-resistant PMT placed directly in the PLUME acceptance. It, as expected, has the highest light yield (about 400 p.e. per incoming electron) and two (short and long) decay time components, as shown in Figure 3.7.

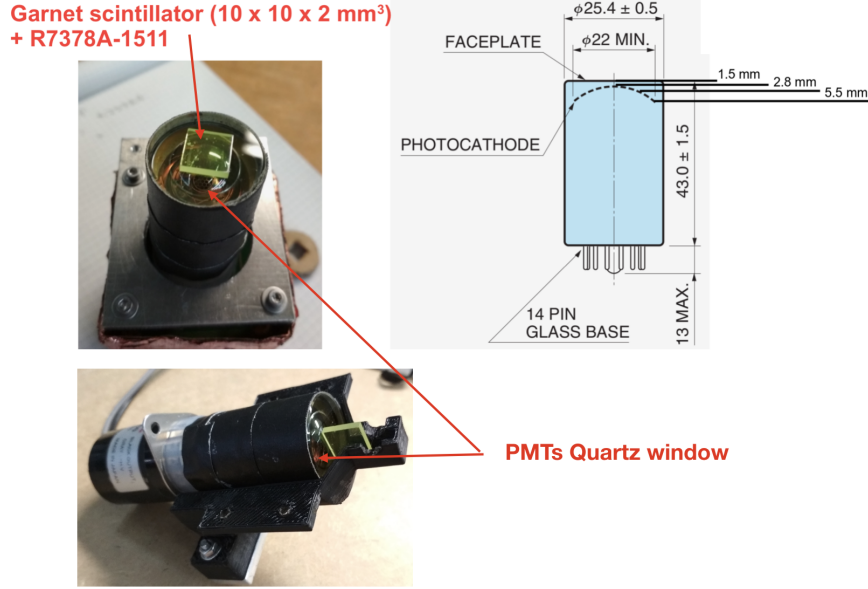


Figure 3.6 – Picture of the test setup for the Garnet crystal.

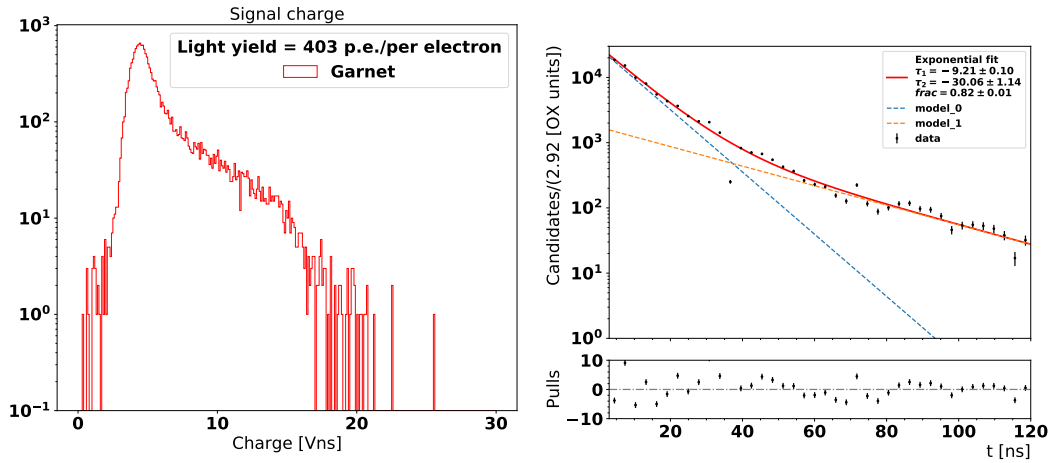


Figure 3.7 – Integrated charge (left) and signal shape (right) of the the tested Garnet crystal.

- The photomultiplier with the quartz window. This is a robust option with a very short signal pulse, which is induced by the Cherenkov light produced in the PMT quartz window, and sufficient signal amplitude (see Figure 3.8).
- A system of parabolic mirrors transporting the light produced in the Cherenkov radiator or in the scintillating crystal. We also tested an alternative way to transport the light

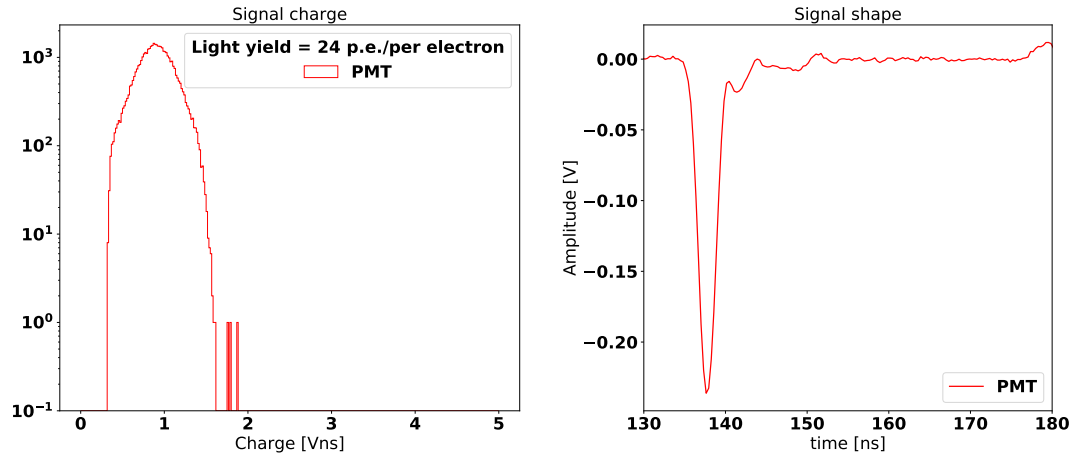


Figure 3.8 – Integrated charge (left) and 10^5 scintillator pulses (right), which are shifted, scaled and fitted to two exponential functions to retrieve the fast and slow components of the signal.

away from the radiation zone, where the detector is expected to operate. The light produced at the focal point of the first mirror is reflected and then focused onto the readout system by the second mirror, as shown in Figure 3.9. Despite the fact that the amount of light detected from the Cherenkov radiator is very small (see Figure 3.10) due to the lack of fine optical tuning of the system during the test beam, this technique can be employed when the radiation level is too high for the PMT operation.

Trig3 (30 x 30 x 15 mm³) plastic scintillator + PMT (R7378A – 1519) light transportation from Cherenkov radiator with parabolic mirrors
 Trig 1 (5 x 5 x 5 mm³) LYSO scintillator + PMT

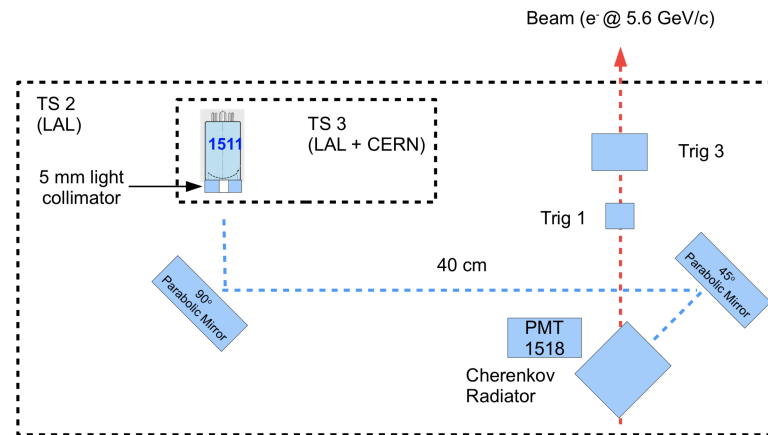


Figure 3.9 – Sketch of the test setup for the mirror configuration.

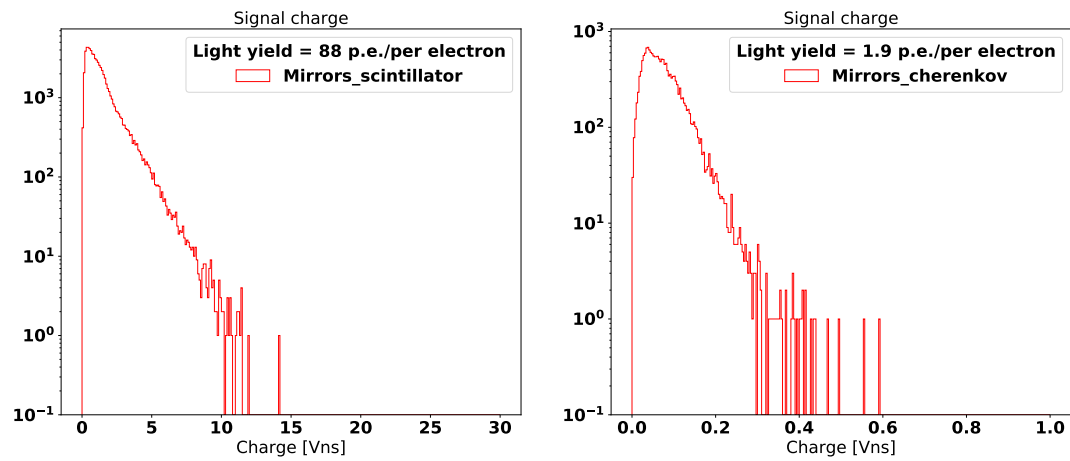


Figure 3.10 – Integrated charge with scintillator (left) and with Cherenkov radiator (right) of the mirrors setup.

PMT of choice

The PMT with a quartz radiator was chosen because of its very fast signal and a decent signal amplitude, obtained at the beam test, as shown in Figure 3.8. This combines the simplicity and radiation hardness of the setup. The HAMAMATSU R760 PMT is chosen for PLUME, as it has been already used and proven to work by the LUCID luminometer [69] of ATLAS. As shown in Figure 3.11, this PMT has a small diameter of 10 mm to comply with the low-occupancy requirements of the PLUME detector. Its quantum efficiency peaks around a wavelength of 400 nm and stays on the level above 15% for wavelengths between 200 nm and 500 nm, which is a good match for the Cherenkov emission spectrum. The starting working point of the high voltage (HV) of these PMTs is around 700 V and will be increased over time as the tubes age. Aging of the PMT is caused by two main effects: the loss of the quantum efficiency of the photocathode over time, and aging of the chain of HV dynodes, which reduces the multiplication. Therefore, an additional light injection system is used to monitor and adjust the gain as it is expected that the PMT will not only age due to the drawn current during operation, but also will get damaged by the radiation.

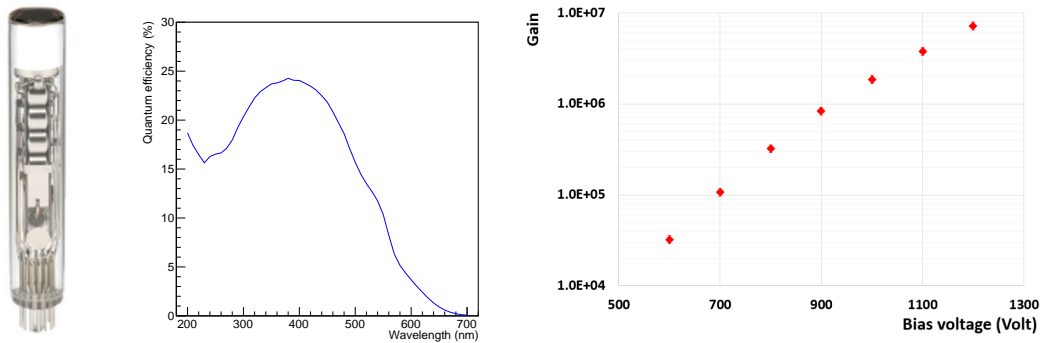


Figure 3.11 – HAMAMATSU R760 PMT [70] (left), its quantum efficiency(center) as a function of the wavelength [62], and its gain (right) as a function of the bias voltage.

The LED monitoring system

The monitoring system is developed to continuously track the PMT stability, and to provide the precise calibration of the PLUME detector for the luminosity determination. The LED calibration system monitors PMT response by sending LED light pulses through the quartz fibres to the PLUME PMTs at the regular time intervals using suitable gaps in the LHC filling scheme. The stability of the LED light pulses is in turn checked by the PIN photodiodes placed next to the LEDs at the distant location where the radiation load is reduced. Performance of this system is shown in Figure 3.12, where PMT responses are scanned with the same exact light pulses for several bias voltages showing the expected gain trends.

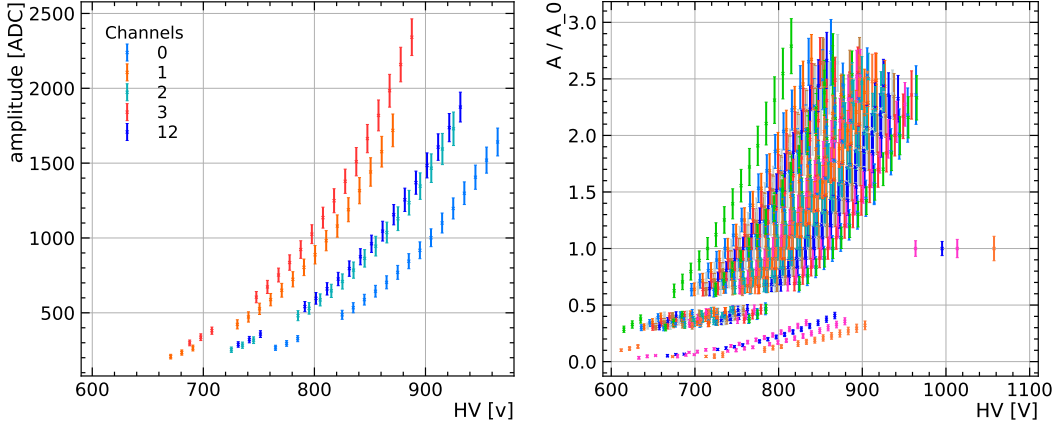


Figure 3.12 – Response of the PMTs to the LED pulses sent by the monitoring system: amplitudes of several channels as a function of the bias voltage (left), and amplitudes of all the channels of PLUME that are scaled to its nominal working points.

Elementary detection module

The elementary detection module, as shown in Figure 3.13, hosts the PMT with a quartz table attached and coupled quartz fibre that brings generated light pulses used for the calibration and monitoring.

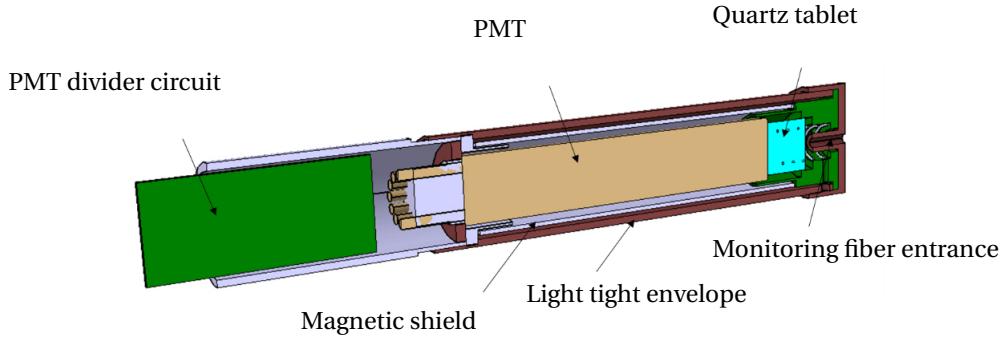


Figure 3.13 – Schematic view of the PLUME elementary detection module. The module is 153 mm long with a diameter of 24 mm.

Detector layout

A total of 48 PMTs are arranged in a projective geometry and form a two-layer, cross-shaped, hodoscope of 24 PMT pairs. The first and second layers are located at 1680 mm and 1900 mm from the IP, respectively. By requiring a coincidence in the PMT pair, it is expected to clean the data sample of the secondaries that do not originate from the IP or induced by the beam on surrounding materials. The PMT pairs are positioned at angles approximately from 5° to 10° with respect to the beam axis (see Figure 3.14), which corresponds to a pseudorapidity range of $-3.1 < \eta < -2.4$.

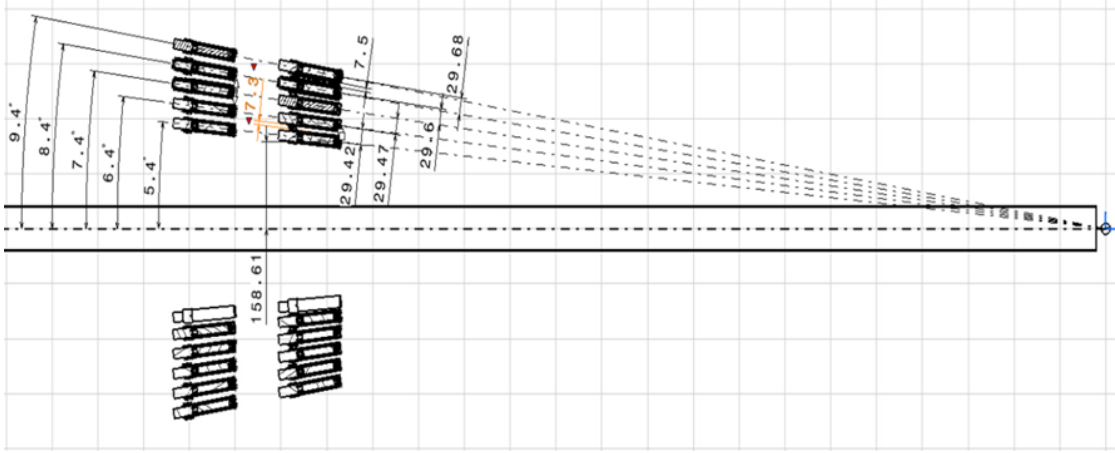


Figure 3.14 – Detector layout along the beam axis with respect to the LHCb interaction point [62].

3.3 Detector performance

In preparation to the physics data taking, the PLUME group has commissioned the detector and performed several important measurements for the absolute calibration of the online instantaneous luminosity for the $\sqrt{s} = 0.9$ TeV beam. For the measurement of instantaneous luminosity \mathcal{L} each counter needs to be calibrated, *i.e.* the value of a corresponding cross section σ , defined as

$$\mathcal{L} = f \frac{\mu}{\sigma}, \quad (3.1)$$

has to be determined. Here f is the bunch crossing rate, μ is the number of interactions. This cross section is measured using a van der Meer scan [64] introduced in Section 2.3. The evolution of the beams positions, intensity, and μ value during the scan are measured by the PLUME and the LHC machine, and are shown in Figure 3.15. In this scan the value of $\mu / \langle n_1 n_2 \rangle$ is measured for the PLUME counters, shown in Figure 3.16, which is used to compute σ . Here $\langle n_1 n_2 \rangle$ is the product of bunch populations averaged over the two colliding bunch pairs.

The PLUME subdetector measures the number of events in a 3 s time window, requiring at least one pair of two projective PMTs to have a coincidence of a signal above the threshold. Then, for each scan point, the value of μ is computed as

$$\mu = -\log \frac{N_0}{N_{\text{tot}}}, \quad (3.2)$$

where N_0 is the number of empty events, without any coincidence, and N_{tot} is a total number of bunch crossings in the time window.

The first van der Meer scan at the LHCb IP of Run 3 using PLUME as a new luminometer was performed on June 5, 2022. The PLUME detector has successfully provided online counters

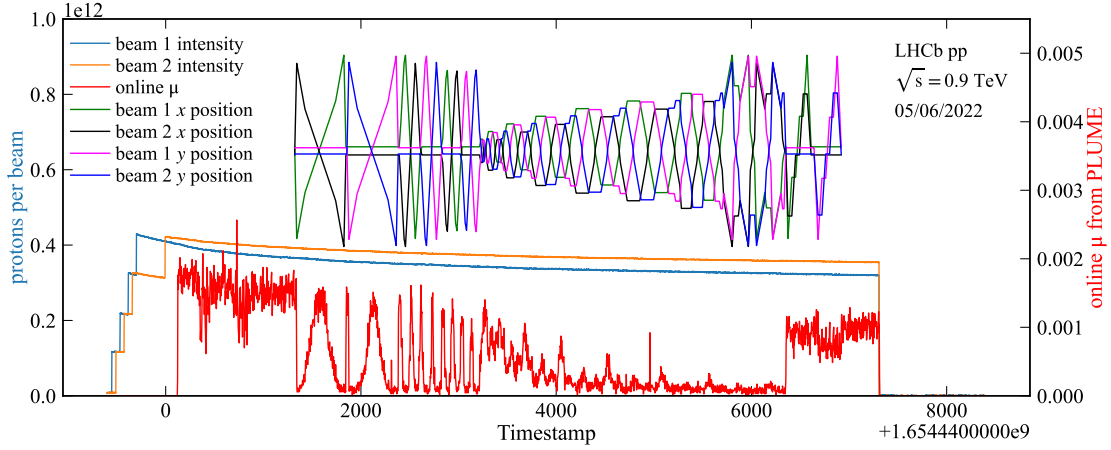


Figure 3.15 – The time evolution of various quantities measured by PLUME or provided by the LHC during the van der Meer scan [71].

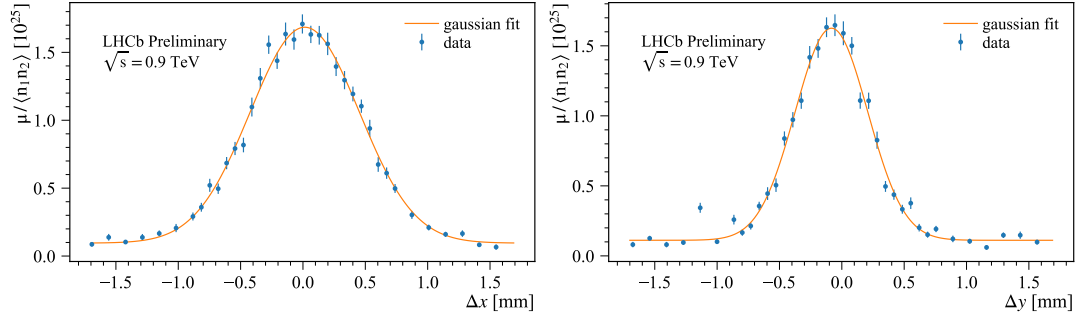


Figure 3.16 – The values of $\mu/\langle n_1 n_2 \rangle$ as a function of the beam separations Δx (left) and Δy (right), where $\langle n_1 n_2 \rangle$ is the product of bunch populations averaged over the two colliding bunch pairs [71].

and instantaneous luminosity, which was archived by the LHCb detector control system, provided to the LHC control centre, and will be used for the analysis of Run 3 data by the users.

4 Inclusive search for heavy neutral leptons in $B \rightarrow X\mu^+N$ with $N \rightarrow \mu^\pm\pi^\mp$

Motivated by the direct evidence for the BSM physics outlined in Chapter 1, possible mechanisms and phenomena of their accommodation introduced in Section 1.2 and by taking into account the numerous amount of attempts to find an experimental confirmation for these mechanisms discussed in Section 1.3, this chapter presents a search for an HNL in B decays conducted in a scope of this thesis work. Its signature consists in a heavy neutrino decaying to $\mu^\pm\pi^\mp$, while the neutrino is produced in B meson decays to μ^+N^1 or μ^+NX , where X is not reconstructed. Depending on the mixing U_μ^2 of the heavy neutral lepton with the SM muon neutrino, the $N \rightarrow \mu^\pm\pi^\mp$ vertex can be displaced from the B decay vertex or not. The dataset used was collected by the LHCb experiment during the years 2016-2018 and corresponds to an integrated luminosity of 5.0 fb^{-1} .

4.1 Search strategy

This analysis investigates HNLs with masses in the few GeV range, assuming that HNL couple only to muon neutrinos through U_μ^2 . In particular, $N \rightarrow \mu^+\pi^-$ HNL decay channel² is considered. As shown in Figure 4.1 (left), its branching ratio varies significantly within the m_N range considered, going from about 20% for HNLs of 1 GeV down to a subpercent level for HNLs with masses higher than 5 GeV. Other decay modes such as $N \rightarrow \mu^+\pi^-\pi^0$ and $N \rightarrow \mu^+\ell^-\bar{\nu}_\ell$ are expected to dominate, however, $N \rightarrow \mu^+\pi^-$ gives a cleaner detector signature and a two-body final state with charged particles. Semileptonic and final states with π^0 would significantly increase sensitivity in the mass region of interest, but they cannot be combined with an inclusive strategy of this search, that is described further. The expected N lifetime, τ_N , is predicted to vary by four orders of magnitude within the mass region considered, which is shown in Figure 4.1 (right) for a coupling $U_\mu^2 = 10^{-4}$. This directly affects the HNL detection and reconstruction efficiency in a way that low-lifetime N are hard to reconstruct among the prompt SM decays, and N with high lifetime simply fly out of the detector acceptance. This was thoroughly studied, modeled and implemented in the analysis computations.

¹ N , *i.e.* HNL, heavy neutrino

² Charge conjugation is implied throughout

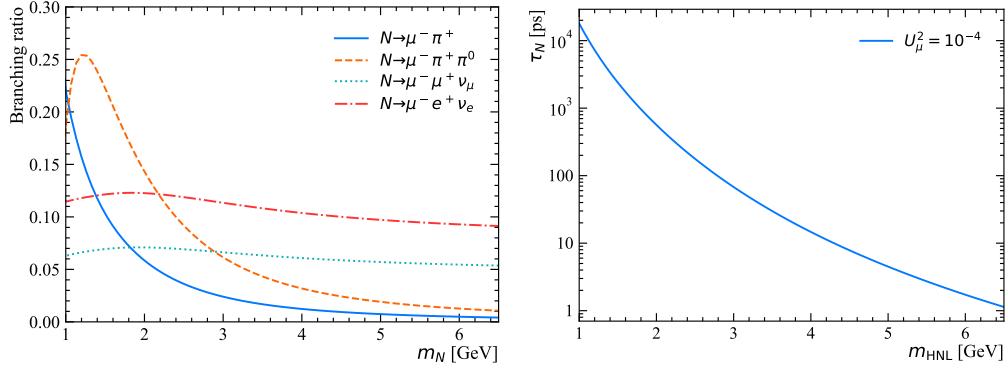


Figure 4.1 – (left) Branching ratio of the HNL decays $N \rightarrow \mu^+\pi^-$, $\mu^-\pi^+\pi^0$, $\mu^-\ell^+\bar{\nu}_\ell$. (right) HNL lifetime τ_N as a function of its mass m_N for the coupling value $U_\mu^2 = 10^{-4}$. Predictions are taken from the formulae in Ref. [24].

The current excluded regions in the U_μ^2 versus m_N parameter space were thoroughly discussed in Section 1.3, where two deterministic for this search conclusions were drawn. The HNLs that are light enough to be produced in D meson decays are strongly constrained to the level of $U_\mu^2 < 10^{-7}$ and $c\tau_N > 100$ m, which is not accessible to LHCb with current dataset. The HNLs with masses larger than about 5 GeV are produced mostly in Z or W bosons decays and are searched most effectively with the ATLAS [30, 34] and CMS [31, 35, 36] detectors. Therefore, this analysis is focused on the range of HNL masses where the production from (semi)leptonic B meson decays is the dominant HNL production process at the LHC, roughly between 2 and 5 GeV. A Feynman diagram for the considered HNL production and decay is shown in Figure 4.2.

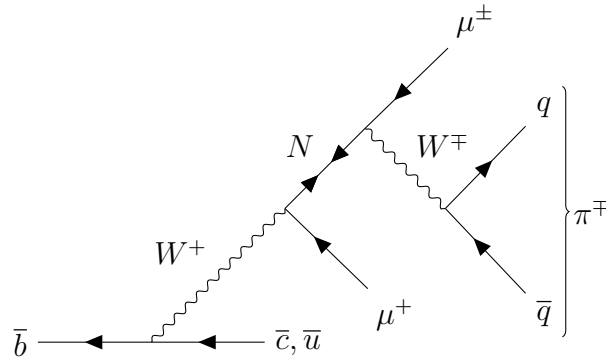


Figure 4.2 – Feynman diagram for the inclusive HNL production from B meson and its decay $N \rightarrow \mu^\pm\pi^\mp$. This represents several decay channels, depending on the hadronisation of the \bar{b} quark. The \bar{b} and \bar{c}, \bar{u} quarks can be either hadronised together in the initial-state B meson or separately in initial and final state mesons together with a spectator quark. If the HNL is of Majorana nature, the two muons can be of the same sign.

The B decays branching ratios to HNLs are also obtained from [24]. The inclusive strategy of this analysis considers B meson decay channels with the highest branching fractions for B^0 ,

B^+ , B_s^0 and B_c^+ . They include so-called leptonic decays $B_{(c)}^+ \rightarrow \mu^+ N$ and semileptonic decays $B \rightarrow h\mu^+ N$ where h is either a pseudoscalar or vector meson. The complete list of considered channels is shown in Figure 4.3 along the value of their branching ratios as a function of the HNL mass, m_N . Also, no B decay channels involving two or more mesons in addition to an HNL are considered, as their contribution is known to be negligible [24]. Despite the permille fragmentation fraction of B_c mesons measured at LHCb [72], the $B_c^+ \rightarrow \mu^+ N$ channel has to be considered as its branching ratio to HNLs is enhanced by $|V_{cb}|^2/|V_{ub}|^2$ and it is the only channel that can provide an HNL with a mass larger than 5.1 GeV.

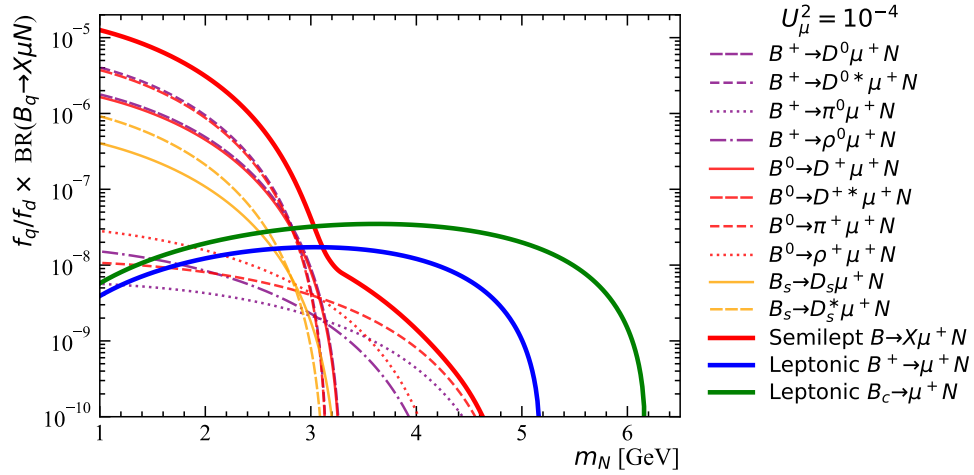


Figure 4.3 – The branching ratios of the B meson decays considered in this analysis are reported as a function of the heavy neutrino mass and for a coupling $U_\mu^2 = 10^{-4}$. For illustration purposes, the branching ratios are multiplied by the relevant B meson fragmentation fractions. The $B \rightarrow X\mu^+ N$ line denotes the sum of all the exclusive decays listed above. The predictions are obtained from the formulae detailed in [24].

The analysis is performed separately for the two fully reconstructed leptonic decays $B^+ \rightarrow \mu^+ N$ and $B_c^+ \rightarrow \mu^+ N$ and the sum of semileptonic modes treated inclusively as $B \rightarrow \mu^+ NX$, where X is not reconstructed. These three categories of decays are shown in Figure 4.4. Leptonic decays are fully reconstructed and the invariant mass $m(\pi\mu\mu)$ peaks around a corresponding B meson mass. However, semileptonic decays dominate by up to three orders of magnitude for $m_N < m_B - m_{D^{(*)}} - m_\mu$. While the semileptonic B decay is only partially reconstructed, instead, the $N \rightarrow \mu\pi$ decay peak can be used to clearly identify the signal.

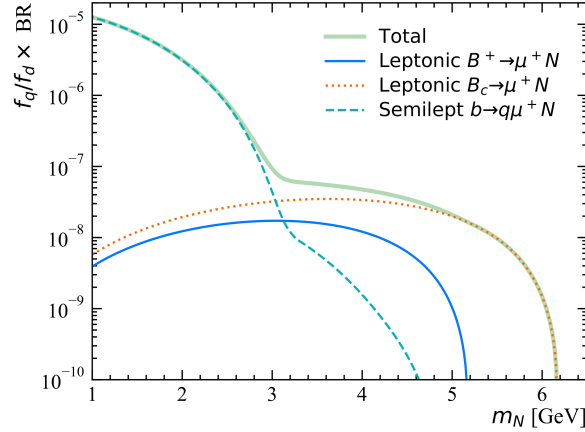


Figure 4.4 – Most important production channels of an HNL in the mass range [1, 6] GeV. The channels are the same as in Figure 4.3 but grouped into two leptonic and a semileptonic category.

4.2 Signal expectation

This search is performed blindly looking for the HNL with unknown mass, m_N , and lifetime, τ_N , where the number of observed events is extracted from the $\mu\pi$ invariant mass spectrum. The full strategy is described in Section 4.7. At the same time, this number can be predicted using the model introduced in Section 4.1, and then used to exclude the mixing parameter $|U_\mu|^2$ between the HNL and the LH muon neutrino.

The number of signal events expected in the selected data sample for each of the considered $B_q \rightarrow X\mu N$ decays is obtained with the following formula

$$N^{\text{sig}}(B_q \rightarrow X\mu N) = \mathcal{L} \sigma(pp \rightarrow B^\pm) \frac{f_q}{f_u} \mathcal{B}(B_q \rightarrow X\mu N) \mathcal{B}(N \rightarrow \mu\pi) \frac{\varepsilon(\text{FV}_{\text{HNL}})}{\varepsilon(\text{FV}_{pp \rightarrow B^\pm})} \varepsilon_{\text{sel}}, \quad (4.1)$$

where the various factors are explained in the list below.

- \mathcal{L} is the integrated luminosity of the data sample. Its calculation is detailed in Sec. 4.3.1.
- $\sigma(pp \rightarrow B^\pm) = (86.6 \pm 6.4) \mu\text{b}$ is the inclusive B^\pm cross section measurement performed by LHCb [73] with 13 TeV pp collisions in the fiducial volume (dubbed in the following $\text{FV}_{pp \rightarrow B^\pm}$) defined by $2 < y(B^\pm) < 4.5$ and $0 < p_T(B^\pm) < 40$ GeV.
- The factor f_q/f_u is the ratio of fragmentation fraction of the B_q meson considered with respect to B_u as it was measured in the LHCb acceptance. We take $f_d/f_u = 1$ assuming isospin symmetry, $f_s/f_u = 0.244 \pm 0.012$ from [74] and $f_c/f_u = (2.61 \pm 0.62) \times 10^{-3}$ from [72].
- $\mathcal{B}(B_q \rightarrow X\mu N) \mathcal{B}(N \rightarrow \mu\pi)$ is the theoretical prediction taken from [24] and detailed in Sec. 4.1. The prediction depends on the HNL mass and lifetime.
- $\frac{\varepsilon(\text{FV}_{\text{HNL}})}{\varepsilon(\text{FV}_{pp \rightarrow B^\pm})}$ is the ratio of FV efficiencies between the fiducial volume of our selection and that of the $\sigma(pp \rightarrow B^\pm Y)$ cross section measurement of [73]. Definition of the

fiducial volume and the estimation of this factor are detailed in Sections 4.4.4, 4.5.1, correspondingly.

- ε_{sel} is the total selection efficiency for signal events produced within the FV of the analysis (FV_{HNL}). This efficiency includes all online and offline requirements described in Section 4.4 and depends on the HNL mass and lifetime.

The total selection efficiency ε_{tot} calculation involves several corrections to the MC simulation that are detailed in the following sections. Namely, corrections to L0 trigger efficiency are given in Section 4.5.4, those involving the general event cut efficiency are described in Section 4.5.4 and the modeling of PID efficiencies are described in Section 4.5.4. The strong dependence of the efficiency on the HNL lifetime is obtained through the lifetime reweighting described in Section 4.5.3. Efficiencies are interpolated between the few HNL mass hypotheses of our MC samples with the method explained in Section 4.5.3. For the semileptonic partially reconstructed category $B \rightarrow X\mu N$, the total efficiency is averaged using the expected fraction of decays contributing, which depend on the HNL mass, but not on its lifetime.

4.3 Data and simulation samples

This analysis uses the pp collision data set collected by the LHCb experiment in the years 2016, 2017 and 2018, *i.e.* Run 2, corresponding to an integrated luminosity of 1.6, 1.7 and 2.1 fb⁻¹, respectively.³

4.3.1 Integrated luminosity

The total integrated luminosity is obtained by summing up the luminosity values of the data-taking runs that are used in this analysis, following the procedure indicated by the LHCb luminosity group [75]. The results are shown in Table 4.1. The total integrated luminosity is 5.04 fb⁻¹ with an uncertainty of 2%, which is determined assuming the luminosity correlation between different years of data-taking is 100%, which is conservative with respect to the estimates from [76, 77] that give around 50% correlation.

Table 4.1 – Integrated luminosity of the dataset used in this analysis.

| | 2016 | 2017 | 2018 | Total | Uncertainty |
|---|------|------|------|-------|-------------|
| Integrated luminosity [fb ⁻¹] | 1.61 | 1.45 | 1.98 | 5.04 | 2 % |

4.3.2 Simulation samples

A set of simulated samples is used to design the search, model the selection efficiency and to extract the probability density function (PDF), which describes the $\mu\pi$ mass shape. Proton collisions are simulated using PYTHIA 8 [57], while all the B meson decays to HNL shown in Figure 4.3 are simulated using EVTGEN [59]. The decays of the unreconstructed hadrons X from $B \rightarrow \mu^+ NX$ semileptonic decays are not included in EVTGEN. The HNL object is simulated in EVTGEN as a spin-0 particle with a given mass and lifetime, thus neglecting the polarisation of the spin- $\frac{1}{2}$ HNL. The simulated HNL mass hypotheses are 1.6, 2, 3, 4, 5 and 5.5 GeV. HNLs are generated with lifetimes of 100 or 1000 ps. These two values are chosen in order to efficiently cover the decay time acceptance of the detector for displaced HNL decays to long or downstream tracks. Some additional samples of 10 ps were used as well for cross-checks in the efficiency computations. A different simulation sample is generated for each HNL mass and lifetime and depending on the B meson type, B^0 , B^+ , B_s^0 or B_c^+ . Both the lepton-number-conserving $\mu^+\mu^-$ (OS) and lepton-number-violating $\mu^+\mu^+$ (SS) channels are generated. A summary of the inclusive simulation samples is given in Table 4.2. For each B meson, the generated decay channel fraction is set according to the predictions shown in Figure 4.3. In the simulation, the HNL is decayed not only to $\mu^+\pi^-$ but also to other $N \rightarrow \mu^+ h^-$ channels, with $h^- = \rho^-, D_s^-$ and D_s^{*-} . They are included so the same simulation samples could be used in the future searches to include the HNL decay channels mentioned in Figure 4.1. All

³Including data from Run 1 would provide a negligible improvement to the sensitivity (the B meson production cross section scales with the pp collision energy).

HNL decays are generated according to phase space, thus neglecting the HNL polarisation.

Table 4.2 – Summary of the simulation samples of the inclusive HNL production.

| | |
|---------------|-------------------------------------|
| B meson | B^+, B^0, B_c^+, B_s^0 |
| Muon sign | SS $\mu^+\mu^+$ and OS $\mu^+\mu^-$ |
| HNL masses | 1.6, 2, 3, 4, 5, 5.5 GeV |
| HNL lifetimes | 100, 1000 ps |

Additionally, samples of the exclusive channels $B^+ \rightarrow \mu^+ N(\rightarrow \mu^\pm \pi^\mp)$ and $B_c^+ \rightarrow \mu^+ N(\rightarrow \mu^\pm \pi^\mp)$ are used in a part of the analysis.

4.3.3 Inclusive MC model for $B \rightarrow \mu^+ NX$

In order to have a representative $B \rightarrow \mu^+ NX$ sample, the MC samples generated separately for B^+, B^0 and B_s^0 meson decays are merged into an inclusive MC model taking care of the b quark fragmentation fractions and the expected branching ratios from [24].

The relative branching ratios of different decay channels of the same B_q meson is encoded in the `DecFiles`. The `DecFile` has a configuration needed for the simulation framework, outlined in Section 2.2.6, to control the decay and to impose any event-type specific requirements (i.e. generator selection). In an early stage of the analysis, these were based on a preliminary version of the code for branching ratio predictions that needed corrections. This mismodelling is therefore corrected with the weights expressed by

$$w_{\text{BR}} = \frac{\text{correct normalized BR}}{\text{initial normalized BR}}. \quad (4.2)$$

The effect of the w_{BR} weights is shown in Figure 4.5. The relative amount of B^+, B^0 and B_s^0 meson decays in $B \rightarrow \mu^+ NX$ sample is controlled with the weights calculated as

$$w_{\text{cockt}}^q \propto \frac{\frac{f_d}{f_u} \cdot (\sum_i \text{BR}(B_q \rightarrow \mu^+ NX_i)) \cdot (\sum_j \text{BR}(N \rightarrow \mu h_j))}{N_{\text{Gen}}}, \quad (4.3)$$

where N_{Gen} is the number of generated events before generator-level selection, *i.e.* the LHCb geometrical acceptance. The LHCb geometrical acceptance selection is applied at the generator level stage of the MC production to ensure an efficient computing power usage by filtering out particles that would simply fly out of the detector geometry, which is within $1.8 < \eta < 4.9$, as specified in Section 2.2. Note that all $\rightarrow \mu h_j$ decays have to be considered for the calculation of the weight as N_{Gen} is given for the sum of them. The value of f_d/f_u is set to 1, assuming isospin symmetry. The value of f_s/f_u is taken from the LHCb measurement in [78] to be $f_s/f_u = 2 \times (0.122 \pm 0.006)$. The uncertainty on f_s/f_u is neglected since B_s^0 decays contribute only about 10% of the total $B \rightarrow \mu^+ NX$ model and have similar selection efficiency. Value

f_c/f_u is taken from [79] and is $f_c/f_u = 2.61 \pm 0.62 \times 10^{-3}$.

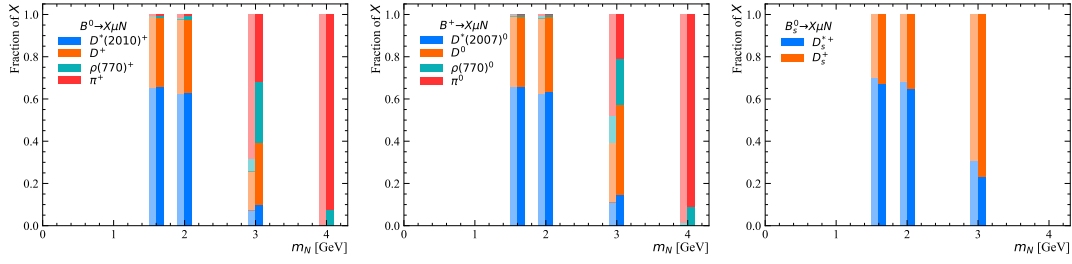


Figure 4.5 – The bar charts show the effect of the w_{BR} correction on the relative fraction of different decays contributing to the $B \rightarrow \mu^+ NX$ sample. The fraction of decays involving an X hadron are shown for each B meson and each m_N before (left bar) and after (right bar) reweighing. The largest effect involves the branching ratios of the B decays involving a ρ meson, which were too small in the configuration of the MC simulation.

4.4 Reconstruction and selection of the signal candidates

Signal candidates are selected online using the trigger lines described in Section 4.4.3. The offline selection, described in Section 4.4.4, involves stripping, preselection and a fiducial volume requirements. The data samples are split in 18 reconstruction categories that are detailed in Section 4.4.2. A multivariate analysis is performed to reduce the large background of the random tracks combinations. The training, testing and optimisation of the classifier is described in Section 4.4.5. After having drastically reduced the combinatorial background, residual misidentified background is further reduced by tightening the particle identification criteria as detailed in Section 4.4.6.

4.4.1 Signal reconstruction

This analysis is a direct search for a particle with unknown mass, m_N , and lifetime, τ_N , which partially follows the strategy outlined in [80] with several major modifications. Generally, the search involves a scan of the $\mu^+\pi^-$ invariant mass spectrum for a presence of a statistically significant excess, which means that the precise reconstruction of the signal candidates decays is necessary. To do so a collaboration-centralised application was used: DaVinci [81], which allows to analyse high-level physics information such as tracks and vertices, combine them into decay chains and to store in ROOT [82] n-tuples. This application loops over the output of a dedicated to this analysis stripping line and builds a decay chain with reconstructed particles. Our decay topology, which is shown in Figure 4.6, is built in several steps. At first, a

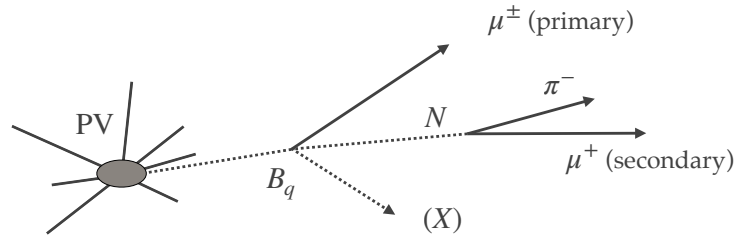


Figure 4.6 – Sketch of the decay topology studied in this analysis.

list of pions and muons is selected that pass minimal physics criteria summarised in Table 4.6. Then, a muon and pion of opposite sign are combined to build an HNL vertex (N). If resulting candidate particle fulfills the list of requirements on its mass, transverse momentum and vertex quality listed in lines 7-10 of Table 4.6, it is used for the further combination. Lower mass boundary of $m_N > 1500$ MeV is imposed by the analysis strategy and also by a very high combinatorial background below that threshold. This object is then combined with a muon to form a secondary vertex (SV) corresponding to B_q decays. Since this vertex is not fully reconstructed and misses a particle, there is a window selection on the mass of B_q candidate, $m \in \{1500, 6500\}$ MeV, instead of a tight requirement. These selections were intentionally

chosen to be loose to have a high signal efficiency, but which has a very inefficient background rejection. To overcome this, several more steps are needed that are following further.

When an event is produced using the simulation software it consists not only of tracks of the HNL decay chain, but also includes all the particles produced in the underlying pp collision. These secondaries are also simulated in the detector volume and therefore can be wrongly-assigned to the decay vertexes leading to the decay misreconstruction and biases in the efficiency measurement. Therefore, when computing the signal efficiency, a so-called “truth-matching” procedure is applied on all the reconstructed signal candidates. It uses the true IDs of mother, grandmother and daughter of the tracks to match the correct decay topology. As results of this study depicted in Figure 4.7 show, fully reconstructed vertex of $N \rightarrow \mu\pi$ has much lower misreconstruction rate in comparison to the B_q vertex which has much looser requirements.

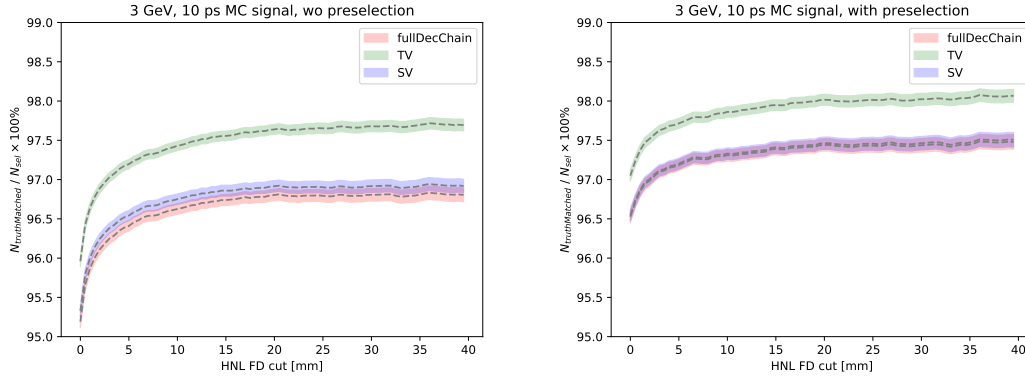


Figure 4.7 – Ratio of a number of simulated events with truth-matched vertexes to a total number of reconstructed decays as a function of the HNL flight distance threshold. Left plot is for a dataset with the stripping requirements only and right plot has additional selection chain applied that is introduced further.

4.4.2 Reconstruction categories

The analysis is performed in parallel for the final states with two same-sign (SS) and opposite-sign (OS) muons. As explained in Section 4.1, each of those final state has three categories of decays, namely two fully reconstructed leptonic decays $B^+ \rightarrow \mu^+N$ (leptonic Bu) and $B_c^+ \rightarrow \mu^+N$ (leptonic Bc) as well as the partially reconstructed semileptonic decays of the type $B \rightarrow \mu^+NX$, where X is not reconstructed (semileptonic). Furthermore, in order to enhance the sensitivity for different lifetimes, the dataset is split into three regions (bins) of the HNL flight distance. The prompt region includes events with a z component of the flight distance FD_z smaller than 20 mm and it contains about 85% of the background. Choice of the threshold value of 20 mm was also partially motivated by the result of the previously mentioned study in Figure 4.7 that shows an expected conclusion that the prompt decays have higher misreconstruction rate. Events with $FD_z > 20$ mm are split depending on whether the

4.4. Reconstruction and selection of the signal candidates

$N \rightarrow \mu\pi$ candidate is formed by using long or downstream tracks. These regions are called long and downstream, respectively. This split allows to take into account the different quality of long and downstream tracks (e.g. the $m(\mu\pi)$ resolution is worse for downstream tracks) as well as to profit from the different level of background at two displacement regions.

In conclusion, the analysis has $2 \times 3 \times 3 = 18$ reconstruction categories, having two muon charge configurations (SS $\mu^+\mu^+\pi^-$ and OS $\mu^+\mu^-\pi^+$), three categories of B decays ($B \rightarrow \mu NX$, $B^+ \rightarrow \mu N$ and $B_c^+ \rightarrow \mu N$) and finally three bins of displacement. In the following, each category is defined by the labels defined above, for example (leptonic Bu, OS, long).

4.4.3 Trigger

Table 4.3 – Overview of the used trigger lines.

| Trigger Level | Trigger Line | TOS on |
|---------------|---|---------------------------|
| L0 | <i>Muon</i> or <i>DiMuon</i> (offline $nSPD < 450$ requirement) | $\mu\mu$ |
| HLT1 | <i>TrackMuon</i> | $\mu\mu$ |
| HLT2 | <i>Topo(Mu)TwoBody</i> <i>ExoticaRHNu</i> <i>MajoranaBLambdaMuDD</i> (only SS muons, prescale 20%) | $B \rightarrow \mu\mu\pi$ |

As was already mentioned in Section 2.2.5, LHCb has the multi-stage triggering system that signal candidates have to pass for an event to be written on disc. An overview of the trigger lines used in the analysis is presented in Table 4.3. At the hardware level (L0), the signal is triggered with either one or two muons of high p_T (L0Muon with $p_T > 1.3$ GeV or L0DiMuon with $\Sigma p_T > 1.5$ GeV). It is required to have any of the two muons to be L0Muon TOS or a head of selection (b object) to fire L0DiMuon TOS line. Only TOS candidates are used in this analysis to not include a substantial amount of the di- b -hadron backgrounds, which would not be worth of a few percent gain of the trigger efficiency comparing to the case when the TIS is used as well.

These L0 trigger lines require a global event cut (GEC) on the number of hits recorded by the SPD detector. The GEC requirement is applied for some of the L0 trigger lines to discard events that consume too much time in the reconstruction due to large event multiplicities, and otherwise would overflow the HLT stage. Namely, L0Muon requires $nSPD < 450$ and L0DiMuon requires $nSPD < 900$. The different $nSPD$ requirement complicates the calculation of efficiencies while bringing a gain in the final trigger efficiency of about 7%. Therefore, an offline requirement was imposed on all events to have $nSPD < 450$. This also significantly reduces complexity of the GEC efficiency calibration introduced in Section 4.5.4.

At the first software trigger stage (HLT1), the signal is triggered by one high- p_T muon with large impact parameter (IP) using the Hlt1TrackMuon trigger line. The HLT1 requirements

are detailed in Table 4.4. At least one of the two muons from the signal candidate are required to have fired L0 and HLT1.

Table 4.4 – HLT1 trigger selection (Hlt1TrackMuon). One of the signal muons has to be responsible for triggering (TOS).

| Selection criterion | Value |
|--------------------------------------|-------------|
| $p(\mu)$ | > 6.0 GeV |
| $p_T(\mu)$ | > 1.1 GeV |
| μ Track χ^2/dof | < 3 |
| μ Ghost probability | < 0.2 |
| μ Minimum IP- χ^2 w.r.t. PV | > 35 |

The HLT1 efficiencies for all simulated masses are listed in Table 4.5. As expected, the HLT1 efficiency increases for higher masses of HNLs since the p_T of the muon coming from a displaced N vertex increases as well. At the same time a muon coming from the B_q vertex becomes softer because increasing mass of HNL limits its phase space in the $\mu\mu\pi$ combination. This effect can be seen in decreasing efficiency of DD category as there is no triggering on downstream tracks in HLT1 level of LHCb and this trigger decision fully depends on the muon from B_q vertex.

Table 4.5 – HLT1 efficiency obtained for the different SS categories of MC samples with different HNL mass. HLT1 efficiency is provided in % with the statistical uncertainty evaluated in MC simulation with L0 requirement applied. LL and DD stand for the long-long and downstream-downstream combination of the $\mu\pi$ tracks, respectively. These results are evaluated on concatenation of 100 and 1000 ps MC samples for the cross-check and illustration purposes. When evaluating MC efficiency for the computation of the final results on mass and lifetime grid, it is done per single mass/lifetime point.

| m_N , GeV | semileptonic LL | semileptonic DD | leptonicBu LL | leptonicBc LL |
|-------------|------------------|------------------|------------------|------------------|
| 1.6 | 88.23 ± 0.21 | 58.91 ± 0.34 | 93.41 ± 0.16 | 89.08 ± 0.29 |
| 2.0 | 90.18 ± 0.2 | 53.42 ± 0.4 | 94.47 ± 0.11 | 91.75 ± 0.09 |
| 3.0 | 93.46 ± 0.27 | 44.0 ± 0.79 | 95.51 ± 0.12 | 93.23 ± 0.07 |
| 4.0 | 94.35 ± 0.27 | 45.77 ± 1.03 | 95.65 ± 0.13 | 94.91 ± 0.07 |
| 5.0 | | | 93.41 ± 0.43 | 95.41 ± 0.08 |
| 5.5 | | | | 94.56 ± 0.08 |

At the second software trigger stage (HLT2), standard two-body topological lines are selected as well as a dedicated line triggering on very displaced $N \rightarrow \mu^\pm \pi^\mp$ vertices (ExoticRHNU). On top of that, the MajoranaBLambdaMuDD line is included, which is dedicated to $B \rightarrow \mu^+ N(\mu^+ \pi^-)$ (with same-sign muons) that reconstructs the muon from the B as a long track and the $N \rightarrow \mu^+ \pi^-$ candidate as downstream tracks. This is the only trigger that allows us to get HNLs with a flight distance larger than about 70 cm, but it is prescaled by a factor 5. The $B \rightarrow \mu\mu\pi$ candidate is required to trigger these HLT2 lines. A study was conducted on MC samples of several HNL masses to choose the most efficient HLT2 lines, emphasising on the displaced

candidates. Results of this study is shown in Figure 4.8, where the efficiencies of all tested lines are computed with the prescales taken into account. It shows only 10 most efficient lines out of all available during Run 2 data-taking and tested by us. Lower efficiency for 2 GeV could be explained by much lower p_T of the HNL daughter particles that fire the HLT2 lines. HLT2 efficiencies are summarised later, in Appendix A.1.

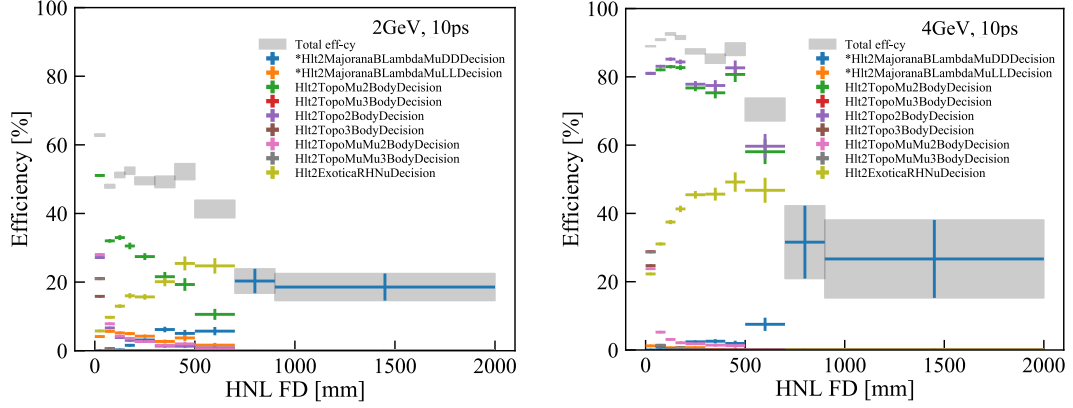


Figure 4.8 – Efficiency of HLT2 lines as a function of the HNL flight distance (FD) evaluated with MC samples for m_N of (left) 2 GeV and (right) 4 GeV. Lines are not sorted by their efficiency in the legend.

4.4.4 Offline selection

The $B \rightarrow (X)\mu^+ N(\mu^\pm \pi^\mp)$ candidates are selected offline using the stripping lines called B2-Lambda0MuBu2LambdaSSMu for the SS muon case and B2Lambda0MuBu2LambdaOSMu for the OS muon case. At first, an HNL object is formed from μ and π candidates, where two separate particle selections used: for long and downstream tracks. Then, a long μ candidate track and the HNL object are used to form a B vertex. The stripping versions used are 28r2, 29r2p1 and 34r0p1 for 2016, 2017 and 2018, respectively. The offline selection criteria applied in the stripping are summarised in Table 4.6 and discussed in detail previously.

Stripped data are further selected by the topological and PID requirements (Preselection) detailed in Table 4.7. These requirements are applied to the N candidate and N daughter particles in order to remove those inconsistent with $N \rightarrow \mu\pi$ decays. If a fake track is reconstructed from combinations of random hits, spillover from the previous bunch crossing or hits belonging to other objects, it is called a ghost track. LHCb employs a neural-network based method to identify ghost tracks which gives a probability-like score to the track to be a fake one. A constraint of $\text{ProbNN}_{\text{gh}} < 0.35$ is applied to ensure that ghost tracks do not pass the signal selection. Pion tracks that fulfill isMuon condition, which requires matching hits in several consecutive Muon stations, are also removed. When applying isMuon requirement, inMuon has to be fulfilled as well to ensure that the track is in acceptance of Muon stations.

To reduce background from partially reconstructed decays and random track combinations,

Table 4.6 – Selection criteria applied to signal candidates during the LHCb stripping phase. Requirements for the SS and OS candidates are identical except the $(N \text{ Vertex} - B \text{ Vertex})_z$, which is indicated by (*) for the OS line.

| | |
|---|----------------------------------|
| <i>B</i> | |
| m | $\in \{1500, 6500\} \text{ MeV}$ |
| Vertex χ^2 / dof | < 4 |
| $(N \text{ Vertex} - B \text{ Vertex})_z$ | $> -1(5)^* \text{ mm}$ |
| DIRA_{PV} | > 0.99 |
| <i>N</i> | |
| m | $> 1500 \text{ MeV}$ |
| p_T | $> 700 \text{ MeV}$ |
| χ^2 -separation from PV | > 100 |
| Vertex χ^2 / dof | < 10 |
| π | |
| p | $> 2000 \text{ MeV}$ |
| p_T | $> 250 \text{ MeV}$ |
| Track χ^2 / dof | < 4 |
| Minimum IP- χ^2 w.r.t. PV | > 10 |
| μ | |
| p | $> 3000 \text{ MeV}$ |
| p_T | $> 250 \text{ MeV}$ |
| Track χ^2 / dof | < 4 |
| Minimum IP- χ^2 w.r.t. PV | > 12 |
| $\text{ProbNN}_{\text{gh}}$ | < 0.5 |
| PID_μ | > 0.0 |
| $\text{PID}_\mu - \text{PID}_K$ | > 0.0 |
| $\text{PID}_\mu - \text{PID}_p$ | > 0.0 |

the kinematic variable DIRA is used, which is a cosine of the angle between the direction vector from N origin vertex to its end-vertex and the momentum vector of N . Since N could be of a short lifetime with no flight distance, an additional DIRA_{PV} with respect to the PV is used. Although at this stage the requirement of $\text{DIRA} > 0.996$ is rather loose (see Figure 4.9), it removes $\approx 20\%$ of combinatorial background events while being more than 98% efficient on signal. Validity of this approach is also confirmed by the truth-matching study summarised in Figure 4.7. This variable is also used later in a multivariate analysis technique to allow for a more powerful background rejection.

The “fiducial volume” (FV) selections on p , p_T and η of at least one muon, all signal tracks, and of the HNL candidate, detailed in Table 4.8 are applied to cut out the phase-space corners

4.4. Reconstruction and selection of the signal candidates

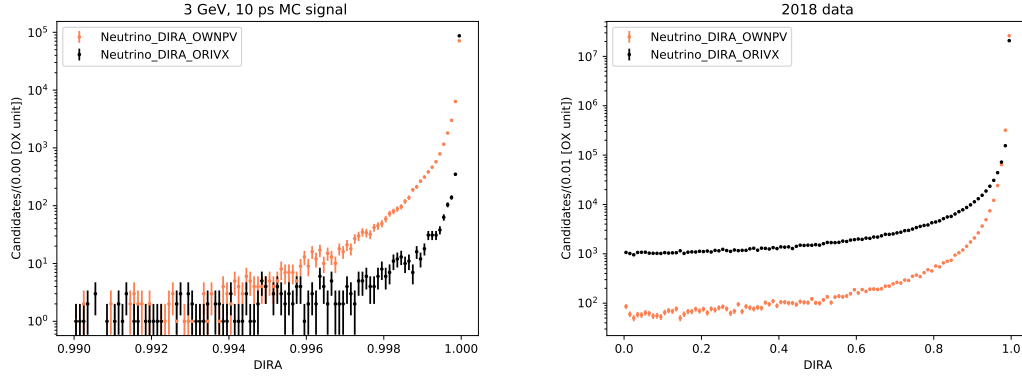


Figure 4.9 – Distribution of DIRA_{PV} and $\text{DIRA}_{\text{OrVtx}}$ of MC signal (left) and reconstructed data (right) events.

Table 4.7 – Preselection criteria applied to signal candidates.

| N | |
|------------------------------|-----------|
| DIRA_{PV} | > 0.996 |
| $\text{DIRA}_{\text{OrVtx}}$ | > 0.996 |
| π | |
| $\text{ProbNN}_{\text{gh}}$ | < 0.35 |
| isMuon | false |
| inMuon | true |
| μ | |
| $\text{ProbNN}_{\text{gh}}$ | < 0.35 |

where the detector acceptance is low and therefore for which it is harder to estimate reliably the signal efficiency. The FV requirements include a selection on one of the muons to have $p_T > 1.1$ GeV and $p > 6$ GeV which matches the HLT1 trigger requirement (see Table 4.4). The efficiency of the FV on top of the other requirements detailed above is larger than 90% for an HNL mass of 2 GeV (which is the most sensitive search region).

Table 4.8 – Overview of the applied fiducial volume cuts.

| Applied to | η | p_T [GeV] | p [GeV] |
|-----------------------------|----------|---------------|-------------|
| Single μ | (2, 4.5) | > 1.1 | > 6 |
| At least a μ or a π | (2, 4.5) | > 0.3 | > 3 |
| HNL candidate | (2, 4.5) | > 1.0 | > 15 |

Table 4.9 shows the efficiency of different selection steps discussed above for several simulated points in mass and lifetime of HNL. The efficiency chain defines the fraction of signal candidate decays that passes every level of the selection. At each step, the efficiency is computed

relatively to the previous one.

The acceptance efficiency, ϵ_{acc} , is defined as the ratio of the number of events that pass the LHCb spatial acceptance selection to the total number of generated events. Efficiency of reconstruction and stripping algorithms outlined in Section 4.4.1, $\epsilon_{\text{reco}} \times \epsilon_{\text{strip}}$, is taking into account the physical creation of hits in the subdetectors, performance of the tracks reconstruction and decay combination, and filtering by the stripping software. As expected, this efficiency drops for the higher lifetimes as a larger fraction of HNLs flies out of the detector acceptance. For a fixed lifetime, this efficiency increases with mass up to 3 GeV as the $\mu\pi$ daughters of HNL get a larger phase-space volume and then decreases after, as the muon coming from B_q vertex becomes too soft.

Table 4.9 – Summary of the acceptance (ϵ_{acc}), a product of reconstruction and stripping ($\epsilon_{\text{reco}} \times \epsilon_{\text{strip}}$) and preselection (ϵ_{presel}) efficiencies evaluated using the signal MC.

| m_N , GeV | τ_N , ps | ϵ_{acc} , % | $\epsilon_{\text{reco}} \times \epsilon_{\text{strip}}$, % | ϵ_{presel} , % |
|-------------|---------------|-----------------------------|---|--------------------------------|
| 1.6 | 100 | 14.98 ± 0.34 | 7.87 ± 0.12 | 89.57 ± 0.47 |
| 1.6 | 1000 | 14.48 ± 0.33 | 1.23 ± 0.05 | 88.91 ± 1.22 |
| 2.0 | 100 | 14.65 ± 0.33 | 8.98 ± 0.12 | 89.44 ± 0.45 |
| 2.0 | 1000 | 14.54 ± 0.32 | 1.51 ± 0.05 | 89.03 ± 1.1 |
| 3.0 | 100 | 13.24 ± 0.3 | 11.29 ± 0.2 | 86.94 ± 0.63 |
| 3.0 | 1000 | 13.69 ± 0.31 | 1.96 ± 0.09 | 84.0 ± 1.64 |
| 4.0 | 100 | 13.17 ± 0.3 | 12.61 ± 0.24 | 85.65 ± 0.72 |
| 4.0 | 1000 | 12.34 ± 0.28 | 2.09 ± 0.1 | 75.25 ± 2.14 |
| 5.0 | 100 | 13.36 ± 0.3 | 11.12 ± 0.24 | 85.12 ± 0.8 |
| 5.0 | 1000 | 13.22 ± 0.3 | 1.5 ± 0.09 | 85.71 ± 2.15 |
| 5.5 | 100 | 12.94 ± 0.3 | 8.65 ± 0.22 | 85.67 ± 0.92 |
| 5.5 | 1000 | 13.67 ± 0.32 | 1.26 ± 0.09 | 79.9 ± 2.77 |

This selection chain reduces not only combinatorial background but also eliminates backgrounds coming from the photon conversions to dimuons in the material of VELO, which could pass the signal criteria if a pion in $\mu\pi$ vertex is misreconstructed as a muon. Figure 4.10-4.11 show a radial and longitudinal distributions of the HNL vertices in reconstructed data, where projections of the VELO subdetector material can be seen before the selections are applied.

4.4. Reconstruction and selection of the signal candidates

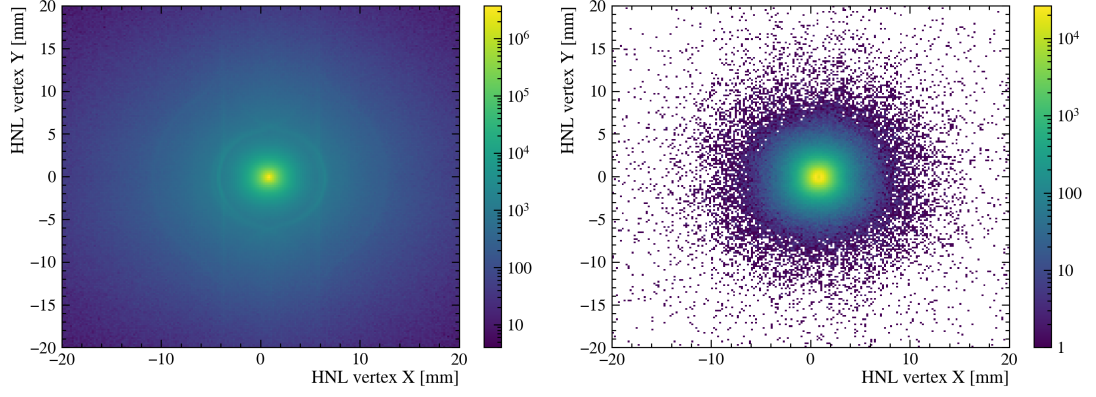


Figure 4.10 – 2D distribution of HNL vertices for the SS sample in XY coordinates. Left, dataset before the selection, right is after.

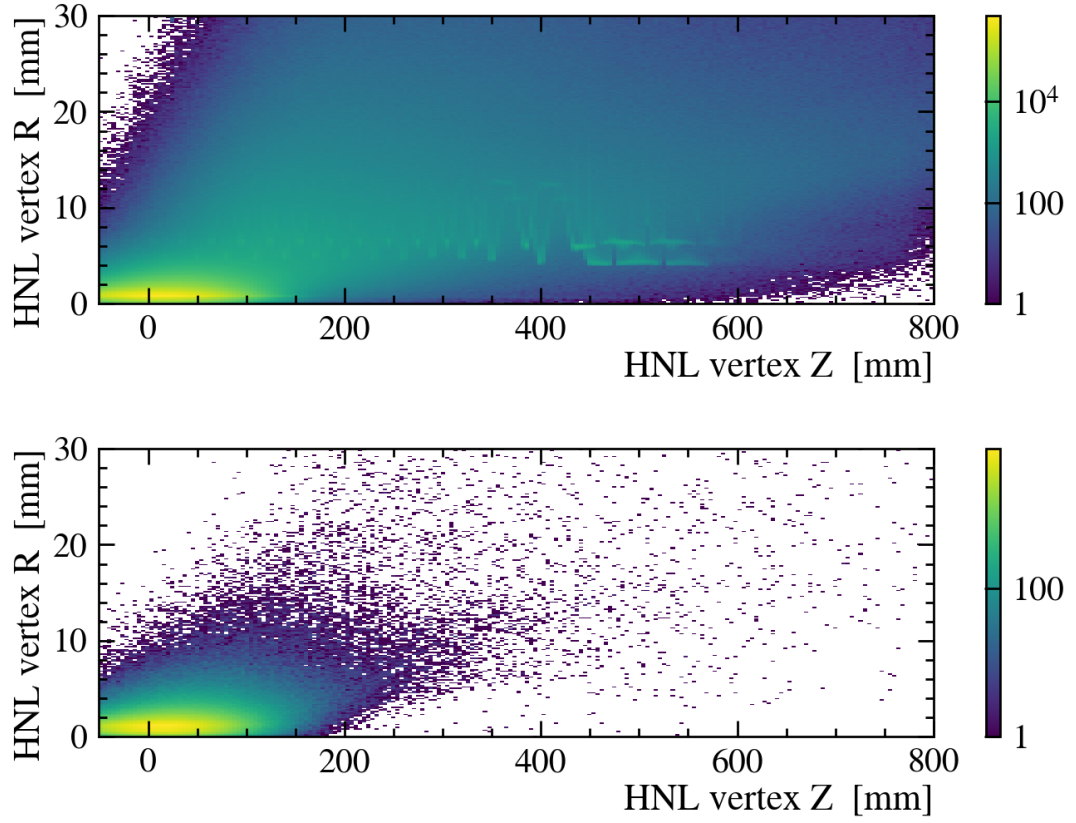


Figure 4.11 – 2D distribution of HNL vertices for the SS sample in RZ coordinates, where $R = \sqrt{X^2 + Y^2}$. Top, dataset before the selection, bottom is after.

4.4.5 Multivariate analysis selection

The combinatorial background is dominant in this analysis in the whole $\mu\pi$ mass range except the charm region, where peaking backgrounds are present as well, as discussed in Section 4.6. Combinatorial backgrounds are composed of random combinations of tracks that form a vertex, pass a signal and PID selection. These events could be filtered out by applying a multidimensional selection criteria on discrimination variables, such as those shown in Figure 4.13. Therefore, a multivariate analysis technique (*MVA*), which exploits correlation between the discriminating variables, is used to suppress the combinatorial background in this search. A classifier based on a neural network (NN) [83] of fully connected layers is developed using the *pytorch* library [84]. Usage of the NN is motivated by the possibility of using a single network over the whole range of the masses in our search, contrary to approaches that require the training of a set of isolated networks [85].

Datasets

The classifier is trained using as a signal-proxy an MC sample that includes all simulated HNL masses and lifetimes mentioned in Table 4.2. The background sample is the upper $\mu\mu\pi$ mass sideband of reconstructed data. For fully reconstructed B^+ and B_c^+ leptonic decays, the $m(\mu\mu\pi)$ sideband is taken above the $m_b + 3\sigma_m$, where m_b is the B^+ or B_c^+ mass, and σ_m is mass resolution. For partially reconstructed $B \rightarrow \mu NX$ semileptonic decays, the sideband is taken as $m(\mu\mu\pi) > m_{B^+} - m_D$ where there cannot be $B \rightarrow \mu ND$ contributions. In this sideband, residual contributions from $B \rightarrow \mu NX$ with $X = \pi, \rho$ are expected to be negligible given the existing limits. The sidebands are sketched in Figure 4.12, where the X_b candidate has its mass in a corresponding range for a given category. To increase training statistics, the sideband regions of B^+ and B_c^+ categories were merged into a single background dataset used by both categories, see a red region in Figure 4.12. To test the classifier performance, a 15% portion of the whole dataset is reserved. A separate classifier is used for each search category.

In order to enhance the discrimination power over the whole mass range, especially in the regions between simulated mass points, a new method is applied, which uses a classifier parameterised by a physics parameter, which is then used as an input feature [86]. The true HNL mass, m_N^{TRUE} , is used to parameterise the classifier, to allow it to smoothly interpolate between simulated points of the search and to replace the sets of classifiers trained at individual values. For the signal proxy, the parameterised mass feature, M_N^{sig} , corresponds to the m_N^{TRUE} distribution, while the background proxy has its m_N^{bkg} values randomly sampled from the m_N^{TRUE} . In this way, the M_N feature is uncorrelated with the background class and does not have any discrimination power in the problem. As for the HNL lifetime, τ_N parameter, it is not treated separately as the m_N since the classifier is trained using samples covering the wide range of decay time, where $\tau_N = 100, 1000$ ps and 10 ps for the leptonic categories, allowing to perform well in that range. In order to mitigate an imbalance in the number of signal and background events, $\omega_{\text{Bkg/Sig}} = N_{\text{Bkg}}/N_{\text{Sig}}$ weights are used during training, which are equal to

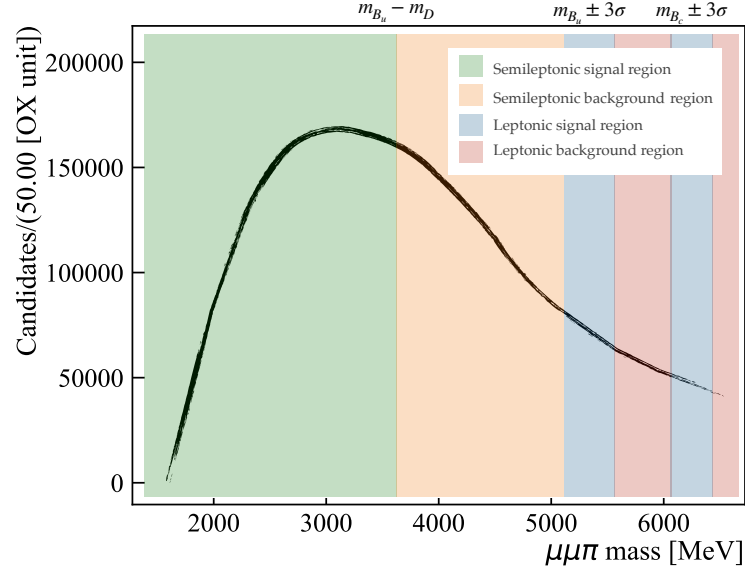


Figure 4.12 – The schematics show the signal and background regions selected based on the invariant mass of $\mu\mu\pi$. The black curve represents the expected background distribution in the data, projected from a sample with limited statistics and no selection applied.

the datasets sizes fraction.

Training features

The following list of input variables was used, which have a high discrimination power and low correlation (see Figure 4.13 and Figure 4.14):

- $\ln(FD_{\text{OWNPV}}(X_b))$ - flight distance of the X_b candidate
- $\ln(p_T(\mu_{\text{prim}}))$ - transverse momentum of the primary muon
- $\ln(\chi^2_{\text{IP_OWNPV}}(\mu_{\text{sec}}))$ - impact parameter (IP) χ^2 of the secondary muon
- $\ln(p_T(\mu_{\text{sec}}))$ - transverse momentum of the secondary muon
- $\ln(\chi^2_{\text{IP_OWNPV}}(N))$ - IP χ^2 of HNL
- $\ln(\chi^2_{\text{IP_OWNPV}}(\pi))$ - IP χ^2 of pion
- $\ln(p_T(\pi))$ - transverse momentum of pion
- $\log(1 - \text{DIRA}_{\text{ORIVX}}(N))$ - cosine of the angle between HNL momenta and the direction vector, that connects X_b and HNL candidates end-vertices (DIRA)
- $\log(\frac{\chi^2_{\text{ENDVTX}}(N)}{N \text{DOF}_{\text{ENDVTX}}(N)})$ - HNL end-vertex χ^2 divided by its number of degrees of freedom
- M_N - the parameterised mass feature
- $\log(1 - \text{DIRA}_{\text{ORIVX}}(X_b))^*$ - DIRA of the X_b candidate w.r.t the PV. *This feature is used only for the leptonic categories, where B vertex is fully reconstructed.

Figure 4.14, left, shows that the M_N feature is uncorrelated with the background class, as was mentioned previously.

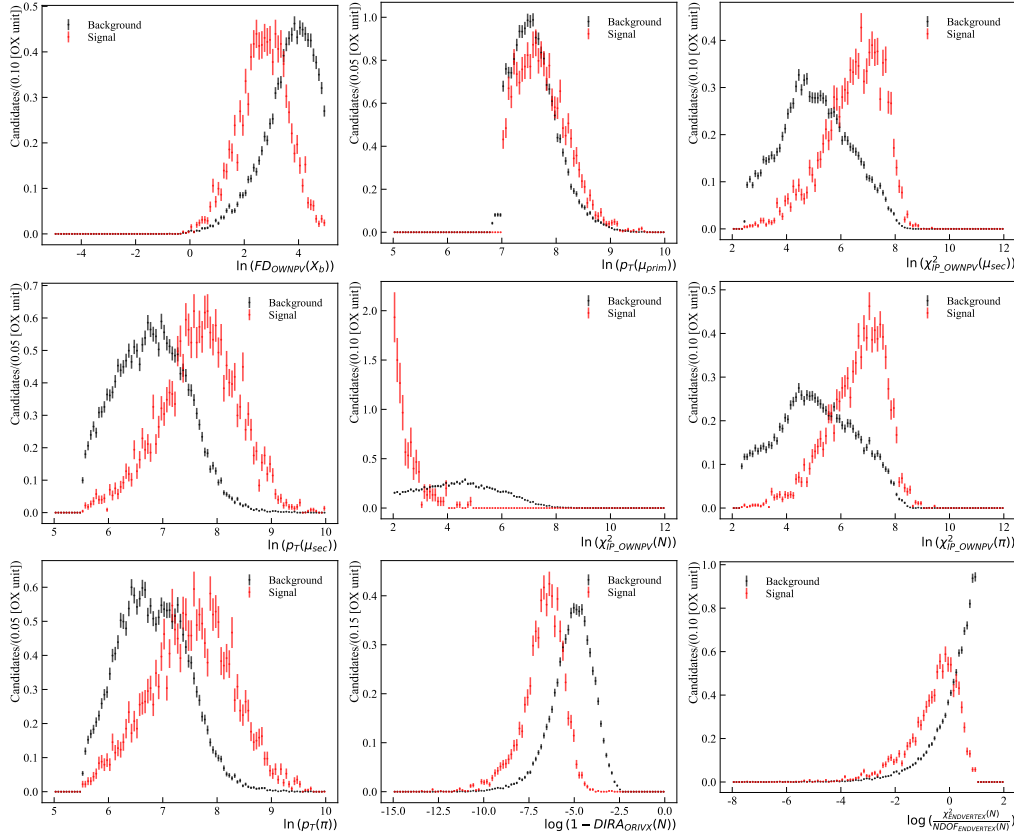


Figure 4.13 – MVA inputs variables for the Run 2 samples of background (black) and signal (red) data. The order of the plots corresponds to the list in the chapter. semileptonic, SS, downstream search category is shown.

Signal samples of the SS and OS categories do not have any difference in the features (see Figure 4.15) distributions, so data sets are concatenated into a single one and used for the MVA classifier training. This doubled the number of events for the classifier training and improved overall performance.

NN structure and hyper-parameters optimisation

The Multilayer Perceptron (MLP) is used as a base classifier. It is a neural network where the mapping between inputs and output is non-linear. Between input and output layers it has one or more hidden layers with many neurons (nodes) stacked together. Each layer is followed by an activation function which determines if the neuron will fire or not. The MLP network is a feedforward algorithm where inputs are combined with the initial weights to form a weighted sum and passed forward to the next layers through the activation function. Results of the internal representation of data by each layer is passed all the way to the output layer. The MLP algorithm *learns* in a way that can be outlined as the following procedure:

4.4. Reconstruction and selection of the signal candidates

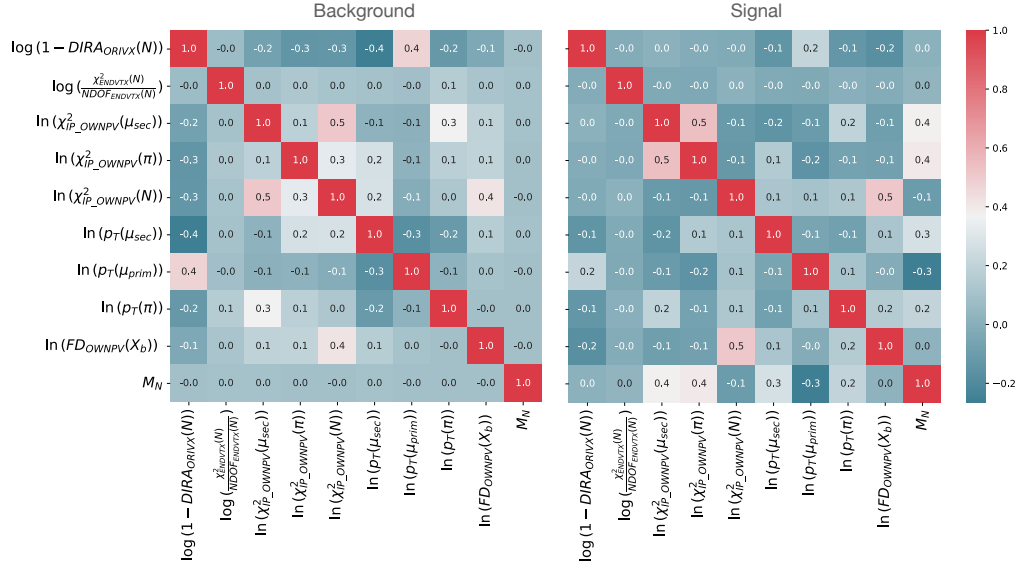


Figure 4.14 – MVA features correlation matrix for the background (left) and signal (right) samples. semileptonic, SS, long search category is used.

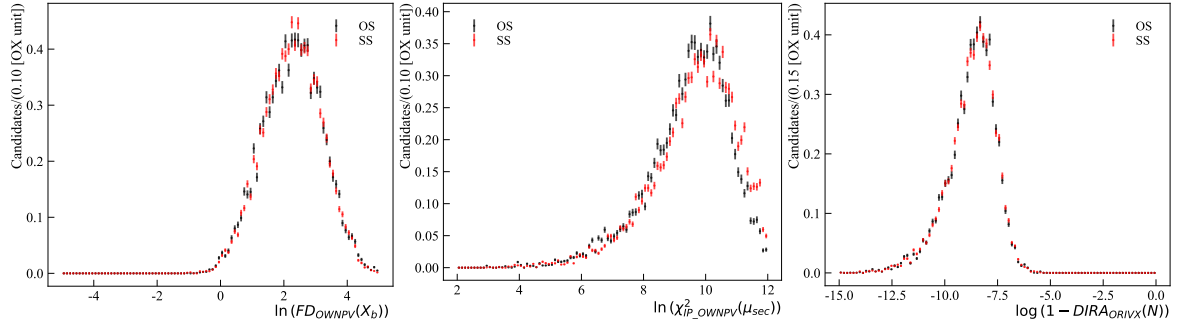


Figure 4.15 – Comparison of the several training features for the SS vs OS modes. Signal proxy of the semileptonic, SS, long search category is shown.

- Through the input layer, propagate the data forward to the output layer, i.e. perform the forward propagation.
- Based on the outputs, calculate the difference between the predicted and known outcome, i.e. errors that have to be minimized. To compare the target and predicted output values a loss function is used.
- Backpropagate these errors through all the layers using the optimisation function, compute its derivatives with respect to each weight in the network, and update all the weights.

This process is repeated multiple times (epochs) to find ideal weights. At the end of each epoch the NN performance is tested on a separate dataset which is not used during the training process. In this way it is ensured that NN is tested on the data which it was not fit to before.

Our NN is the MLP with a dropout between each fully connected linear layer that makes classifier more robust to overfitting. The dropout technique at each iteration randomly drops (not uses) P_{dropout} fraction of nodes during the forward propagation. Each layer has the rectified linear unit (ReLU) function as the activation function [87], except the last one, which uses a sigmoid in order to provide an output value in a range of [0, 1] as a probability of the binary classification. A total number of the NN layers is equal to three plus $N_{\text{add.layers}}$ with a node size of each layer of N_{node} . A combination of the sigmoid layer followed by the binary cross entropy function (BCELoss) [88] was used as a loss function, where the aforementioned $\omega_{\text{Bkg/Sig}}$ weights are applied. Finally, the Adam optimiser [89] with the learning rate value of P_{LR} is used to update the NN weights during training, where P_{LR} value is decreased by 5% after each training epoch to take into account a steep learning process at the beginning and to avoid the overtraining later.

All mentioned above hyper-parameters: $N_{\text{add.layers}}$, N_{node} , P_{dropout} and P_{LR} are optimised using the Bayesian optimisation (BO) with a Gaussian process (GP). This algorithm allows to optimise parameters with only O(50) iterations and takes into account multidimensional relations correctly [90]. A classification accuracy is used as the figure of merit, and the set of parameters at the maximum is used. Figure 4.16 shows an example of optimised hyper-parameters for the semileptonic, SS, downstream category. Also, to make adjustment of the number of training epochs easier, the early stopping algorithm is used, which terminates the learning process when the training loss is not improving or is showing indications of overtraining. In order to ensure the best performance, the classifier for each search category is optimised separately.

Optimisation of the MVA requirement threshold and performance

Output of the classifier, the prediction score of the positive class, is the value in range of [0,1], which can be interpreted as a probability of an event to belong to the signal category, with 1 being signal-like and 0 background-like, correspondingly. This distribution, which is shown in Figure 4.17, shows a great separation power and no signs of the overtraining. Then, the following transformation is performed on the MVA distribution in the signal and background samples before using it for classification

$$MVA_{\text{flat}}(x) = \frac{\int_{-\infty}^x MVA(y) dy}{\int_{-\infty}^{+\infty} MVA^{\text{sig}}(y) dy}, \quad (4.4)$$

where MVA^{sig} is used as a flattened distribution. It does not change the separation power but allows for a better control and optimisation of the MVA selection threshold value, which is shifted to 1 otherwise.

By construction, the classifier can be applied on the whole range of mass, but also, the amount of combinatorial background is changing when shifting from lower to higher mass region.

4.4. Reconstruction and selection of the signal candidates

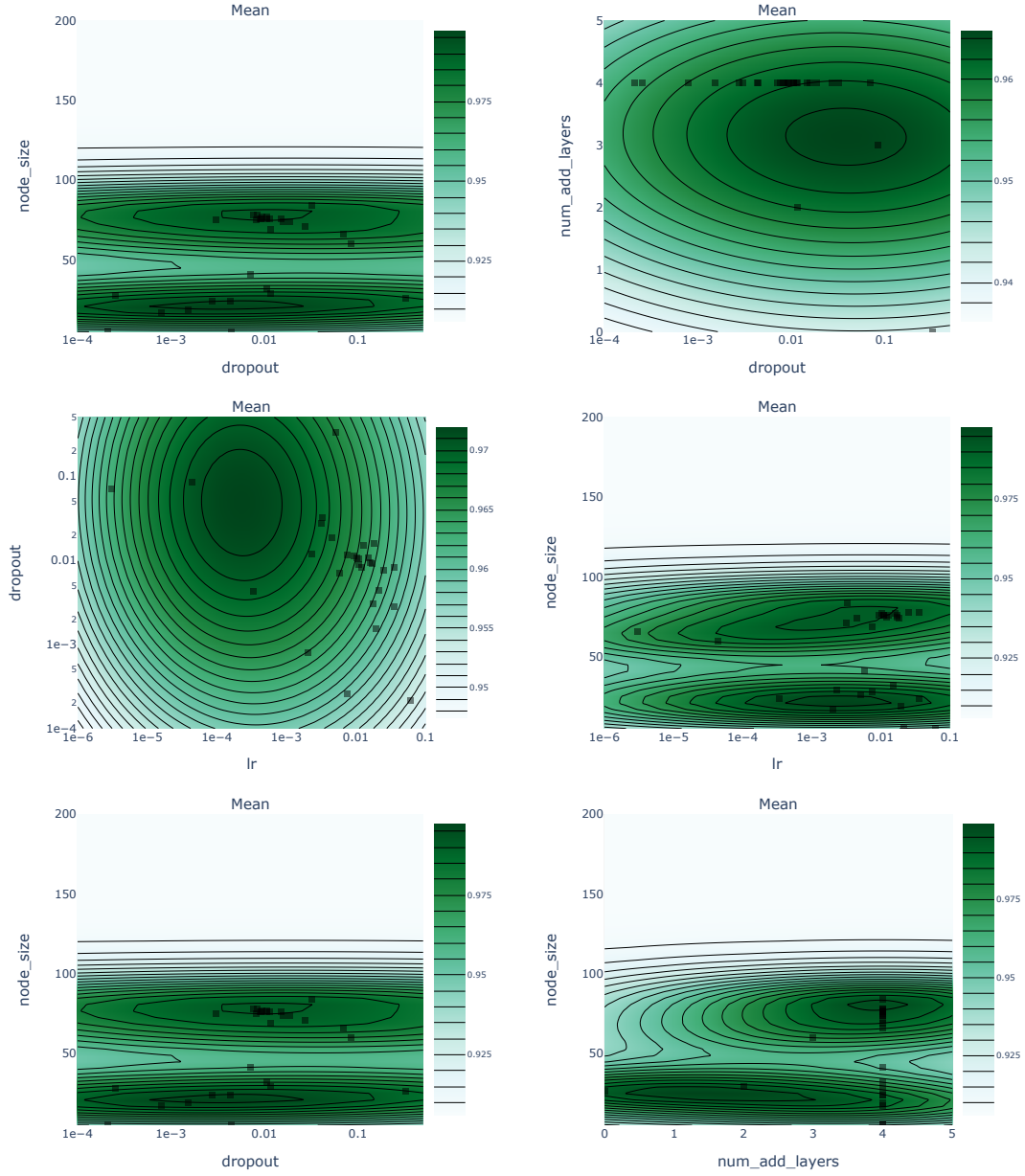


Figure 4.16 – 2D projections of the classification accuracy for all combinations of optimised hyper-parameters $N_{\text{add.layers}}$, N_{node} , P_{dropout} and P_{LR} . The black squares show points of the actual trials, which are used in the BO algorithm to makes predictions on the unobserved parameterization (contour plot). The semileptonic, SS, downstream category is shown.

This requires to have multiple selections on MVA_{flat} variable over the range of probed masses to have the best final sensitivity. Thus, this requirement is optimised for each simulated mass m_N and its value is interpolated over the whole mass region. The Punzi figure of merit [91] is

used to set a threshold on the MVA_{flat} variable

$$FOM(m_N) = \frac{S(m_N)}{\sqrt{B(m_N)} + \frac{3}{2}}, \quad (4.5)$$

where S is a signal efficiency, and B is an extrapolated background yield in the region of $m_N \pm 3\sigma_{m_N}$, that are evaluated after the requirement is applied. In order to perform a blinded optimization, the B value is taken from the upper mass sideband defined earlier, and scaled by a transfer factor $f_{\text{sig}} = N_{\text{sig.sample}}/N_{\text{bkg.sample}}$, where $N_{\text{sig.sample}}$ and $N_{\text{bkg.sample}}$ are the sizes of the signal and background data sets in the regions defined in Figure 4.12, after the preselection. This transfer factor is measured once and is used throughout the optimization process. Value of σ_{m_N} is set to 25 MeV, which corresponds to the highest value expected in this analysis. The MVA_{flat} requirement value is chosen where the Punzi FOM is at the maximum (see Figure 4.18, left), ensuring to have at least $\mathcal{O}(10)$ events left in the signal region for the final fit. Resulting efficiencies are shown in Figure 4.18 (right) for a single search category, and the full list can be found in Figure A.1 in the Appendix A.2. The lower mass regions have higher combinatorial background that requires a tighter threshold value of MVA_{flat} , which results into a lower signal efficiency at the same level of the background rejection. For the same exact reason, semileptonic categories have lower signal MVA efficiency in comparison with the leptonic ones (see Figure A.1).

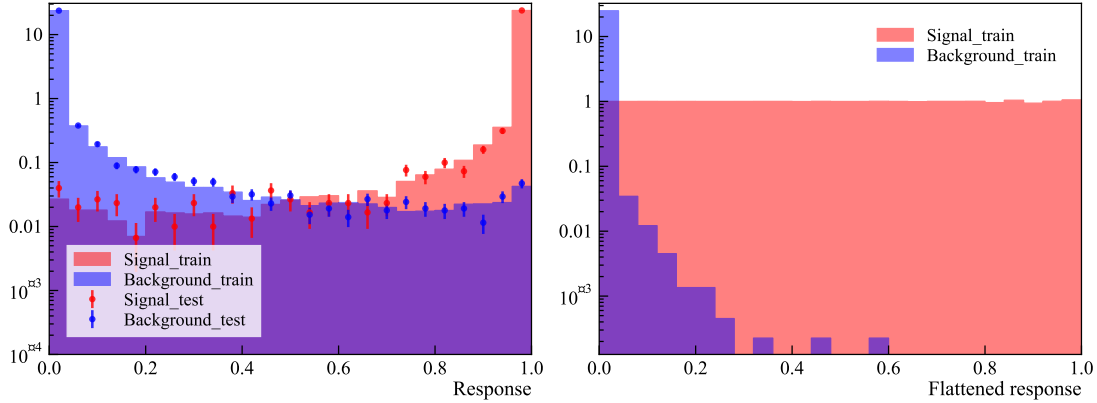


Figure 4.17 – Left, comparison of the training and test distribution of the classifier response MVA^{sig} for leptonic Bu, SS, long. Right, flattened classifier response using Equation (4.4).

4.4.6 Optimisation of the particle identification selection

The PID selection on muons is applied at the stripping stage and is summarised in Table 4.6. It lists the variables PID_i where $i = \mu, p, K$ which are defined as the combined delta-log-likelihood for the given candidate hypothesis with respect to the pion hypothesis, as discussed in details in Section 2.2.4.

4.4. Reconstruction and selection of the signal candidates

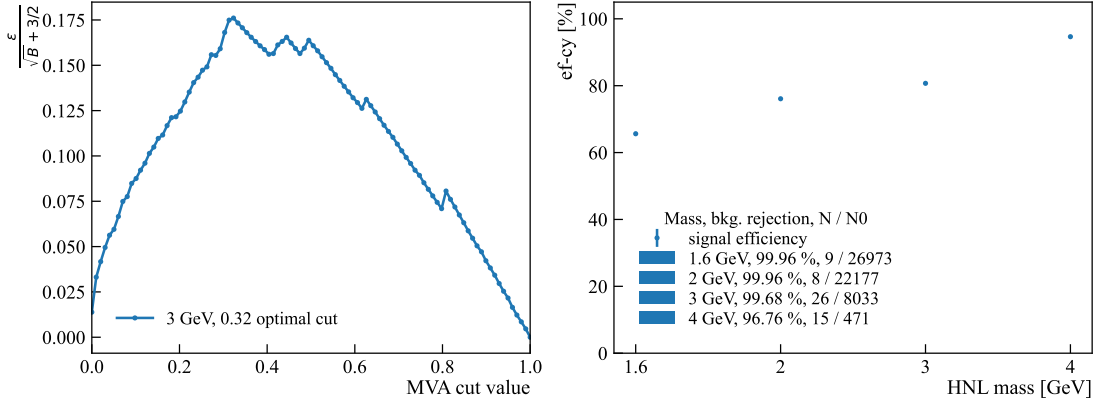


Figure 4.18 – Left, Punzi FOM evaluated on MVA_{flat} selection for 3 GeV mass point. Right, signal efficiency and background rejection as a function of m_N . Both plots are evaluated for the semileptonic, SS, long category.

For pions, a selection on $\text{ProbNN}\pi$ variable is used, which is an output of the standard LHCb NN based PID tool (see Section 2.2.4). It gives a score between 0 and 1, which is related to the probability of the candidate to be a pion track. Distributions of $\text{ProbNN}\pi$ variables for multiple search categories and simulated m_N are displayed in Figure 4.19 showing no significant difference among them. The requirement on $\text{ProbNN}\pi$ is obtained when maximizing the Punzi FOM in the same way as for the MVA_{flat} selection. It is done for several masses (see Figure 4.20 and 4.21), and the optimal value is found and fixed to be $\text{ProbNN}\pi(\pi) > 0.6$ for all categories in the search to have the efficiency of this selection above 80%. This step is done independently of the MVA selection procedure and the PID selection for pion is optimised before applying the MVA.

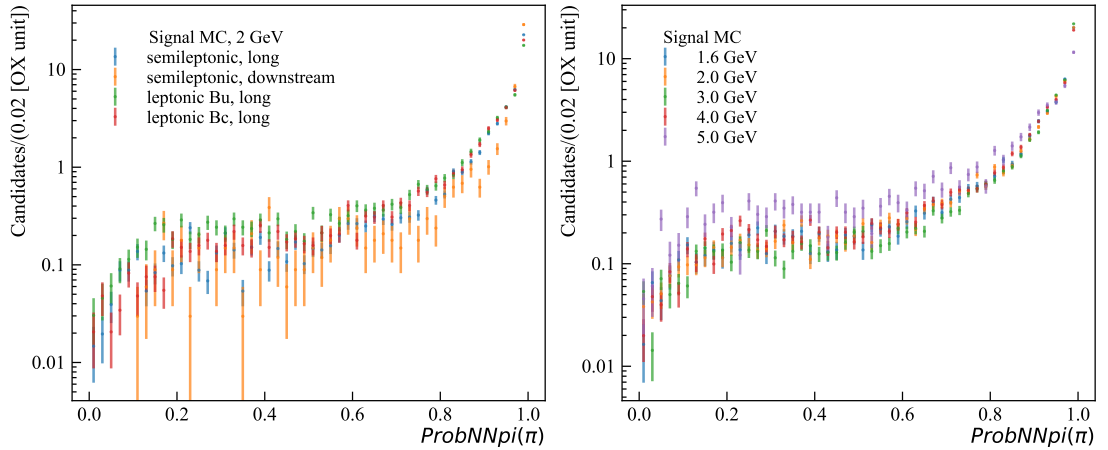


Figure 4.19 – (Left) Distribution of the pion PID output, $\text{ProbNN}\pi$, for the SS search categories. (Right) Distribution of $\text{ProbNN}\pi$ for several simulated m_N in the leptonic B_u , OS, long category.

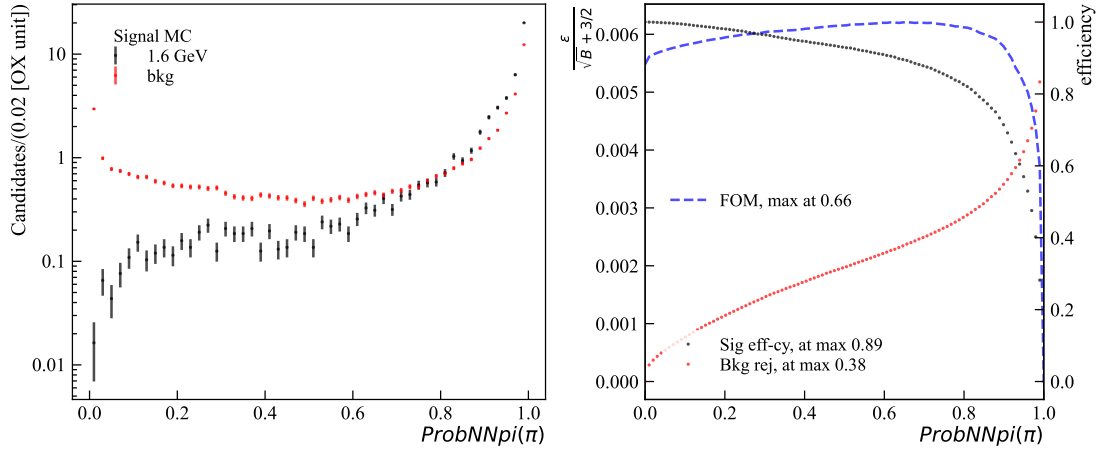


Figure 4.20 – (left) Signal *vs.* background comparison of the pion PID output. (right) Punzi FOM distribution for $m_N = 1.6$ GeV in the leptonic B_u , 0S, long category.

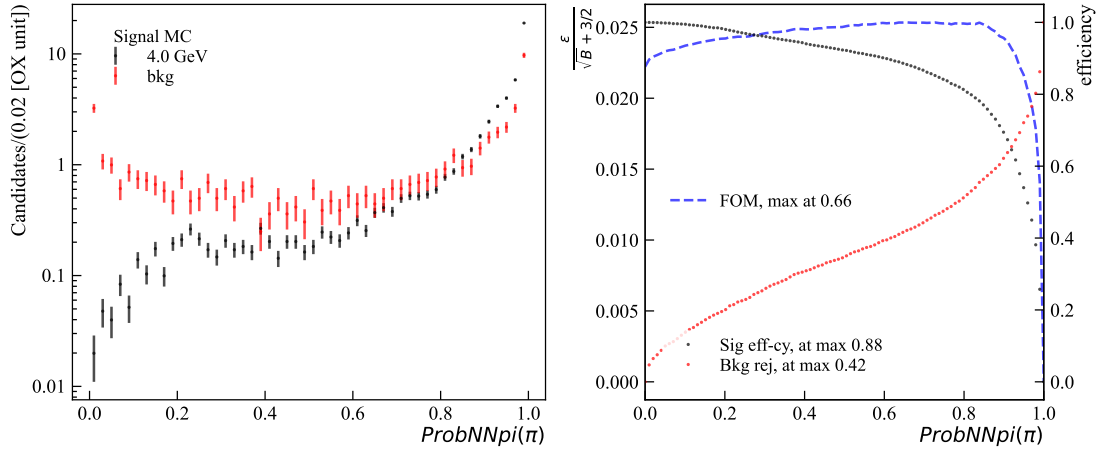


Figure 4.21 – (left) Signal *vs.* background comparison of the pion PID output. (right) Punzi FOM distribution for $m_N = 4$ GeV in the leptonic B_u , 0S, long category.

4.5 Signal efficiency

4.5.1 Fiducial volume efficiency

The FV is defined only in terms of the momenta \vec{p} of the reconstructed part of the decay $\mu\mu\pi$ and therefore depends only on the HNL mass (and not on its lifetime). The FV efficiency is calculated for the three decay categories ($B^+ \rightarrow \mu^+ N$, $B_c^+ \rightarrow \mu^+ N$, $B \rightarrow \mu^+ NX$).

The absolute FV efficiency depends on the accuracy of the simulated B meson production spectrum. For this analysis, the $pp \rightarrow B^\pm X$ production cross section measured by LHCb [73] within the FV $2 < y(B^\pm) < 4.5$ and $0 < p_T(B^\pm) < 40$ GeV is used. Therefore, the ratio between the efficiency of the FV of our measurement and that of the cross section measurement has to be estimated. This ratio is expected to be less affected by the theoretical uncertainties related to the prediction of the B meson production spectrum than the absolute FV efficiency.

Note that one cannot impose directly the FV requirements of the cross section measurement on the signal candidates if the B meson is not fully reconstructed. However, the FV of the cross section measurement includes almost completely the FV of this search. Namely, the FV of the cross section measurement applied on top of our FV is more than 99.5% efficient. The B meson rapidity y and transverse momentum p_T distributions of signal decays within the FV are shown in Figure 4.22.

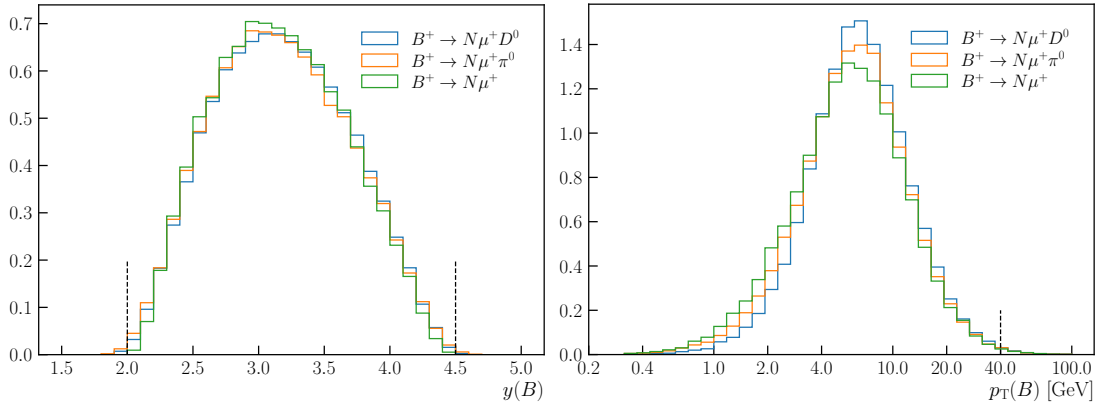


Figure 4.22 – B meson (left) rapidity y and (right) transverse momentum p_T for signal events within the FV of the analysis. Events are generated with RapidSim. The requirements of the FV of the $pp \rightarrow B^\pm X$ cross section measurement by LHCb [73] are shown with vertical dashed black lines.

The produced LHCb MC samples are required to have particles in the LHCb geometric acceptance at the generator level, *i.e.* InLHCbAcceptance requirement requires that each “stable charged particle” is in a loose region around the LHCb acceptance, θ of 10-400 mrad. Mis-modelling in the branching ratios of the different decays contributing to the inclusive channel mentioned earlier makes it impossible to get these generator-level efficiencies from MC production logs. Therefore, a simulation framework called *RapidSim* [92] is used to calculate

the FV efficiency by generating a list of samples following the branching ratio predictions shown in Figure 4.3. Leveraging the speed of RapidSim event generation, the FV efficiencies are obtained with statistical uncertainty below 0.5%, which is considered negligible, and in fine steps of m_N . The resulting FV efficiency divided by the cross section measurement FV efficiency is shown in the left panel of Figure 4.23. The method is cross-checked by comparing the efficiencies obtained from RapidSim and from the LHCb MC samples (in the few m_N points generated) for a few exclusive channels. These results are shown in the right panel of Figure 4.23.

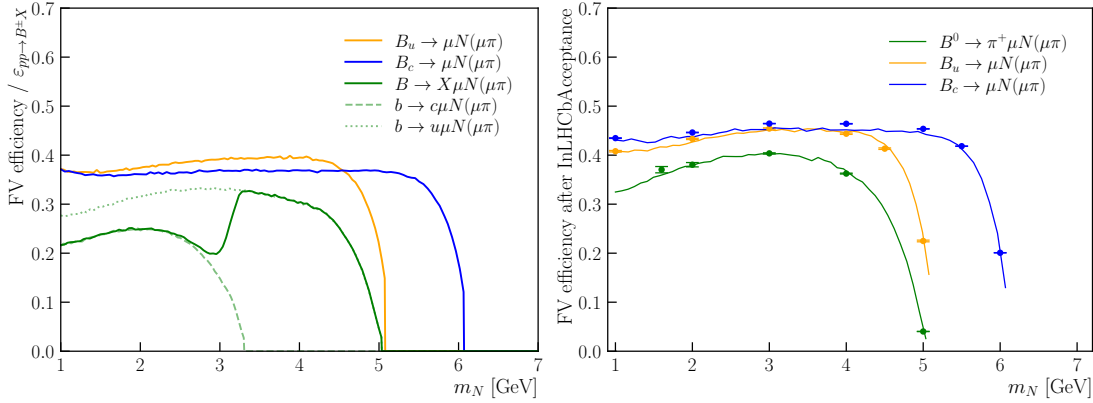


Figure 4.23 – (left) Fiducial volume efficiency divided by $\epsilon(\text{FV}_{pp \rightarrow B^\pm})$ with respect to the mass of the heavy neutral lepton. The semileptonic green curve is split into the contributions of X_{Prim} containing a c quark or a u quark. (right) Comparison of the efficiencies obtained from RapidSim (solid line) and from the LHCb MC samples (simulated m_N points).

Due to the (transverse) momentum requirements of the FV, the efficiency drops as m_N reaches the kinematic limit. Decay channels involving the $b \rightarrow c\mu N$ quark-level transition have lower FV efficiency than those involving $b \rightarrow u\mu N$ as the unreconstructed charmed mesons from $b \rightarrow c\mu N$ are more massive and leave less energy to the reconstructed μN final state.

4.5.2 Pruning of reconstruction categories

As detailed in Section 4.4.2, the analysis has $3 \times 3 \times 2 = 18$ reconstruction categories. Before going further, the sensitivity of these categories is estimated and the least sensitive ones are dropped. The region of the U_μ^2 parameter space excluded by each category is estimated using simplified efficiency maps (not including the MVA efficiency and the data/simulation corrections) and assuming zero background (this hypothesis is particularly misplaced for the prompt category). Results of this sensitivity study are shown in Figure 4.24 for the nine SS categories.

The prompt categories are found to be sensitive only at the high HNL mass, m_N , in a region that is already excluded by other experiments. Given the largest amount of background in these prompt categories, they were dropped in favor of concentrating on the more promising

displaced categories. For the case of the downstream category, since the trigger line dedicated to downstream HNLs MajoranaBLambdaMuDD is only targeting SS events and the HLT1 trigger TrackMuon requires an energetic long muon, only the SS semileptonic downstream category was kept. The SS categories that are discarded are barred in the legend of Figure 4.24. For OS, also the semileptonic downstream category is dropped.

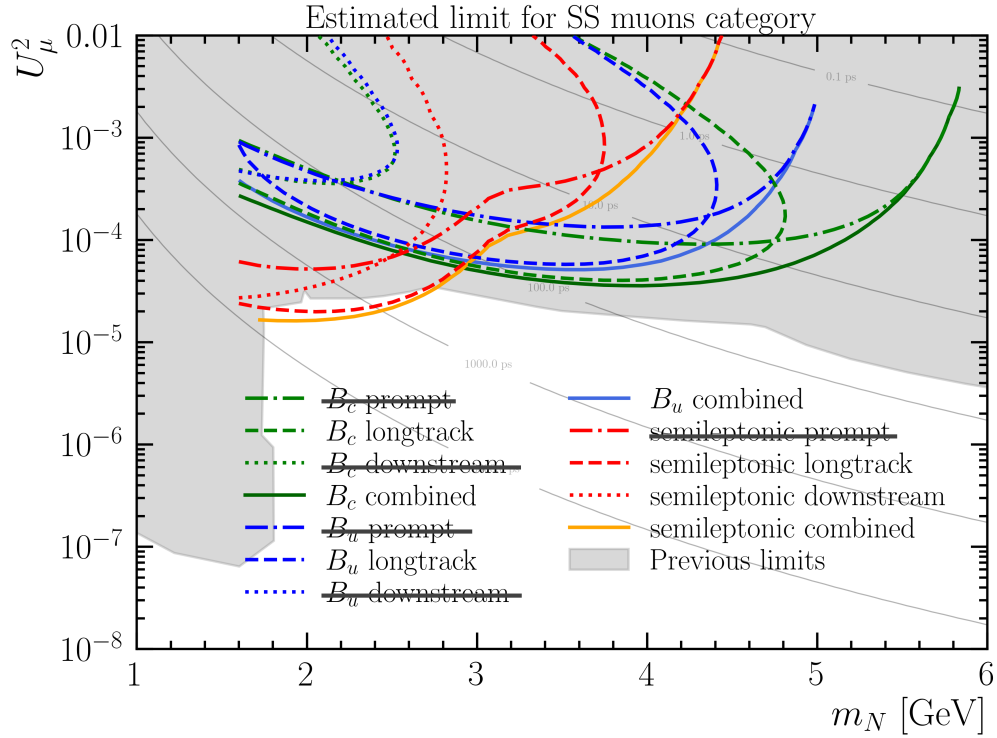


Figure 4.24 – Estimated exclusion regions in the U_μ^2 vs m_N plane for the various reconstruction categories of the SS sample. The categories that are dropped are barred in the legend. The OS categories are exactly the same, excluding the downstream one.

4.5.3 Selection efficiency

The signal selection efficiency ε_{sel} includes all the stages of all online and offline requirements for signal decays produced within the FV of the analysis (FV_{HNL}) discussed before. This efficiency is obtained from MC as a function of the HNL mass and lifetime, and separately for all the search categories considered in this analysis.

Comparing to all the other stages, FV efficiency, ε_{FV} , is computed in a specific way as the FV_{HNL} requirements are actually applied on true particle momenta at the generator level (denominator) and on reconstructed track momenta on the reconstructed events (numerator). However, the fraction of events entering only the numerator or only the denominator is negligible, which is possible due to the excellent LHCb momentum resolution for muons and

pions.

The online and offline selection applies all the requirements detailed in Sec. 4.4, including the requirements on the MVA response. The datasets in the numerator and denominator of ϵ_{sel} are corrected using the branching-ratio and the weights computed in Sec. 4.3.3. The numerator is also corrected for the MC-data differences in the trigger, GEC and PID response as explained in Section 4.5.4. To get the reconstructed efficiency, ϵ_{sel} , for any needed lifetime, τ_N , a lifetime-reweighting of the MC samples is applied. It allows to change the decay time constant of an MC sample to a needed one but has its own limitations, as discussed in Section 4.5.3. In order to measure the signal efficiency at any HNL mass, creation the m_N efficiency grid would require a large amount of computationally expensive MC samples. Therefore, to obtain ϵ_{sel} for any m_N it is interpolated between the few simulated mass points. At the end, efficiency maps that depend on the HNL mass and lifetime are obtained.

The statistical uncertainty in the efficiency is obtained by summing the square of the weights. Correlations of the uncertainties stemming from the numerator and the denominator are small and are therefore neglected.

Lifetime reweighting

MC samples are generated with $\tau_N = 100, 1000$ ps, covering effectively the decay-time acceptance for long and downstream tracks. Efficiency for other lifetime values are obtained by reweighting the true decay time distribution of reconstructed events. This technique allows to transform the MC sample which was generated with the lifetime constant of τ_{gen} to a sample with a lifetime constant τ_{target} . The per event weight w_i to scale from a generated lifetime τ_{gen} to a lifetime τ_{target} is computed using the following formula

$$w_i = \frac{\tau_{\text{gen}}}{\tau_{\text{target}}} \frac{e^{-t_i/\tau_{\text{target}}}}{e^{-t_i/\tau_{\text{gen}}}}, \quad (4.6)$$

where t_i is the true HNL decay time (proper time) and the factor τ_1/τ_2 ensures that the sum of the average weight for a decay-time unbiased distribution is 1. Weighting samples from the smaller to larger lifetimes can bias the efficiency value, as the low-lifetime sample does not cover lifetime distribution completely, which is illustrated in Figure 4.25. This effect is avoided by taking a weighted average of the MC samples that enhances the effect of the sample with τ_{gen} closest to τ_{target} .

Behavior of this lifetime reweighting procedure is cross-checked by comparing the resulting efficiency with the one obtained from the MC simulation without any lifetime reweighting. As shown in Figure 4.26, this procedure does not introduce any bias.

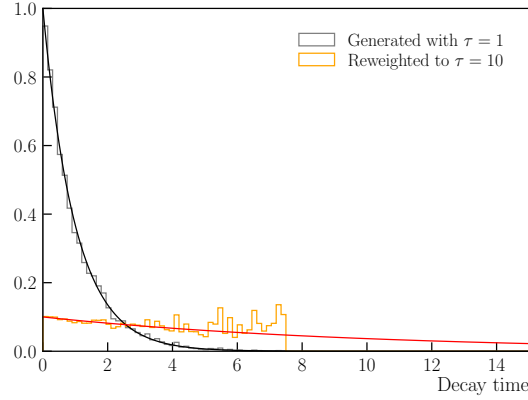


Figure 4.25 – An extreme example of lifetime reweighting from 1ps to 10ps to illustrate possible biases when reweighting from small to large lifetimes.

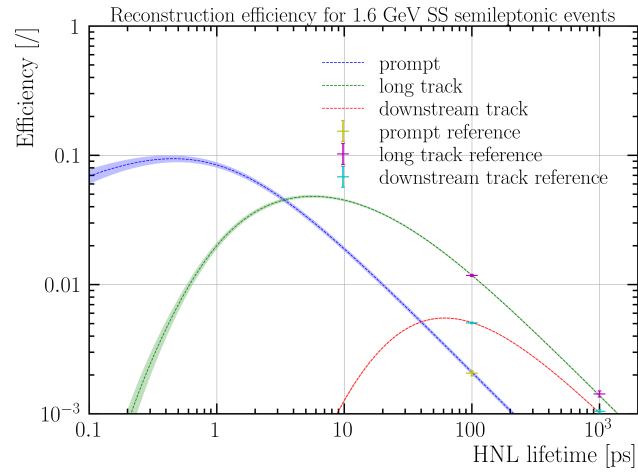


Figure 4.26 – Cross-check of the lifetime reweighting procedure. Efficiencies obtained with all MC samples using reweighting are compared to those obtained with the simulation generated with lifetimes of 100 and 1000 ps. The falling exponential shape of the efficiencies at high lifetimes is expected (the decay time distribution within the detector acceptance is approximately flat for long enough lifetime). This crosscheck does not include cuts on nSPD, PID and the MVA.

Mass interpolation

For the interpolation of the efficiency between the simulated HNL mass values, a *cubic spline* is used. The corresponding fitting algorithm was developed that uses four knots and low-degree polynomials between them as a fit function. Spline algorithm was chosen because single high-degree polynomials tend to oscillate between the knot points and tend to overestimate efficiency values. The spline fitting takes the initial mass points reweighted to a given lifetime. No extrapolation outside the range of simulated mass points is done. To propagate the efficiency uncertainty in the simulated mass points to the interpolated function, a dedicated

toys algorithm is used. The efficiency values for the spline knots are drawn from the Gaussian distribution $G(\varepsilon(m_N, \tau_N), \sigma_{\varepsilon(m_N, \tau_N)})$ with mean equal to the measured reconstruction efficiency $\varepsilon(m_N, \tau_N)$ and its uncertainty as a sigma, $\sigma_{\varepsilon(m_N, \tau_N)}$. This toy experiment is repeated 5000 times, and mean of this distribution is taken as the interpolated efficiency value. The standard deviation of the resulting distribution is assigned as the interpolated uncertainty. At this step, only statistical uncertainties and systematical uncertainty in the GEC (see Sec. 4.5.4) are taken into account.

Figure 4.27 shows the interpolated efficiencies for the long categories for $\tau_N = 99$ ps. The maximum of these efficiencies is between 3 and 4 GeV of m_N where the HNL is both massive enough to give large p_T for the secondary muon and light enough to leave some phase space for the primary muon. Also, the efficiencies are significantly larger for $B^+ \rightarrow \mu^+ N$ than for $B_c^+ \rightarrow \mu^+ N$ because the B^+ lifetime ($\tau(B^+) \simeq 1.64$ ps) is significantly larger than the B_c^+ lifetime ($\tau(B_c^+) \simeq 0.51$ ps), which lets them fly further away of a high-occupancy region within the detector acceptance, and therefore allows the primary muon from the B^+ to pass IP requirements more efficiently.

Efficiencies for the downstream category of the semileptonic SS sample are shown in Figure 4.28. As was explained in the trigger Section 4.4.3, for downstream category, the HLT1 trigger efficiency relies on the primary muon coming from the B_q vertex (the only long track) and is therefore the largest for low m_N , where the primary muon gets a larger share of the energy.

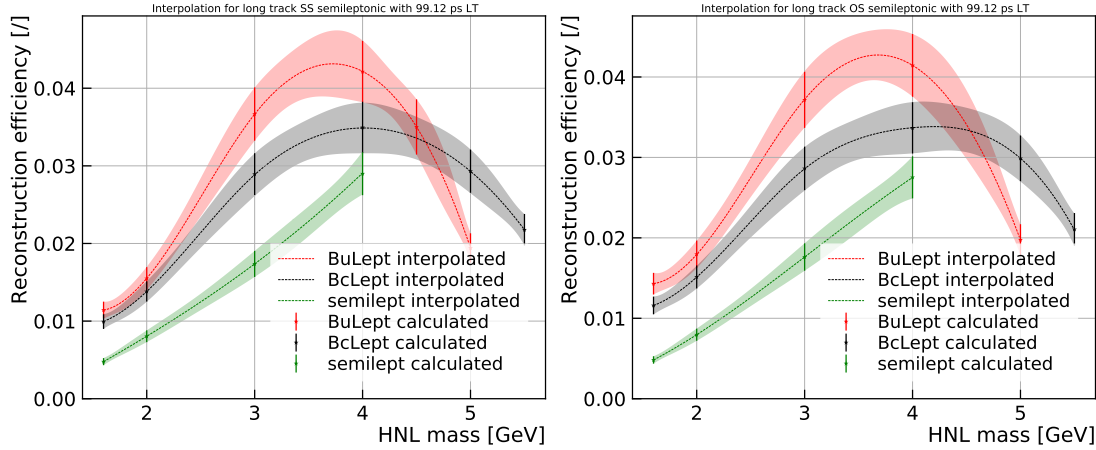


Figure 4.27 – The left (right) panel shows interpolated efficiencies for SS (OS) longstream categories as a function of m_N and for a $\tau_N = 99$ ps. The reference efficiencies at the available mass points are also shown, for comparison. The uncertainty in the interpolated efficiencies is shown as the shaded area.

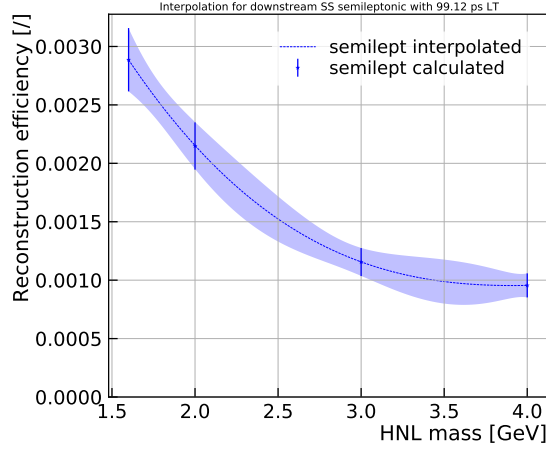


Figure 4.28 – Interpolated efficiencies for downstream category as a function of m_N and for a $\tau_N = 99$ ps. The reference efficiencies at the available mass points are also shown, for comparison. The uncertainty in the interpolated efficiencies is shown as the shaded area.

2D efficiency maps

Efficiencies are calculated for all reconstruction categories scanning the 2D plane of relevant HNL masses and lifetimes. The HNL lifetime, τ_N is scanned in a range from 1 ps to 10000 ps in logarithmic steps using the reweighting detailed in Section 4.5.3. Then for each lifetime, the efficiencies are interpolated in HNL mass as described in Section 4.5.3. Two examples of the obtained 2D efficiency maps are shown in Figure 4.29. A full set of maps for all categories can be found in the Appendix A.3.

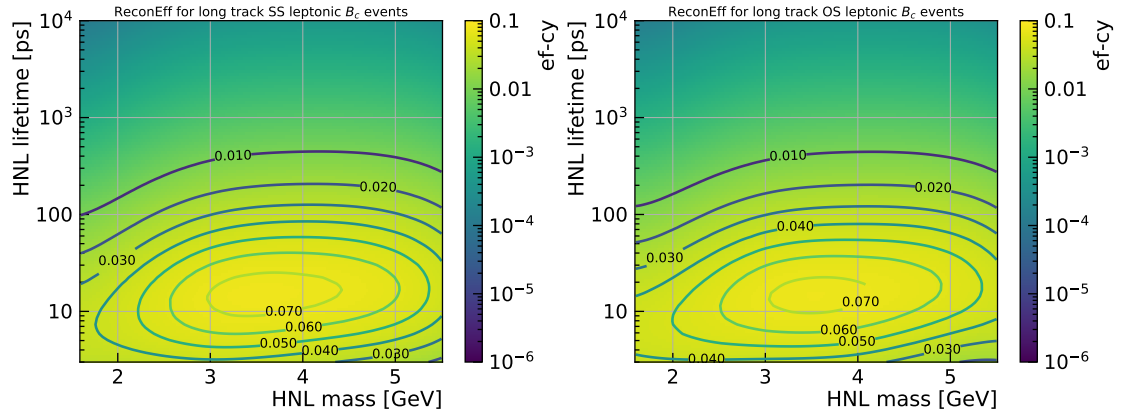


Figure 4.29 – Two examples of the reconstruction efficiency maps for the B_c leptonic, long, SS (left) and OS (right) categories. Efficiency values are encoded in the log-normal color scale with several contour-plots for the illustration purposes.

4.5.4 Correction of MC efficiencies

The selection efficiencies extracted from the MC simulation are corrected for known mismodelling of the simulation using the corrections derived from the reconstructed data detailed in the following sections.

Trigger efficiency correction

At the $L0$ stage, events are triggered by either the $L0\text{Muon}$ or the $L0\text{DiMuon}$ lines. The two offline selected signal muons are required to be responsible for the $L0$ trigger (TOS). The $L0$ trigger efficiency is therefore expected to depend solely on the transverse momenta of the two signal muons. The offline requirement of $nSPD < 450$ ensures that the effect of this general event cut can be factorised and treated separately (see the general event cut efficiency correction).

The $L0$ efficiency in MC simulation is corrected with weights extracted from a comparison between data and MC simulation based on the TIS-TOS method [56], which is a data driven method of the trigger efficiency determination at LHCb.

A data sample of events containing an offline-selected pair of muons that were triggered by the rest of the event (trigger independent of signal, or TIS) is compared to an MC signal sample selected in the same way. The $L0$ trigger selection efficiencies are calculated on both samples with TIS-TOS as

$$\epsilon_{L0} = \frac{N(\text{TOS and TIS})}{N(\text{TIS})} \quad (4.7)$$

in the two-dimensional plane of the maximum and minimum p_T of the two signal muons: $\max p_T^{\mu_i}$ and $\min p_T^{\mu_i}$. Then, the ratio of ϵ_{L0} is calculated using the reconstructed data and the MC simulation to obtain correction weights dependent on the muons p_T :

$$w_{L0}(\max p_T^{\mu_i}, \min p_T^{\mu_i}) = \frac{\epsilon_{L0}^{\text{Data}}(\max p_T^{\mu_i}, \min p_T^{\mu_i})}{\epsilon_{L0}^{\text{MC}}(\max p_T^{\mu_i}, \min p_T^{\mu_i})}. \quad (4.8)$$

Correction weights from these tables are then applied to all MC events used in the analysis to calculate signal efficiencies. The values of $\epsilon_{L0}^{\text{Data}}$, $\epsilon_{L0}^{\text{MC}}$ and w_{L0} are shown in Figure 4.30.

The high-level trigger efficiencies (see Table 4.5, A.2 in Appendix A.1) are taken from the MC simulation directly as they are known to be reproduced with a good accuracy.

General event cut efficiency correction

The efficiency of the general event cut of $nSPD < 450$ selection cannot be taken directly from the MC simulation as the $nSPD$ distribution is known to be poorly reproduced in the simulation. However, it was shown in [93] (among others) that the expected $nSPD$ distribution can be obtained with a scaling factor k^{nSPD} multiplying the $nSPD$ value of the simulation. In

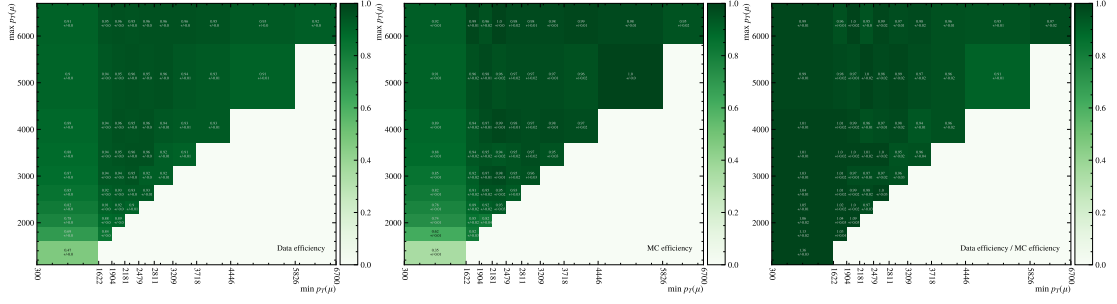


Figure 4.30 – 2D TIS-TOS efficiencies in data, MC simulation and corrections $\epsilon_{L0}^{\text{Data}}$, $\epsilon_{L0}^{\text{MC}}$ and w_{L0} (from left to right). The last p_T bin includes overflow. Figures of increased size are placed in Appendix A.4

this search k^{nSPD} is obtained by comparing data and MC samples selected with the L0DiMuon line that has a loose GEC of $n\text{SPD} < 900$. The value of k^{nSPD} is taken that equates the fraction of events with $n\text{SPD} < 450$ in the reconstructed data and the MC simulation. The resulting scaling factor is $k^{\text{nSPD}} = 1.74$ which matches the one obtained in [93]. Similarly to the results of [93], the uncertainty related to this procedure to obtain the GEC efficiency is about 10%. This number corresponds to a relative difference between the highest and the lowest GEC efficiency obtained with k^{nSPD} evaluated for HNL of different mass (see Table 4.10).

Table 4.10 – The GEC efficiency obtained for the different categories of MC samples with different HNL mass. The GEC efficiency is provided with the statistical uncertainty evaluated with MC simulation.

| HNL mass, GeV | semileptonic, % | leptonicBu, % | leptonicBc, % |
|---------------|------------------|------------------|------------------|
| 1.6 | 64.41 ± 0.35 | 67.28 ± 0.29 | 63.39 ± 0.44 |
| 2.0 | 64.44 ± 0.37 | 65.81 ± 0.14 | 62.35 ± 0.17 |
| 3.0 | 66.22 ± 0.66 | 65.11 ± 0.13 | 62.62 ± 0.14 |
| 4.0 | 62.78 ± 0.76 | 64.72 ± 0.14 | 61.38 ± 0.15 |
| 4.5 | | 64.96 ± 0.17 | |
| 5.0 | | 63.04 ± 0.39 | 61.64 ± 0.18 |
| 5.5 | | | 61.39 ± 0.22 |
| 6.0 | | | 59.96 ± 0.86 |

PID efficiency correction

In general, PID variables are slightly mismodelled by the LHCb simulation due to the several second-order effects (e.g. varying detector occupancy, inaccuracy in the detector material maps) and changes in the detector conditions and configurations during the data-taking that are hard to fully implement in simulation. There are several ways to correct for that. The most common is to discard the simulated PID response and to draw it using statistical methods from the PDF of the same variable but obtained in a well-studied calibration sample. The PDF of this distribution depends on the event kinematics and multiplicity, which is taken into account

when resampling. As these samples are taken from the reconstructed data of the pp collisions, they contain not only the calibration decay channel but also multiple background processes as well. Contribution of those backgrounds is removed using the statistical background subtraction (the `sWeights` method), which is introduced in Section 4.6.1.

The PID requirements of this analysis are summarised in Table 4.11. The $\text{ProbNN}(\pi)$ and PID_μ response is corrected using the previously mentioned data-driven method implemented in the `PIDGen2` package, which is an internal LHCb tool developed by a dedicated working group. The efficiency of the `isMuons` requirement is taken from simulation. The requirements on $\text{PID}_\mu - \text{PID}_K$ and $\text{PID}_\mu - \text{PID}_p$ have an efficiency of about 99% and are therefore taken from the MC simulation as well (the impact of MC/data corrections is expected to be at the sub-percent level and therefore neglected).

Table 4.11 – Summary of the PID selection requirements on signal candidate tracks.

| Muons | | Pions | |
|---------------------------------|-----|----------------------|-------|
| <code>isMuons</code> | = 1 | <code>isMuons</code> | = 0 |
| PID_μ | > 0 | $\text{ProbNN}(\pi)$ | > 0.6 |
| $\text{PID}_\mu - \text{PID}_K$ | > 0 | | |
| $\text{PID}_\mu - \text{PID}_p$ | > 0 | | |

Most of the PID requirements are applied at the stripping level and only a fraction of the simulation samples are not stripping filtered. In order to study the PID corrections, an additional stripping algorithm without the PID requirements was developed and applied on unfiltered simulation samples. The $\text{ProbNN}(\pi)$ response is sampled as a function of $p_T(\pi)$ and $\eta(\pi)$ from `sWeighted` PID calibration samples of $D^{*+} \rightarrow \pi^+ D^0 (K^- \pi^+)$ decay. The PID_μ response (for both muons) is sampled as a function of $p_T(\mu)$ and $\eta(\mu)$ from `sWeighted` $J/\psi \rightarrow \mu\mu$ samples where `isMuons` = 1 is required. The result of the resampling is shown in Figure 4.31.

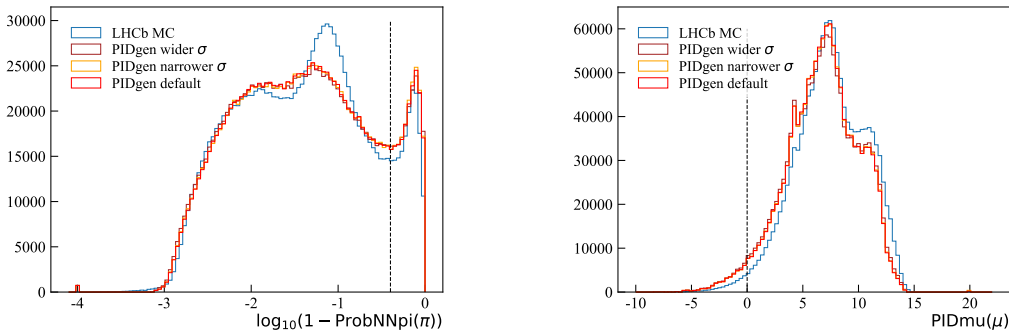


Figure 4.31 – The distributions of the resampled (left) $\text{ProbNN}(\pi)$ and (right) PID_μ variables obtained from `PIDGen2`. Three alternative templates are used for resampling, with default, narrower or wider kernels. The values of the PID requirements are shown by vertical dashed lines.

Then, similarly to the trigger efficiency correction, the data/MC efficiency correction factors are computed for the requirements on $\text{ProbNN}(\pi)$ and PID_μ using the unfiltered MC samples

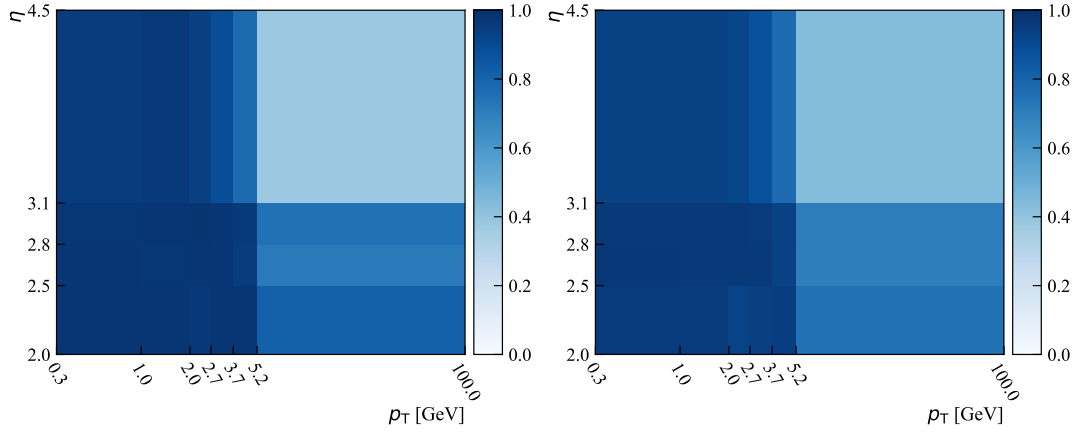


Figure 4.32 – The $\text{ProbNN}(\pi) > 0.6$ efficiency obtained from the MC PID response (left) and PIDGen2 resampling (right).

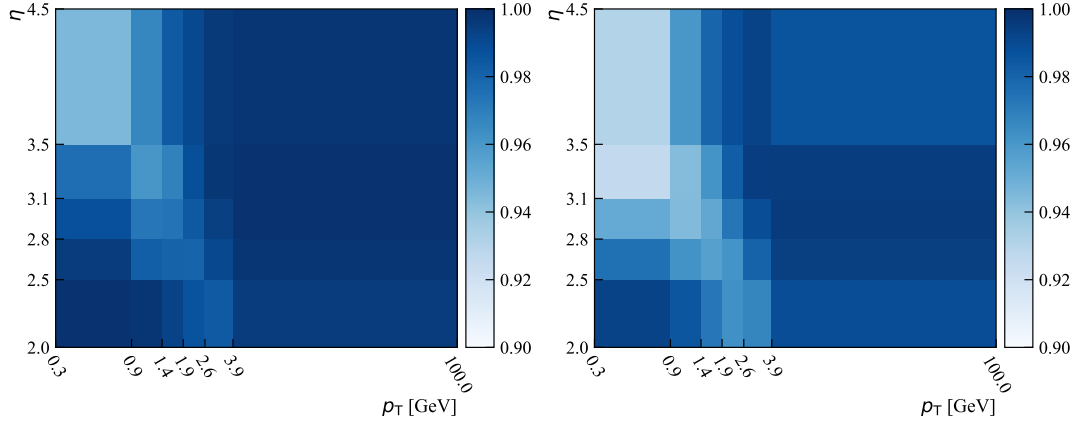


Figure 4.33 – The $\text{PID}_\mu > 0$ efficiency obtained from the MC PID response (left) and PIDGen2 resampling (right).

with removed PID selection. The efficiency correction weights are calculated as a function of p_T and η of the muons and pions as shown in Figure 4.32, 4.33 and 4.34. Per-event weights drawn from this study are used to correct all MC samples, resulting in a correction of the PID efficiency that depends on the kinematics of the sample considered. The overall size of the PID data/MC efficiency correction is about -5% .

The templates to resample $\text{ProbNN}(\pi)$ and PID_μ using PIDgen2 are obtained using 4D images in 100 bins of p_T and η and 50 bins of N_{tracks} . Gaussian smearing is added on top to get smooth templates to sample from. The uncertainty related to this procedure is evaluated by using both a narrower and a wider kernel for the Gaussian smearing. The resulting $\text{ProbNN}(\pi)$ and PID_μ distributions are shown in Figure 4.31 and are very similar to the ones obtained with the standard template. The efficiency of all PID requirements using these alternative templates stays within 0.5% of the default one. Therefore, this systematic uncertainty is neglected.

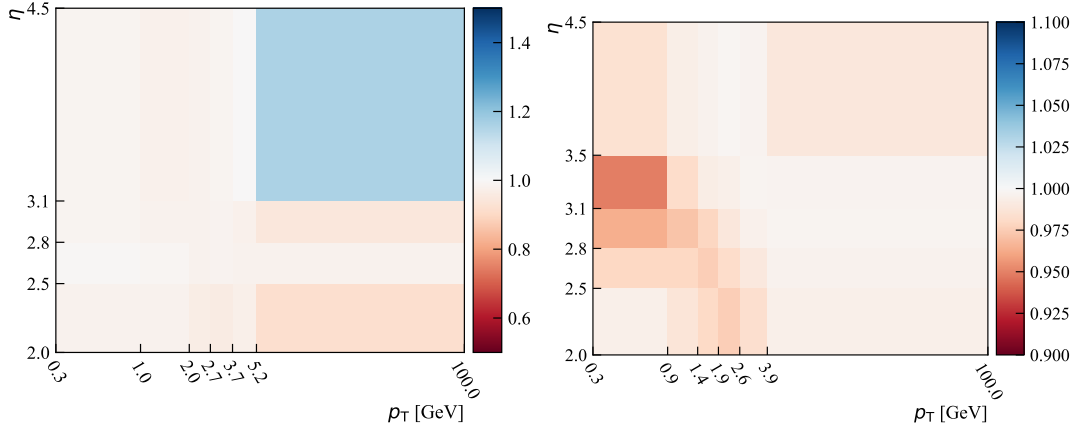


Figure 4.34 – The data/MC correction factor obtained by taking the ratio of the efficiencies obtained from the MC PID response and PIDGen2 resampling. Left is for $\text{ProbNN}(\pi) > 0.6$, right is for $\text{PID}_\mu > 0$.

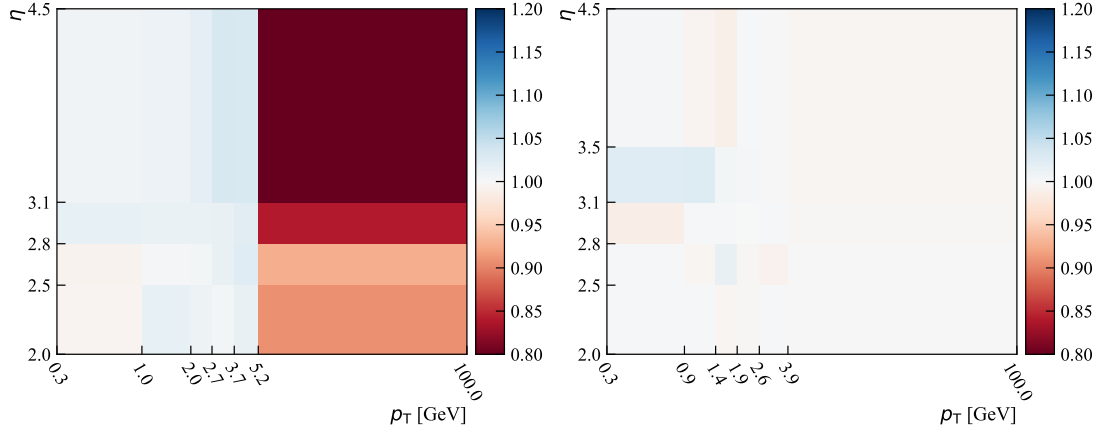


Figure 4.35 – The ratio between the pion (left) and muon (right) PID efficiency for downstream over that for long tracks obtained from the MC.

The data/MC efficiency correction is obtained from calibration samples of long tracks and applied to both long and downstream tracks assuming the differences are negligible. The difference in the PID efficiency between downstream and long track selections is of a few percents, but is coming mainly from the different (p_T, η) spectrum of the two samples. These differences were studied on the MC samples in bins of p_T and η as shown in Figure 4.35. Sizeable differences are observed only for pions with very large p_T (a region with very low statistics). Shown maps of the efficiency ratios then are used to take the (p_T, η) spectrum differences out of the equation. When it is done, the resulting PID efficiency for downstream category is just 0.5% lower than that of the long one. Therefore, it is expected that the data/MC efficiency correction on top of this effect will be even smaller and can be neglected.

4.6 Peaking backgrounds in the search mass region

While smoothly falling combinatorial background shape is enough to describe the combinatorial background in almost all search regions, the peaking background from D^0 mesons is found to be important for the HNL masses between 1.7 and 1.9 GeV. Since the final signal extraction is done with the fit to the distributions with very few events, it is not possible to include the peaking background shape with free parameters into the fit model, as in the signal region there is no sensitivity to reliably extract them. Therefore, a custom data-driven method was developed to measure the peaking background shape and its yield, which are then included into the final fit for the signal extraction with the shape and normalization parameters constrained to their measured values within their measured uncertainties.

4.6.1 Statistical background subtraction

If a data sample is populated by several sources of events, like signal and background, or samples of different lifetimes, it is possible to unfold the contributions of the different sources for a given variable. A statistical tool to unfold data distributions is called s Plot [94]. It is performed by fitting a PDF with signal and background components to a chosen *discriminating* variable distribution and extracting the so-called s Weights for each data point (event)

$$W_n(x) = \frac{\sum_{j=1}^{N_s} V_{nj} f_j(x)}{\sum_{k=1}^{N_s} N_k f_k(x)} \quad (4.9)$$

with

$$V_{nj}^{-1} = \sum_{e=1}^{N_s} \frac{f_n(x_e) f_j(x_e)}{(\sum_{k=1}^{N_s} N_k f_k(x))^2}, \quad (4.10)$$

where N_s is the number of events sources n in the data sample (in our case 2), and f_n , N_n are the PDF function and its normalisation for the source n .

Computed s Weights then can be used to obtain the signal-only components in the distributions of *control* variables. To avoid biases when using control variables they have to be uncorrelated with the discriminating ones.

4.6.2 Swap of the mass hypotheses

Despite the stringent requirements on displacement and PID of the pion and muon candidates, the HNL mass region below 2 GeV is populated by D^0 two-body hadronic decays. Using the upper B -mass sideband region of the reconstructed data for the *semileptonic* category, $m(\mu\mu\pi) > 3.4$ GeV, with only preselection and trigger applied, one can see two peaks in the $\mu\pi$ spectrum shown in Figure 4.36. As concluded further, these peaks belong to D^0 decays. To identify the aforementioned decays, several misidentification (misID) hypotheses were tested, where single or both 4-vectors are recalculated under μ , π , or K hypotheses.

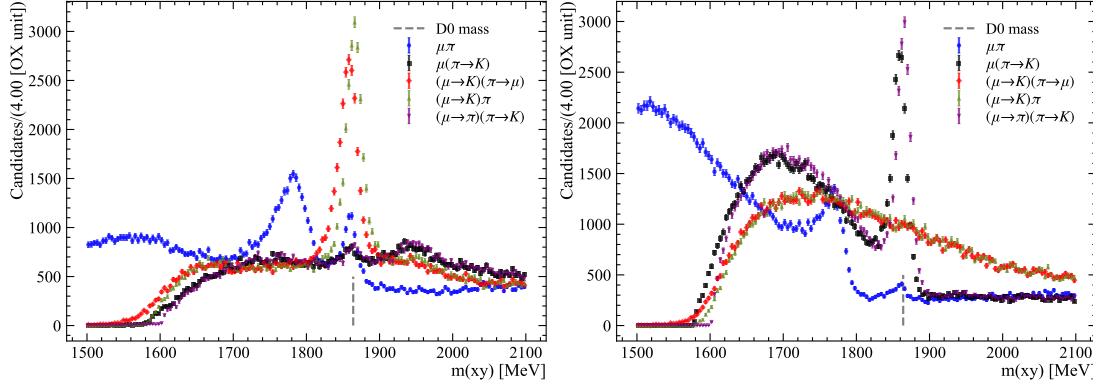


Figure 4.36 – Mass spectrum of two tracks forming an HNL vertex, which is calculated under different mass hypotheses, (left) for the SS category and (right) for the OS category. Two peaks correspond to $D^0 \rightarrow K^- \pi^+$ and $D^0 \rightarrow \pi^- \pi^+$, respectively.

Two decays with high branching ratios (BR) are consistent with our topology and therefore considered: $D^0 \rightarrow K^- \pi^+$ with BR of 3.90% and $D^0 \rightarrow \pi^- \pi^+$ with BR of 0.24%. In an effort to verify this, the \mathcal{S} Plot technique was applied to isolate events falling under different peaks and correct them using the corresponding hypothesis. In Figure 4.37 top, fit to the SS and OS data with Johnson PDF [95] (see Section 4.6.2) for the signal and a single (or two exponentials) for the combinatorial background is shown. The \mathcal{S} Weights values for the first peak are derived labeling the second peak with exponential as a background. Then, $\mu \rightarrow K$ hypothesis correction was applied only to signal-weighted events, see Fig. 4.37 bottom. The same procedure is applied for the second peak. Difference in the rates fractions between the two peaks for the SS and OS categories can be explained by a selection of $FD_Z > 5mm$ applied on the OS category, which was placed on the stripping stage to reduce the SM decays rates. Most likely, with our decay topology, $B^+ \rightarrow \mu^+ N (\rightarrow \mu^\pm \pi^\mp)$ the $B^+ \rightarrow \pi^+ \bar{D}^0 (\rightarrow K^+ \pi^-)$ decay is observed here. This explains the fact that, in order to fulfil the charge conservation requirement for the SS category we need to have $(\mu \rightarrow K)\pi$ misID, whereas for OS it is a double misID $(\mu \rightarrow \pi)(\pi \rightarrow K)$, see Figure 4.36.

The Johnson PDF that used to describe the shape of peaking background is defined as

$$\mathcal{B}_{\text{peaking}}^i(m; \theta^i) = N_{\text{peaking}}^i \times \frac{1}{\lambda \sqrt{2\pi}} \frac{1}{\sqrt{1 + \left(\frac{x-\xi}{\lambda}\right)^2}} e^{-\frac{1}{2} \left(-v + \sinh^{-1} \left(\frac{x-\xi}{\lambda} \right) \right)^2} \quad (4.11)$$

with

$$\lambda = \sigma \times \left(\frac{1}{2} (\exp\{\tau^2 - 1\}) (\exp\{\tau^2\}) \cosh(\nu\tau + 1) \right)^{-1/2}$$

$$\xi = \mu + \lambda \exp\left\{\left(\frac{\tau^2}{2}\right)\right\} \sinh(\nu\tau),$$

where N_{peaking}^i is the background yield and nuisance parameters are $\theta^i = (\mu, \sigma, \nu, \tau)$.

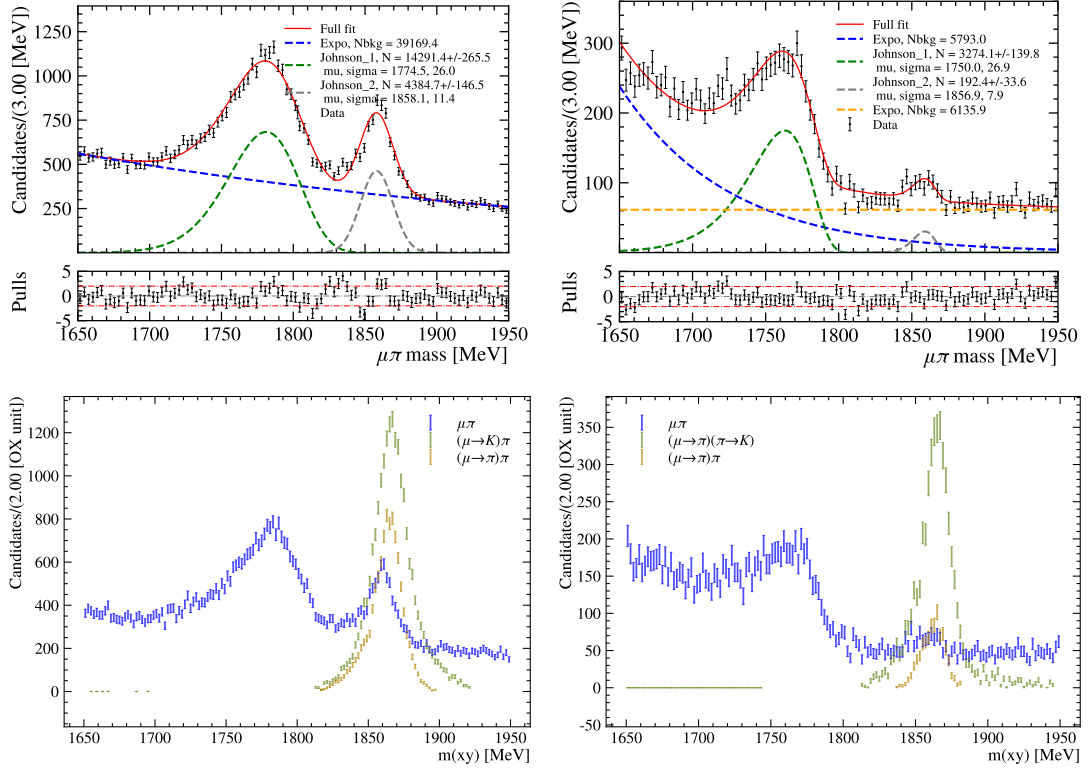


Figure 4.37 – (top) Fit to (left) SS and (right) OS sideband data and (bottom) two separately corrected mass hypotheses using s Weights to isolate the two peaks.

4.6.3 The ABCD method

Once decays are identified using the sideband data, one could estimate peaking backgrounds yields in the long categories using a data-driven extrapolation evaluated on the prompt category, which is well excluded by other experiments and not considered for a final fit in this analysis. The ABCD method [96] is used, which applies selection on two statistically independent variables, separating signal and background into four regions, so that the background in the signal region can be estimated using the other three control regions.

These regions are defined with the HNL FD_Z and $m(\mu\mu\pi)$ variables, see Figure 4.38, left. They

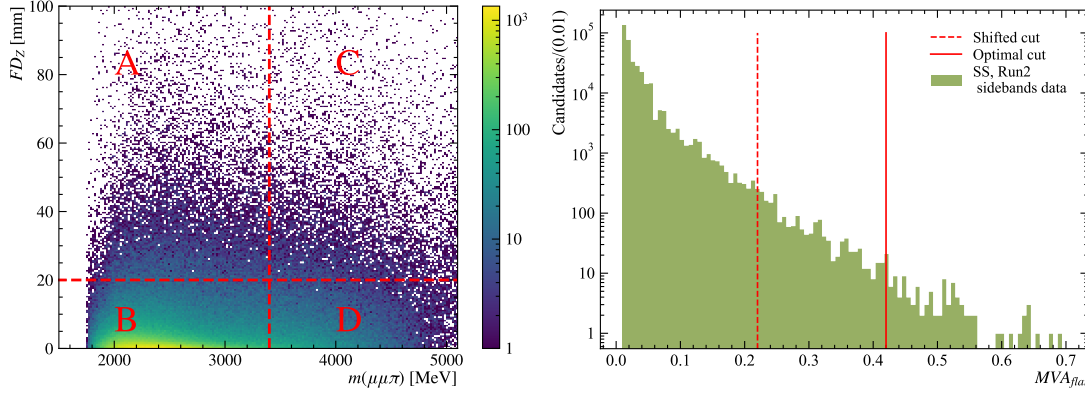


Figure 4.38 – (left) 2D histogram of the HNL FD_Z vs $m(\mu\mu\pi)$ with indicated ABCD regions for the SS category. Orthogonal to working point selection on MVA_{flat} variable is used in order to not unblind the signal region. (right) MVA_{flat} distribution for the sideband data with the sub-region windows: $MVA_{flat} > 0.42$ is the signal selection, denoted by the solid line. The dashed line corresponds to the shifted cut value by an arbitrary X_{BD} and illustrates a region, $MVA_{flat} > 0.42 - X_{BD}$, used for the validation studies.

are statistically independent, with correlation coefficient of 0.1, and are physically motivated. They are splitting our phase space into prompt (B, D) and long (A, C) regions on Y axis. Then, on X axis, are defined the signal (A, B) and the sideband (C, D) mass regions. In this way, the background yields in the region of interest A are measured with the control regions B, C and D, using relation $N_A/N_B = N_C/N_D$. The N_X value is the peaking background yield in a region X, extracted from the fit to the invariant mass spectrum with the sum of the Johnson PDF and the exponential PDF, which describes the combinatorial component. The shape parameters of Johnson PDF are measured in a well populated region D, and are fixed to found values when fitting to the regions A, B and C. Parameters of the exponential shape are free to vary in each region. The mass hypothesis swap studies are done using the datasets without the MVA selection applied, but yield estimations are performed with the final selection in place, which limits the number of available events and worsens statistical precision of the prediction.

Validating the ABCD method

In order to be able to quantify the prediction accuracy and later improve it without unblinding the region A, the background-enriched subsets B and D are split in half along the Y axis to four control regions A', B', C' and D'. Then, to improve the statistical uncertainties, the MVA selection is loosened separately on A', C' and B', D' regions by $X_{A'C'}$ and $X_{B'D'}$ values respectively, which does not change the yield ratios between these regions, i.e. N_A/N_C and N_B/N_D . To validate the feasibility of such approach and evaluate the prediction dependency on the MVA selection, the ABCD prediction as a function of $X_{A'C'}$ and $X_{B'D'}$ was studied. At first, a fit to the control regions is done for an arbitrary shift of $X_{A'C'} = X_{B'D'} \approx 0.3$ and is shown in Figure 4.39, which

4.6. Peaking backgrounds in the search mass region

gives

$$\frac{N_{A'}^1(\text{true})}{N_{A'}^1(\text{predicted})} = 0.83 \pm 0.12 \quad (4.12)$$

for the left peak, and

$$\frac{N_{A'}^2(\text{true})}{N_{A'}^2(\text{predicted})} = 0.99 \pm 0.15 \quad (4.13)$$

for the right peak. This proves that the concept works for a single MVA_{flat} selection value, which is quite far from the working point.

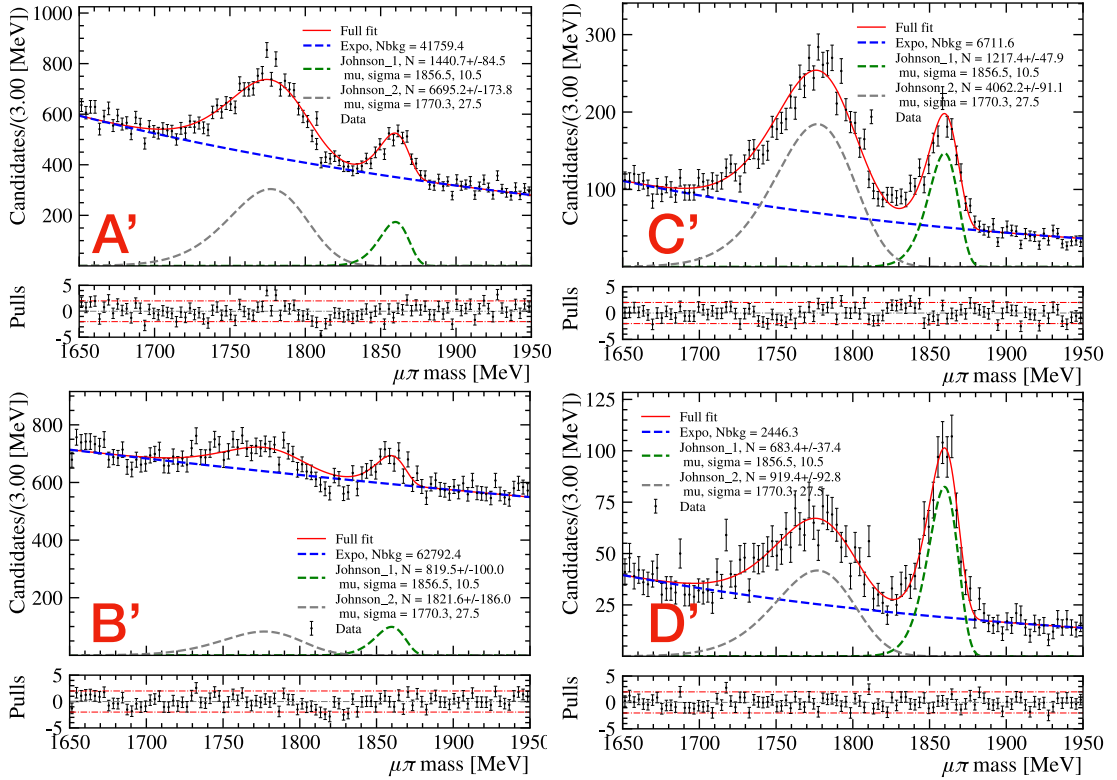


Figure 4.39 – Fit to A' , B' , C' and D' regions, defining yields for the ABCD method validation.

Then, to prove that the conclusions obtained in the far MVA_{flat} selection region are valid in the signal MVA_{flat} selection, the performance of this method is tested as a function of the selection value for the MVA_{flat} variable. For this, the N_i' yields were measured as a function of the windows positions $X_{A'C'}$ and $X_{B'D'}$. For a given $X_{A'C'}$ ($X_{B'D'}$), yields are measured in the following way:

- a mass fit window is fixed to [1650, 1950] MeV, which has boundaries approximately equal to 5σ mass resolution offset from the peaks positions;
- fit to the region D' first, with all parameters allowed to vary;
- extract peaks shape and position parameters as well as the yields in the region D' ;

- fit to A' , B' and C' regions fixing the peak shape parameters to values from the region D' while allowing the yields and the combinatorial background parameters to vary;
- then, extract yields for the regions A' , B' and C' .

In this way, deducing from the scans shown in Figure 4.40, values $X_{B'D'}$ of 0.3 and $X_{A'C'}$ of 0.01 were chosen, where the ratio is flat (following instructions from [96]), with final fits shown in Figure 4.41. This gives us the prediction values of $N_A^1 = 1.5^{+4.8}_{-1.5}$ and $N_A^2 = 3.8 \pm 3.6$ for the SS category and $N_A^1 = 2.9^{+4.7}_{-2.9}$ and $N_A^2 = 3.3 \pm 3.1$. These yields as well as the PDFs parameters are used in the bump hunt scans to describe peaking backgrounds in addition to the combinatorial one. Since we have large statistical uncertainty coming from the low statistics in the C region, any other systematic uncertainties were not assigned on the ABCD method.

Similar studies on J/ψ peak gave yields compatible with 0 in the long category and are not taken into account in the final fit.

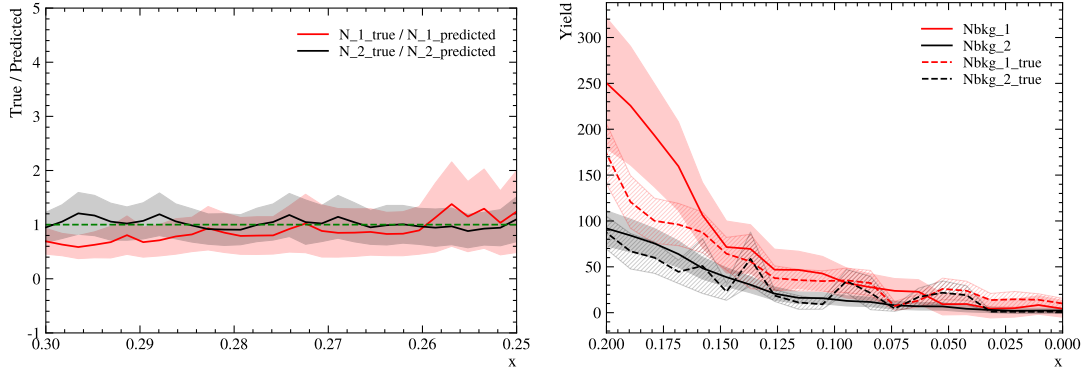


Figure 4.40 – (left) The closure test ($N_{\text{true}}/N_{\text{predicted}}$) as a function of $X_{A'C'}$, where the $X_{B'D'}$ value is fixed to 0.2. (right) Trends of N_{true} and $N_{\text{predicted}}$ as a function of $X_{A'C'}$, while $X_{B'D'}$ is fixed to 0.3. Lines are the central values, while filled area are the statistical uncertainties.

4.6. Peaking backgrounds in the search mass region

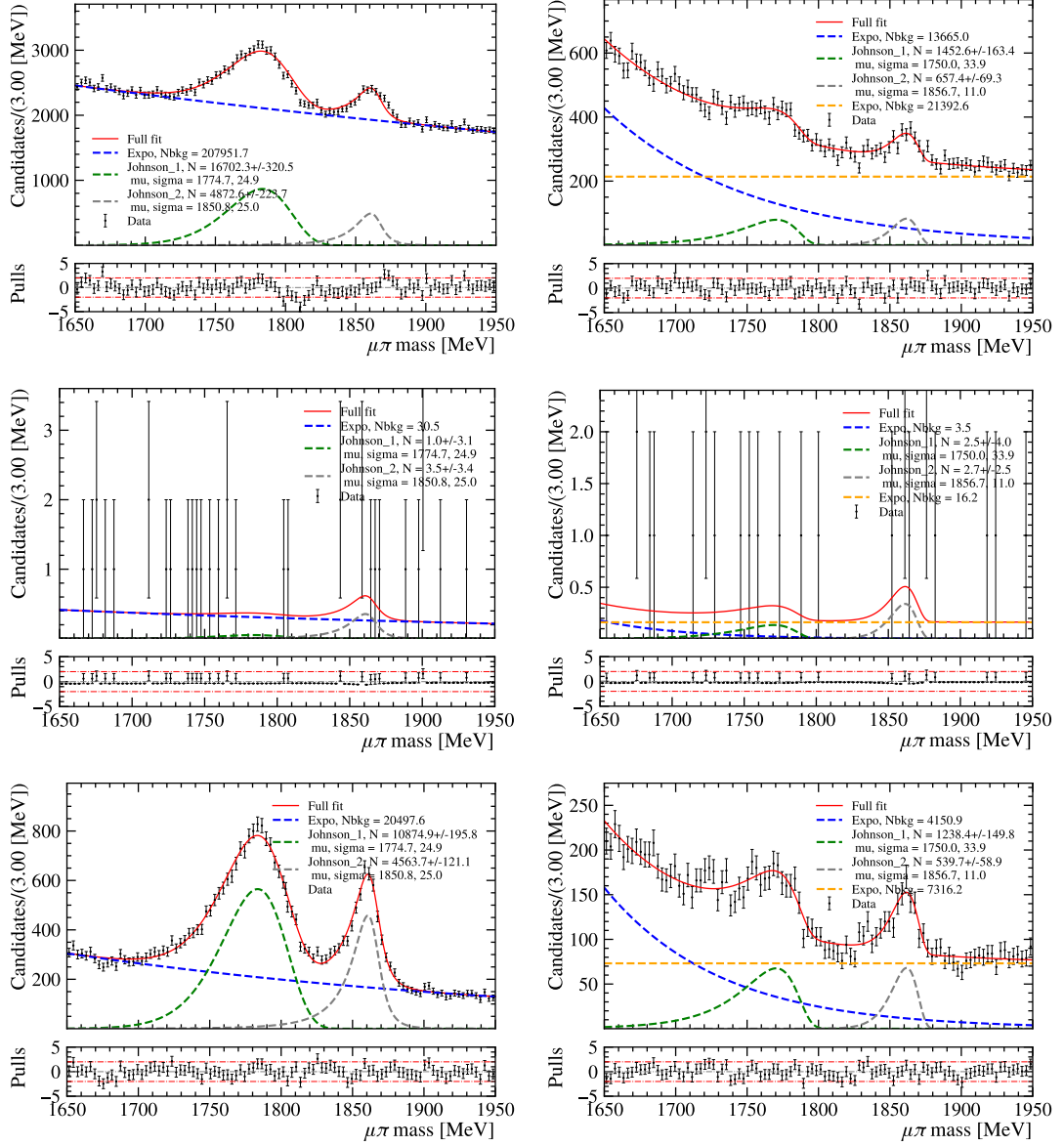


Figure 4.41 – B , C and D regions fits to (left) the SS data, and (right) the OS data.

4.7 Search for the signal peak in the invariant mass spectrum

In this analysis, the number of observed events is directly extracted from the invariant mass spectrum of the reconstructed N mass. It is performed blindly in the whole range of the $m(\mu\pi)$ spectrum, applying a peak search algorithm where the test mass, m_t , is incremented in steps of σ_m , where σ_m is the mass resolution at m_t . The width of the test window, where the fit is performed, is defined as $|m - m_t| < 7\sigma_m$. In total, each category of the search has around 200 fits in a range from 1.6 to 5.5 GeV. The goal of this algorithm is to point out the presence of a local data excess corresponding to a resonant production of a massive particle, or otherwise to compute an upper limit (UL) on the signal yield using a confidence levels (CL_s) method [97]. The fit strategy, signal parameterisation and CL_s method are described in the following section.

4.7.1 Signal parameterisation

The size of the local search window, mass peak shape, and mass steps are dependent on the mass and lifetime of considered HNL candidate. The signal mass shape is extracted from the simulated samples and modeled by the double-sided Crystal Ball PDF, which is composed of a Gaussian distribution at the core, connected with two power-law distributions describing left and right tails and defined as

$$\mathcal{S}(m; \theta_S) = \begin{cases} \left(\frac{n_L}{|\alpha_L|} \right)^{n_L} e^{-\frac{|\alpha_L|^2}{2}} \left(\frac{n_L}{|\alpha_L|} - |\alpha_L| - \frac{m-m_N}{\sigma} \right)^{-n_L}, & \text{for } \frac{m-m_N}{\sigma} \leq -\alpha_L \\ e^{-\frac{1}{2} \left(\frac{m-m_N}{\sigma} \right)^2}, & \text{for } -\alpha_L < \frac{m-m_N}{\sigma} < -\alpha_R \\ \left(\frac{n_R}{|\alpha_R|} \right)^{n_R} e^{-\frac{|\alpha_R|^2}{2}} \left(\frac{n_R}{|\alpha_R|} - |\alpha_R| - \frac{m-m_N}{\sigma} \right)^{-n_R}, & \text{for } \frac{m-m_N}{\sigma} \geq -\alpha_R, \end{cases} \quad (4.14)$$

with short notation $\theta_S = (\alpha_L, n_L, \alpha_R, n_R, m_N, \sigma)$, where m_N is the mass central value, σ is the width of the Gaussian core, α_L and n_L are the shape parameters of the left (L) and right (R) tail respectively. Example of fits for several m_N can be seen in Figure 4.42. An exhaustive list for all the masses can be found in Appendix A.5.

Each search category has its own mass shape. The mass distributions are identical for all considered lifetimes (see Figure 4.43, left), while the dependence of the mass shape on the true HNL mass has to be taken into account. Since only a few mass points could be simulated, the shape of the mass PDF for intermediary mass points is estimated using the moment morphing technique [98]. All simulated samples are used to construct the interpolation object, which provides a mass shape for any given m_N in the range of mass search, as shown in Figure 4.43 on the right. The resulting PDFs are used in the fit to data with fixed parameters. The mass resolution σ_m , which is a fit parameter, is interpolated in the search range using a cubic spline in order to define the mass windows for the peak search algorithm, and is shown in Figure 4.44.

4.7. Search for the signal peak in the invariant mass spectrum

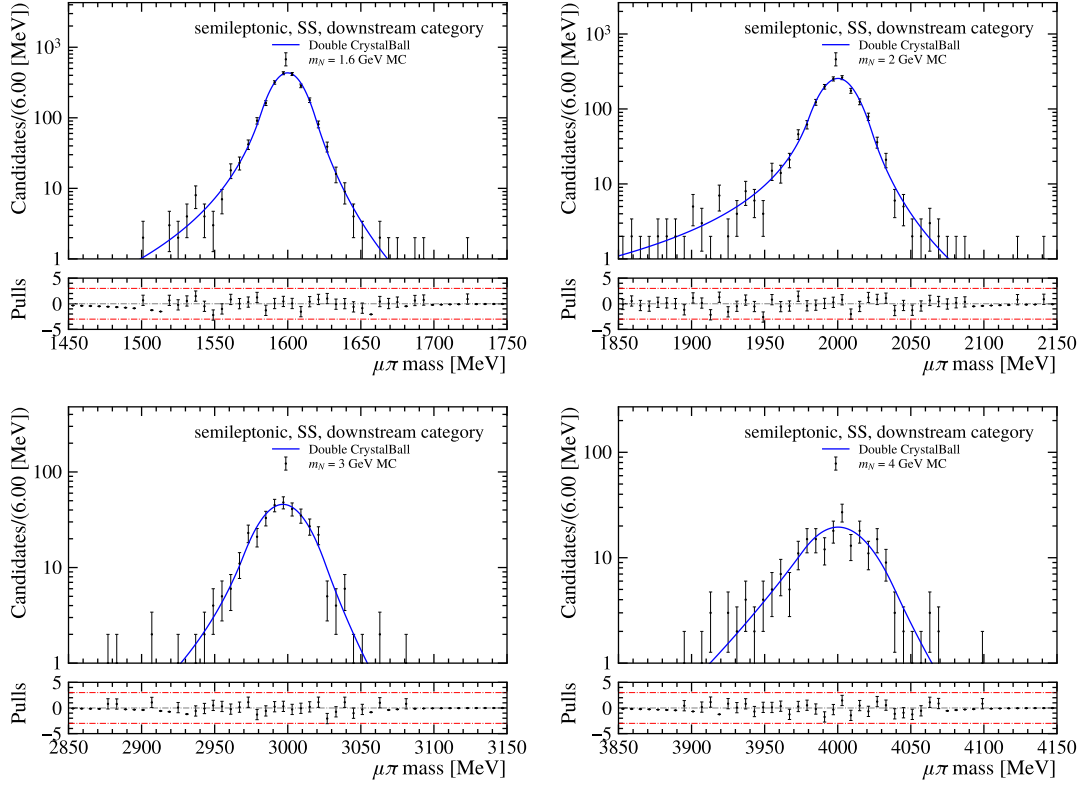


Figure 4.42 – Examples of fits to the simulated signal for $m_N = 1.6, 2, 3, 4$ GeV.

4.7.2 Background parameterisation

Combinatorial background

The combinatorial background yield is extracted directly from a fit to the data, assuming either a linear or an exponential shape with a very flat decay constant

$$\mathcal{B}_{\text{comb}}(m; m_N, N_{\text{comb}}, \alpha_{\text{comb}}) = \begin{cases} N_{\text{comb}} \times e^{-\alpha_{\text{comb}} m}, & \text{default model} \\ N_{\text{comb}} \times (1 + \alpha_{\text{comb}} m), & \text{alternative model,} \end{cases} \quad (4.15)$$

where the PDF normalisation N_{comb} and the shape parameter α_{comb} are allowed to vary in the fit and are independent among the analysis categories. The resulting shape accommodates the data in a satisfactory manner, except in regions where peaking backgrounds are present, which require additional care.

Peaking backgrounds

The region where the peaking backgrounds, defined in Section 4.6, are present has lower and upper boundaries of 1650 and 1950 MeV, respectively. There are two additional peaking

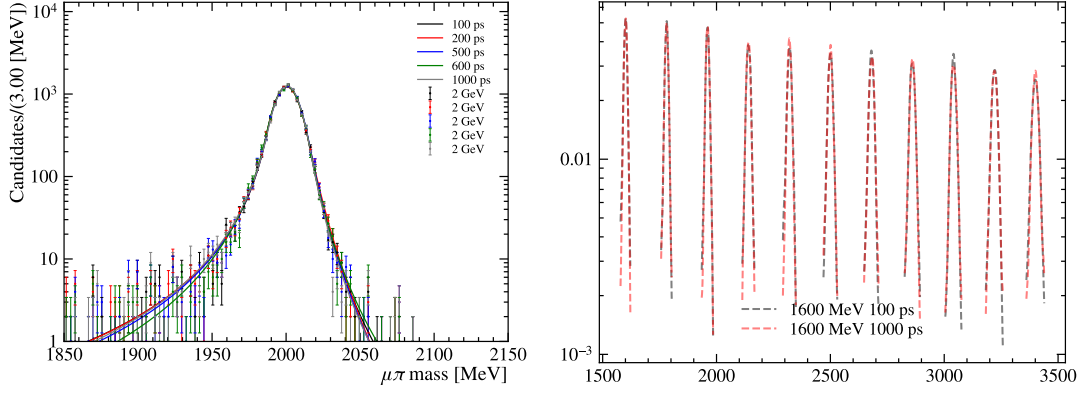


Figure 4.43 – (left) MC samples with a true N mass of 2 GeV with reweighted lifetimes and fitted with double Crystal Ball PDFs. (right) Interpolated mass shapes for two lifetimes, showing no significant difference between PDFs.

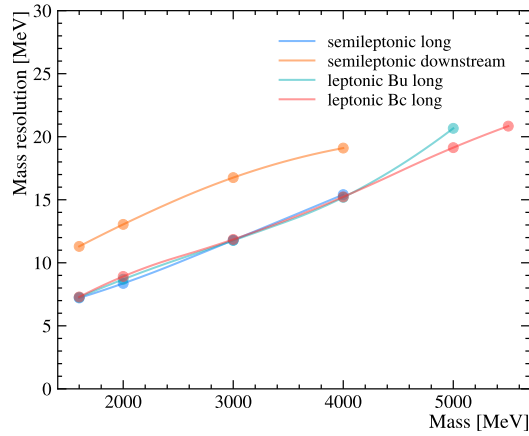


Figure 4.44 – Interpolated σ_m between simulated mass points for the SS categories. Marker points are corresponding to the values extracted from the fit, and solid lines are interpolated.

background PDFs are included in addition to the combinatorial one. The normalisation, shape parameters and positions of these PDFs are fixed to the values computed with the ABCD method, as discussed in Section 4.6. The peaking background region in the mass spectrum is defined as $\mu_i \pm 5\sigma_i$, where μ_i and σ_i are the mean and resolution of the Gaussian cores of the peaking background PDFs. Components of the peaking background are only present in the semileptonic categories of the search.

The total PDF

Taking into account Section 4.7.2 and 4.11, the total background PDF used in this analysis is

$$\mathcal{B}_i(m; m_N, \theta_B) = \begin{cases} \mathcal{B}_{\text{comb}}(m; m_N, \theta_{\text{comb}}), & \text{for } m_N \notin [1650, 1950] \text{ MeV} \\ \mathcal{B}_{\text{comb}}(m; m_N, \theta_{\text{comb}}) + \mathcal{B}_{\text{peaking}}^1(m; m_N, \theta^1) + \mathcal{B}_{\text{peaking}}^2(m; m_N, \theta^2) \end{cases} \quad (4.16)$$

4.7.3 Fit to data

For each category of the search, the fit is performed simultaneously on all the categories of the HNL displacement, sharing a common yield parameter, N_{sig} . In order to extract yields, the signal and background models are used in combination, with separate yield parameter for each PDF, and defined over the aforementioned fit window. By taking into account PDFs denoted in Section 4.7.1 and 4.16, signal-plus-background ($s+b$) parameterisation becomes

$$\begin{aligned} \mathcal{PDF}_i(m; m_N, N_{\text{sig}}, \theta) &= N_{\text{sig}} \times \epsilon_i \times \mathcal{S}_i(m; \theta_S) \\ &+ \mathcal{B}_i(m; m_N, \theta_B), \end{aligned} \quad (4.17)$$

where N_{sig} is our parameter of interest (POI), ϵ_i is the events fraction in the category i and nuisance parameters (background yield, exponential slope, etc.) are denoted by $\theta = (\theta_S, \theta_B)$. The likelihood for the search category i is:

$$\mathcal{L}_i(N_{\text{sig}}, \theta, m_N) = \frac{e^{N_i} N_i^{N_{\text{obs};i}}}{N_{\text{obs};i}!} \times \prod_{j=1}^{N_{\text{obs};i}} \mathcal{PDF}_i(m_j; m_N, N_{\text{sig}}, \theta) \times \mathcal{C}_{\text{bkg};i} \times \mathcal{C}_{\epsilon_i}, \quad (4.18)$$

where $N_{\text{obs};i}$ is the observed number of candidates in that bin, and $N_i = N_{\text{sig};i} + N_{\text{bkg};i}$. $\mathcal{C}_{\text{bkg};i}$ are the Gaussian constraints on the peaking backgrounds normalisations, defined as

$$\mathcal{C}_{\text{bkg};i} = \frac{1}{\sqrt{2\pi}\sigma_{N_1}} \exp\left(-\frac{(\mu_{N_1} - N_1)^2}{2\sigma_{N_1}^2}\right) \times \frac{1}{\sqrt{2\pi}\sigma_{N_2}} \exp\left(-\frac{(\mu_{N_2} - N_2)^2}{2\sigma_{N_2}^2}\right), \quad (4.19)$$

where μ_{N_i} and σ_{N_i} are the central values and uncertainties of the peaking background yield, N_i , extracted from the fit in the ABCD method. \mathcal{C}_{ϵ_i} is the Gaussian constraint on the signal efficiency in the bin i

$$\mathcal{C}_{\epsilon_i} = \frac{1}{\sqrt{2\pi}\sigma_{\epsilon_i}} \exp\left(-\frac{(\mu_{\epsilon_i} - \epsilon_i)^2}{2\sigma_{\epsilon_i}^2}\right), \quad (4.20)$$

where the central value and uncertainty in ϵ_i are obtained from MC simulation.

To perform model fitting, the unbinned maximum log-likelihood method is employed, where

combined likelihood for the simultaneous fit in categories of the search is expressed by

$$\mathcal{L}(N_{\text{sig}}, \theta, m_N) = \prod_{i=1}^{N_{\text{bins}}} \mathcal{L}_i(N_{\text{sig}}, \theta, m_N). \quad (4.21)$$

The fitting procedure, parameters handling and PDFs definition is performed using the *zfit* library [99]. An example of the fit to a toy data sample (generated using a technique outlined in Section 4.7.8) in a region with the peaking background is shown in Figure 4.45.

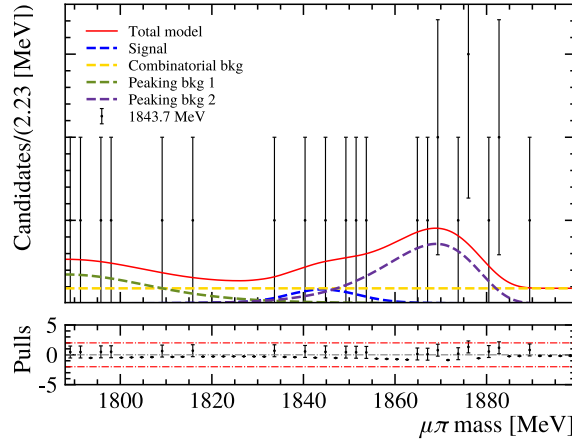


Figure 4.45 – Fit result to the $m(\mu\pi)$ distribution in a toy dataset of the inclusive, SS, displLL category.

The data fits are performed on a merged dataset containing all different years of data-taking in Run 2, merged together. This allows to gain sensitivity at the region of the higher HNL masses, which is less populated, and does not require any special treatment to the data samples since the conditions of the data-taking did not change for our candidates.

4.7.4 CL_s method

After the results of the fit to data are obtained, the significance of this measurement is evaluated by performing a hypothesis test where the null and alternative hypotheses are defined as

- H_0 , the null or background-only hypothesis b , i.e. $N_{\text{sig}} = 0$;
- H_1 , the alternative hypothesis $s + b$, i.e. $N_{\text{sig}} = \hat{N}_{\text{sig}}$, where \hat{N}_{sig} is the fit result.

The test statistic used is the likelihood ratio for the two hypotheses. For testing the discovery, it is defined as

$$q_0 = \begin{cases} -2 \ln \frac{\mathcal{L}(N_{\text{sig}}=0, \hat{\theta})}{\mathcal{L}(N_{\text{sig}}=\hat{N}_{\text{sig}}, \hat{\theta})} & \text{if } \hat{N}_{\text{sig}} \geq 0 \\ 0 & \text{if } \hat{N}_{\text{sig}} < 0 \end{cases} \quad (4.22)$$

4.7. Search for the signal peak in the invariant mass spectrum

where $\hat{\theta}$ and $\hat{\hat{\theta}}$ are the best fitted values of the nuisances parameters for the null and alternative hypotheses, respectively.

If the resulting number of observed events is consistent with zero, the UL on it is set using the following test statistics

$$q_{N_{\text{sig}}} = \begin{cases} -2 \ln \frac{\mathcal{L}(N_{\text{sig}}, \hat{\theta})}{\mathcal{L}(N_{\text{sig}} = \hat{N}_{\text{sig}}, \hat{\hat{\theta}})} & \text{if } \hat{N}_{\text{sig}} \leq N_{\text{sig}} \\ 0 & \text{if } \hat{N}_{\text{sig}} > N_{\text{sig}}. \end{cases} \quad (4.23)$$

A p-value of the signal-plus-background hypothesis can be computed from the test statistic distribution, following

$$p_{N_{\text{sig}}} = \int_{q_{N_{\text{sig}}}^{\text{obs}}}^{\infty} f(q_{N_{\text{sig}}} | N_{\text{sig}}) dq_{N_{\text{sig}}} = 1 - CL_{s+b}, \quad (4.24)$$

and for the background-only hypothesis it is

$$p_0 = \int_{q_0^{\text{obs}}}^{\infty} f(q_0 | H_0) dq_0 = 1 - CL_b, \quad (4.25)$$

where q_0^{obs} is the value of the test statistic evaluated on observed data, CL_{s+b} and CL_b are the confidence levels of these hypotheses.

In the CL_s method the confidence level is modified to

$$CL_s = 1 - \frac{CL_{s+b}}{CL_b}. \quad (4.26)$$

Now, the observed UL on the POI N_{sig} is defined as the value of N_{sig} for which $1 - CL_s > 95\%$. The expected UL on N_{sig} is obtained by repeating the procedure using q values taken from $f(q_0 | H_0)$ instead of $q_{N_{\text{sig}}}$ for the background-only hypothesis.

The UL is found by interpolating the p-values as a function of N_{sig} , using the asymptotic approximations for the test statistic [100], which is implemented in the *hepstats* library [101]. Under this assumption, q_0 follows a χ^2 (ndof = 1) which simplifies the p-value computation to

$$p_0 = 1 - \Phi\left(\sqrt{q_0^{\text{obs}}}\right). \quad (4.27)$$

The validity of the asymptotic approximation of the test statistic has been performed in great details in a similar LHCb analysis [102], by comparing upper limits computed by the *hepstats* asymptotic calculator and by using pseudo-experiments. A good agreement between the two methods is found.

4.7.5 $\frac{f_q}{f_u} \cdot \text{BR}(B_q \rightarrow X\mu^+ N) \cdot \text{BR}(N \rightarrow \mu^+ \pi^-)$ as a parameter of interest

The number of detected events in this analysis can be expressed as

$$N_{\text{sig}} = \mathcal{L} \cdot \frac{\sigma_{pp \rightarrow B^\pm X}}{\epsilon_{pp \rightarrow B^\pm X}} \cdot \frac{f_q}{f_u} \cdot \text{BR}(B_q \rightarrow X\mu^+ N) \cdot \text{BR}(N \rightarrow \mu^+ \pi^-) \cdot \epsilon_{\text{tot}}, \quad (4.28)$$

where

- \mathcal{L} is the integrated luminosity of the analysed dataset;
- $\sigma_{pp \rightarrow B^\pm X}$ is the measured B^\pm production cross section;
- $\epsilon_{pp \rightarrow B^\pm X}$ is the fiducial volume efficiency of this measurement;
- $\frac{f_q}{f_u}$ is the ratio of hadronisation fractions for the considered type of B meson decay and B^\pm , for which the production cross section is measured;
- $\text{BR}(B_q \rightarrow X\mu^+ N)$ is the branching ratio of a B meson to HNL;
- $\text{BR}(N \rightarrow \mu^+ \pi^-)$ is the branching ratio of HNL to the considered final state;
- ϵ_{tot} is the total signal efficiency;
- index q corresponds to a single value of the u or c quark for the leptonic categories. For the semileptonic category, a sum over the q index is performed, where q belongs to the list of all the considered decays in Figure 4.3.

The $\frac{f_q}{f_u} \cdot \text{BR}(B_q \rightarrow X\mu^+ N) \cdot \text{BR}(N \rightarrow \mu^+ \pi^-)$ value is defined as a POI in this analysis, denoted by σ . Therefore, the signal yield in the PDF, see Section 4.7.3, needs to be re-expressed in terms of the new POI

$$N_{\text{sig}} = \mathcal{L} \cdot \frac{\sigma_{pp \rightarrow B^\pm X}}{\epsilon_{pp \rightarrow B^\pm X}} \cdot \sigma \cdot \epsilon_{\text{tot}}^i, \quad (4.29)$$

with ϵ_{tot}^i being the total reconstruction and selection efficiency of the search category i . This conveniently allows to include the systematic uncertainties in the integrated luminosity, production cross sections and fragmentation fractions into the calculation of the UL, as well as the uncertainties in the interpolated efficiencies values. Since these uncertainties are uncorrelated, this is done by constructing a single Gaussian constraint using the mean value and propagated uncertainty of the product

$$\mathcal{L} \cdot \frac{\sigma_{pp \rightarrow B^\pm X}}{\epsilon_{pp \rightarrow B^\pm X}} \cdot \epsilon_{\text{tot}}^i, \quad (4.30)$$

redefining the \mathcal{C}_{e_i} constraint in Equation (4.18). Now, since the total efficiency is a function of (m_N, τ_N) in this analysis, the likelihood for the fit minimisation is re-expressed as $\mathcal{L}_i(N_{\text{sig}}, \theta, m_N, \tau_N)$. To find the excluded UL on both $\text{BR}(B_q \rightarrow X\mu^+ N) \cdot \text{BR}(N \rightarrow \mu^+ \pi^-)$ and U_μ^2 , a scan in the τ_N dimension is performed as well, as described further.

4.7.6 U_μ^2 as a parameter of interest

In order to combine all the categories presented in this analysis, the U_μ^2 parameter is used as a shared POI. Similarly to Section 4.7.5, the N_{sig} value from Equation (4.28) is set as a normalisation parameter to the signal PDF for each category, and in this way, the U_μ^2 becomes a common parameter in the fit. In our definitions, $\frac{f_q}{f_\mu} \cdot \text{BR}(B_q \rightarrow X\mu^+ N) \cdot \text{BR}(N \rightarrow \mu^+ \pi^-)$ is a function of U_μ^2 , precisely $f(U_\mu^2, m_N)$, and $\varepsilon_{\text{tot}}^i$ is $g(U_\mu^2, m_N)$. This can be used to rewrite the signal yield as

$$N_{\text{sig}}^i = \mathcal{L} \cdot \frac{\sigma_{pp \rightarrow B^\pm X}}{\epsilon_{pp \rightarrow B^\pm X}} \cdot f^i(U_\mu^2, m_N) \cdot g^i(U_\mu^2, m_N). \quad (4.31)$$

Due to the fact that the uncertainty on $\varepsilon_{\text{tot}}^i$ has to be included in the fit in form of a constraint, it becomes impossible to include the efficiency in the normalisation as a parameterised function $g^i(U_\mu^2, m_N)$. Therefore, the same technique is employed as in Section 4.7.7, by scanning UL for multiple lifetimes (i.e. couplings), setting fixed $U_\mu^2(\text{tested})$ in $g^i(U_\mu^2, m_N)$ and extracting $U_\mu^2(\text{measured})$ from $f^i(U_\mu^2, m_N)$. The excluded limit is then computed by profiling the $\frac{U_\mu^2(\text{measured})}{U_\mu^2(\text{tested})}$ fraction for each mass as it is shown in Figure 4.46. This procedure has the following list of free parameters:

- U_μ^2 is a POI, shared among all bins;
- N_{comb}^i and α_{comb}^i are the normalisation and the shape parameter of combinatorial background 4.15, free in each bin.

The fixed (constrained) parameters in that procedure are:

- The signal mass shape PDF $\mathcal{S}(m; \theta_S)$ from Section 4.7.1, where mean the m_N and shape parameters θ_S are fixed in each bin;
- The peaking background mass shape PDF from Section 4.6.2, where the mean μ_{peaking}^i and shape parameters $\theta_{\text{peaking}}^i$ are fixed to the values measured in Sec. 4.6;
- The peaking background normalisation N_{peaking}^i is constrained with the values measured in Section 4.6;
- The total efficiency $\varepsilon_{\text{tot}}^i$, which is a constrained parameter in each category with values of efficiency and its uncertainty for each $U_\mu^2(\text{tested})$, m_N point;
- $\mathcal{L} \cdot \frac{\sigma_{pp \rightarrow B^\pm X}}{\epsilon_{pp \rightarrow B^\pm X}}$, which is a common parameter among all categories of the search, constrained to its mean value and uncertainty.

4.7.7 Scan in the HNL lifetime dimension and interpretation of the results

For each m_N , the σ value extracted from the fit depends on the lifetime τ_N used for the UL computation and is model independent. To interpret our results into the coupling-mass exclusion curve, which is a model-dependent result, several HNL lifetimes have been tested. At first, 30 U_μ^2 points in a range of $[10^{-3}, 10^{-5}]$ are defined, see Figure 4.46 (left), then they are transformed into τ_N values for the test using the code implementation of Ref. [24]. For

each tested U_μ^2 value, the UL on σ is calculated using the CL_s method. Then, a ratio of these extracted σ values from the data to the predicted ones is computed, using [24], and is plotted as a function of the tested U_μ^2 , see Figure 4.46 (right). Zones where our tested value is equal to or below the predicted one are corresponding to excluded U_μ^2 . This procedure is repeated for each tested m_N value and is summarised further. The mass shape and peak position parameters are fixed in the fitting procedure, while the nuisance parameters, such as combinatorial background normalisation and shape parameters, are set free.

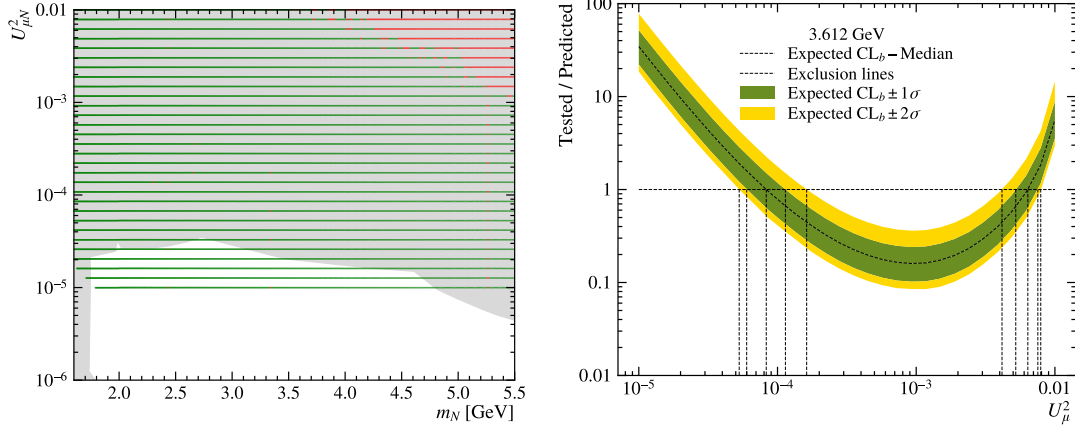


Figure 4.46 – (left) HNL U_μ^2 coupling-mass plane with the values tested in this analysis marked by green points, and points that are out of sensitivity reach or marked by red. (right) Plot of the exclusion strength, $\sigma_{\text{tested}}/\sigma_{\text{predicted}}$, as a function of U_μ^2 for $m_N = 3.612$ GeV of the exclusiveBu, SS, long category.

4.7.8 Generation of pseudoexperiments

Background parameterisation

In order to test for the possible biases in the bump hunt procedure and to evaluate systematic uncertainty due to the fit technique, generation of pseudoexperiments, or so-called toys, is required. At first, for a certain m_N value, a blind fit to data using the PDF defined in Section 4.7.3 is performed. Then, after fixing all parameters to the ones extracted in the fit, this PDF is used to randomly draw events from it in order to generate our toy data sets. Number of toy events is a random number generated according to a Poisson distribution with mean equal to the aforementioned PDF normalisation. A likelihood function construction for each pseudoexperiment and the fit procedure to the toy data-set are following exact same strategy as it is outlined in Section 4.7.3. To catch the biases and evaluate systematic uncertainty due to the choice of the combinatorial background shape, toys are generated using the default PDF (exponential) and then fit with and alternative one (linear).

In this study, an arbitrary number of signal events ($\sigma_{inj} > 0$), which is of the order of our sensitivity, is injected into the spectrum using parameterised signal from Section 4.7.1. Then,

4.7. Search for the signal peak in the invariant mass spectrum

for every 10th mass point of our search, 200 pseudoexperiments are performed and the σ_{fit} is extracted. Finally, pull distributions, $(\sigma_{\text{fit}} - \sigma_{\text{inj}})/\varepsilon_{\sigma_{\text{fit}}}$, are fit with a Gaussian PDF (see Figure 4.47) for each studied mass.

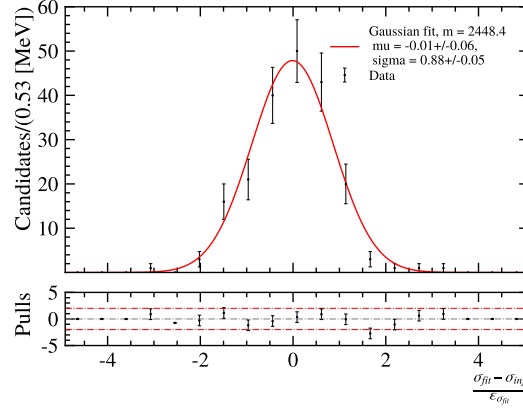


Figure 4.47 – Fit to the pull distribution of 200 pseudoexperiments with $m_N = 2448.4$ MeV of the leptonic Bu, SS, long category. It corresponds to a study with $\sigma_{\text{inj}} > 0$.

Results of this study are shown in Figure 4.48 where the results of fit to the pull distributions are plotted for each tested mass. Distributions of the mean values are showing no bias in the fit and UL computation and therefore no additional systematic uncertainty is assigned to the fit procedure. The same study is used to estimate the systematic uncertainty in choice of the background shape where pulls of $(\sigma_{\text{fit}} - \sigma_{\text{inj}})/\sigma_{\text{inj}}$ value are studied for each mass and showing an average deviation of 2% which is assigned as the value systematic uncertainty in background parameterisation.

Signal parameterisation

The same approach using pseudoexperiments is used to estimate systematic uncertainties caused by the mismodelling of the signal shape parameters. Signal parameterisation extracted from the fits to MC simulation shown in Figure 4.42 describes very well the $\mu\pi$ invariant mass spectra. Despite a good fit quality, parameters of the model in Equation 4.14 are determined with a certain level of precision and therefore the influence of this effect on the final result is studied.

To estimate this contribution, 150 toy experiments were performed for each simulated mass sample. The bump hunt procedure described in Section 4.7.6 was then repeated with the signal model parameters randomly drawn from a multivariate normal distribution. This distribution is constructed using the mean values and covariance matrices of parameters of Equation 4.14 extracted from the fit to each m_N . Same pull distributions of $(\sigma_{\text{fit}} - \sigma_{\text{inj}})/\sigma_{\text{inj}}$ mentioned above are used to analyse the deviation of POI values. An average deviation of 5.9% among all masses is found and assigned as systematic uncertainty in signal mismodeling.

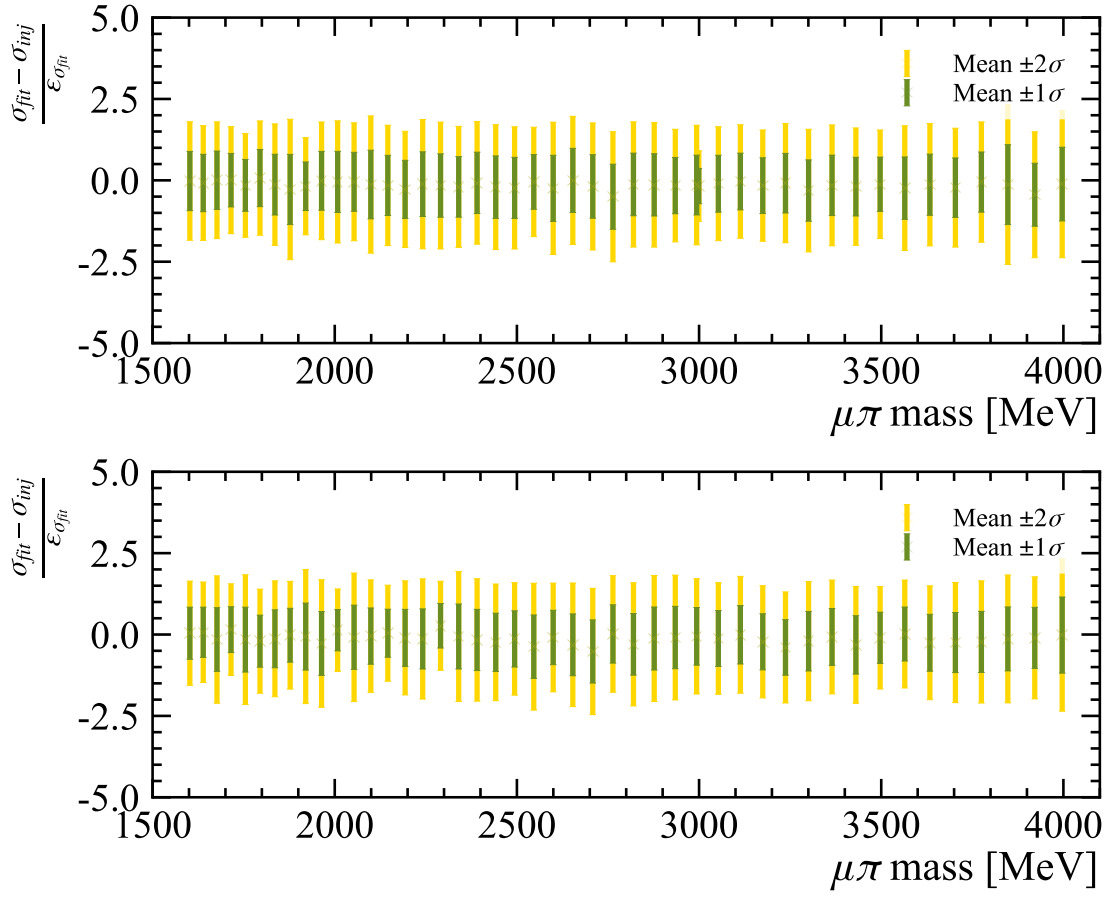


Figure 4.48 – Results of the pseudoexperiments for the combined SS (top) and OS (bottom) categories. For each tested m_N central value and $\pm 1, 2\sigma$ bands of the pull distributions are shown. Result for the study with $\sigma_{\text{inj}} > 0$ indicates no strong deviations and therefore no biases in the fit procedure.

4.8 Expected sensitivity

Results of this search are presented in the excluded $U_\mu^2 - m_N$ plane using the method described before. Currently, the observed values of the limit are blinded and will be published shortly after the collaboration review. Nevertheless, even the expected limits curve is enough to draw some conclusions about the final sensitivity of this analysis. No bias in the bump hunt procedure was observed as the study with pseudoexperiments shows. The range of studied HNL masses goes from 1.6 to 5.5 GeV. The exclusion curve of the leptonic Bc category, which has the widest phase space in mass, reaches only approximately up to 5 GeV due to the loss of the sensitivity in that range, although higher masses are tested as well. This can be explained by an example of the exclusion strength curve (as the one in Figure 4.46, right) that does not cross the exclusion boundary.

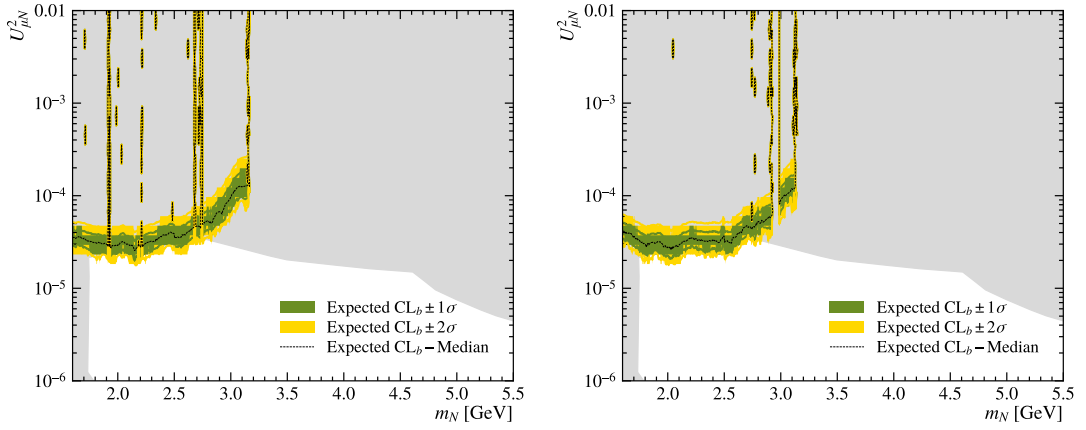


Figure 4.49 – (left) SS and (right) OS semileptonic category expected exclusion in the the U_μ^2 versus m_N parameter space. Grey area is excluded by previous experiments.

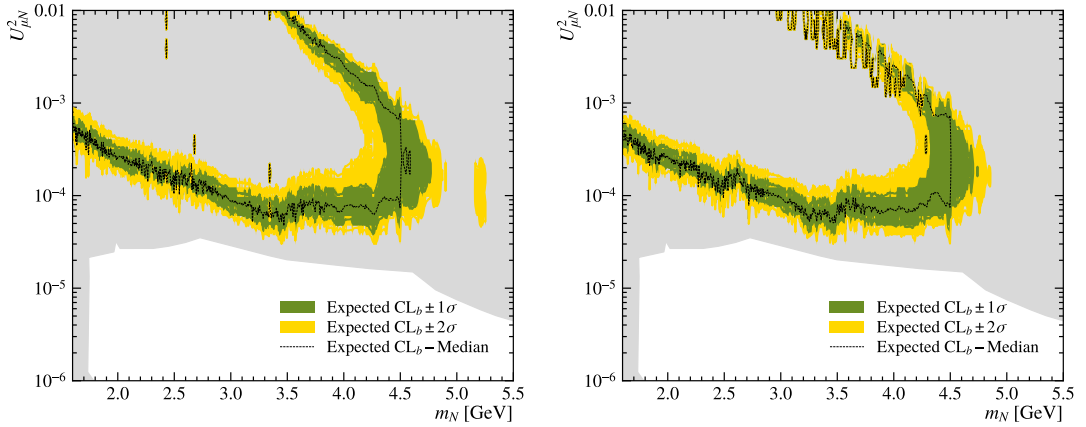


Figure 4.50 – (left) SS and (right) OS Bc category expected exclusion in the the U_μ^2 versus m_N parameter space.

In order to evaluate the overall region excluded by all the considered categories in this analysis,

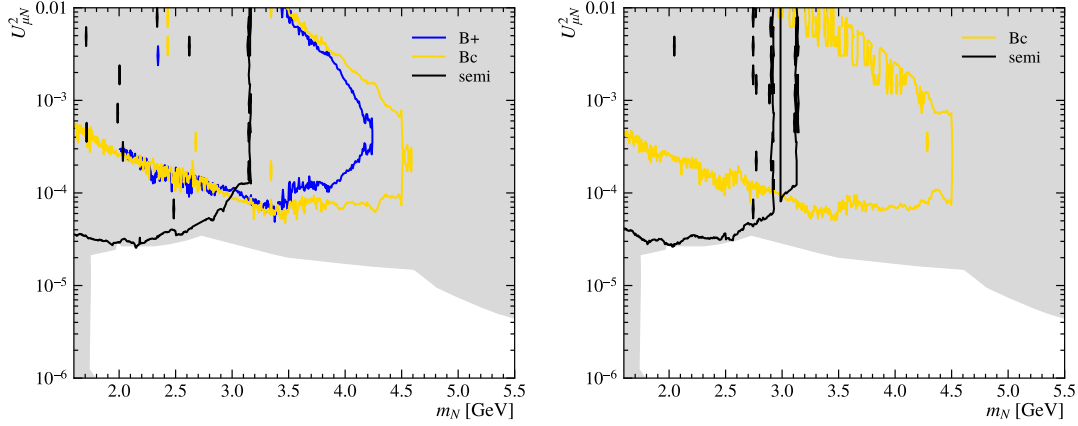


Figure 4.51 – All expected limits overlaid for (left) SS and (right) OS categories.

an additional procedure was developed as explained in Section 4.7.6. The resulting exclusion regions are shown in Figure 4.52 for the SS and OS categories together with the excluded regions by all the other searches outlined in Section 1.3. Interpretation of the OS category corresponds to the Dirac-like HNL scenario. The evaluation of the Majorana-like case requires a statistical combination of the SS and OS categories and is outlined further.

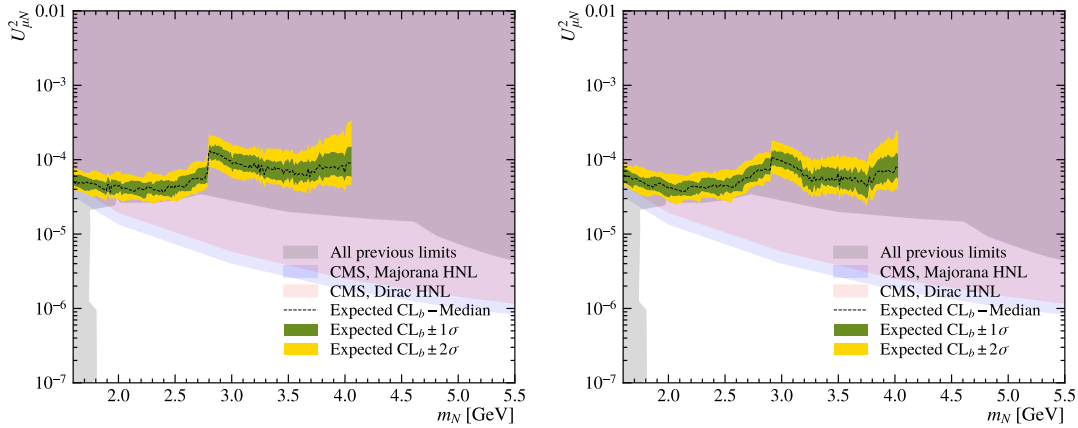


Figure 4.52 – Left, combination of all the SS hunt categories: semileptonic LL, semileptonic DD, leptonic Bu LL and leptonic Bc LL. Right, combination of all the OS hunt categories: semileptonic LL, leptonic Bu LL and leptonic Bc LL.

4.8.1 Blinded results of Majorana and Dirac scenarios interpretation

In case of Dirac-like HNL, the interpretation is identical to the one obtained with the OS category shown in Figure 4.53, right. For the Majorana-like case, the HNL can decay to both the OS and SS final states and it does so with equal branching fraction. The HNL total natural width is therefore doubled in the Majorana case and as a consequence its lifetime is halved

and its branching ratio to the OS final state is also halved with respect to the Dirac-like case. A simultaneous hunt for Majorana-like HNLs in both the SS and OS categories was performed, where the lifetime and the BR obtained for the Dirac-like case was halved. The result of this combination is shown in Figure 4.53, right. The limit for the Majorana neutrino is stronger as this case includes all the sensitive categories of the search and the lifetime modification shifts the signal efficiency towards higher values.

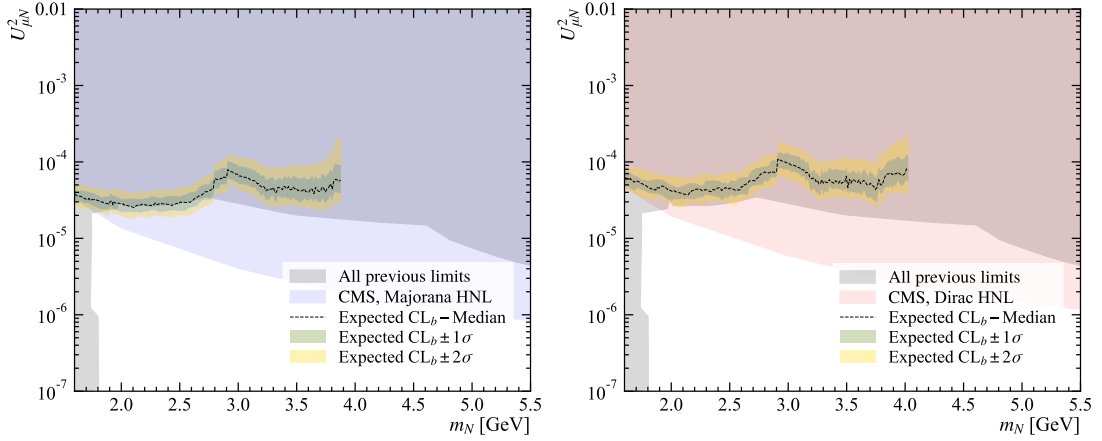


Figure 4.53 – (Left) Combination of all the SS and OS hunt categories that corresponds to Majorana HNL. (Right) Combination of all the OS hunt categories that corresponds to Dirac HNL. *Limits of the previous results indicated in grey are not adjusted for the Dirac and Majorana cases.

4.9 Uncertainties summary

Systematic uncertainties arise from uncertainties associated with the measurement method, assumptions made by the experimenter, and the model used to describe the observed data. Sources of these systematics relevant for this analysis are outlined in this chapter.

4.9.1 Integrated luminosity

Luminosity is computed in Section 4.3.1 and uncertainty of 2% is assigned according to the recommendations. This value is directly taken into account in the computation of the final result in Section 4.7.5.

4.9.2 $\sigma_{pp \rightarrow X_b} \cdot \text{BR}(B_q \rightarrow X\mu^+ N)$ calculation

In Section 4.5 and 4.7.5, when computing the number of expected signal events in the selected data sample using Equation (4.1), the uncertainty in cross section, $\sigma(pp \rightarrow B^\pm) = (86.6 \pm 6.4) \mu\text{b}$ [73], and in the ratios of fragmentation fractions, $f_s/f_u = 0.244 \pm 0.012$ [74] and $f_c/f_u = (2.61 \pm 0.62) \times 10^{-3}$ [72] are included.

4.9.3 Signal efficiency

For the efficiency interpolation only statistical uncertainty is taken into account and propagated by running 5000 toy fits for each point, as described in Section 4.5.3. Systematic uncertainties are computed for the following list of efficiency components:

Trigger efficiency correction

No additional systematic uncertainty on the L0 correction procedure, only statistical uncertainty on correction weights described in Sec. 4.5.4 that are taken into account when computing the total efficiency and its uncertainty.

GEC correction

As discussed in Section 4.5.4, 10% systematic uncertainty is assigned, which is included in the final result in Section 4.7.5 as well.

PID correction

Our corrected distributions shown in Section 4.5.4 using standard and alternative templates are very similar. The efficiency of all PID requirements using these alternative templates stays within 0.5% of the default one. Therefore, no additional systematic uncertainty assigned due

to this procedure.

Implementation

All the factors discussed above are directly taken into account when calculating the UL on $\text{BR}(B_q \rightarrow X\mu^+N) \cdot \text{BR}(N \rightarrow \mu^+\pi^-)$ in form of a Gaussian constraints terms in the likelihood function, as explained in Section 4.7.5. Current limits are produced with the luminosity, cross section, interpolated efficiency uncertainty and GEC-related uncertainty.

4.9.4 PDFs parameterisation

In order to evaluate systematic uncertainties in the signal and background parameterisation the pseudoexperiments are used. It is done following the procedure described in Section 4.7.8. Then, the UL on $\text{BR}(B_q \rightarrow X\mu^+N) \cdot \text{BR}(N \rightarrow \mu^+\pi^-)$ is computed for the PDF used to generate toy data sets and for each toy experiments. The average deviation of the observed upper limit with respect to the one obtained from original distribution is assigned as a systematic uncertainty.

Signal parameterisation

A systematic uncertainty of 5.9% is assigned due to the signal shape mismodelling, which is evaluated in Section 4.7.8 by generating toys with variations of the parameters of the signal model following a multivariate normal distribution with the mean and the covariance matrices obtained from the fit to MC samples.

Background parameterisation

A systematic uncertainty of 2% is assigned due to the choice of the combinatorial background PDF, which is evaluated in Section 4.7.8 by generating toys with the default function and fitting with the alternative one (see Section 4.7.2). Contribution for statistical uncertainty in the peaking background parameterisation is already taken into account in the likelihood function (as a Gaussian-constrained term in the likelihood).

The dominant systematic uncertainty is on the GEC selection efficiency which is not well reproduced in the official LHCb simulation and required a custom method of evaluation for this analysis. It can be improved in the future searches with introduction of the control channel to the analysis in order to cancel out shared systematics.

5 Conclusions and outlook

The Standard Model is a great success of the high energy particle physics. To date it described almost all phenomena observed in this physics domain and those events that cannot be accommodated or contradict to it hint for a physics beyond of the reach of this theory. Additionally to already existing, multiple dedicated experiments are being built or designed with intention to hunt for new physics or improve already measured pieces of the SM. In that scope, the LHC experiments have undergone one of the previewed upgrades allowing for higher sensitivity and precision, which is leading to the further reach in yet untested regions of the BSM. Part of this thesis work was dedicated to the upgrade of the LHCb experiment, which was a unique opportunity to contribute to the development, commissioning and operation of the PLUME luminometer that successfully operates during the data-taking of the LHCb detector. The major part of this thesis was dedicated to the search for hypothetical right-handed neutrinos that do not interact via any of the fundamental interactions of the SM and can provide a minimal solution to several outstanding problems in particle physics. This search was performed using the data of the proton-proton collisions at the LHC collected by the LHCb detector during the Run 2 period, looking for a particle with unknown mass, m_N , and lifetime, τ_N . Current blinded results are presented in a form where the expected background-like yields are interpreted as the model-dependent limit on the mixing parameter $|U_\mu|^2$ between HNL and the left-handed muon neutrino. This search focused on the on-shell heavy neutral leptons produced inclusively in B decays. It improved greatly the LHCb sensitivity to HNL that was obtained in [32] using $B^+ \rightarrow \mu^+ N (\rightarrow \mu^+ \pi^-)$ decays, and it includes both the LNV and LNC decay channels and most importantly makes use of HNLs produced inclusively from semileptonic B decays or in leptonic B^+ as well as B_c^+ decays. Expected limits surpass the previous LHCb sensitivity to the mixing parameter between the HNL and the muon neutrino U_μ^2 by more than one order of magnitude. Moreover, the result is competitive with the world-best limit coming from the CMS experiment for the HNL mass around 2 GeV, with possible future improvements beyond luminosity scaling thanks to the use of partially reconstructed HNL decays and the use of vertices downstream of the VELO detector. Additionally, several key features were studied and developed that will help for the future searches of this kind to reach the new levels of sensitivity to the potential discoveries.

A Additional figures and tables

This appendix includes additional material mentioned in the thesis.

A.1 HLT efficiency tables

These tables are evaluated on concatenation of 100 and 1000 ps MC samples for the cross-check and illustration purposes. When evaluating MC efficiency for the computation of the final results on mass and lifetime grid, it is done per single mass/lifetime point.

Table A.1 – HLT1 efficiency obtained for the different SS categories of MC samples with different HNL mass. HLT1 efficiency is provided in % with the statistical uncertainty evaluated in MC simulation with L0 requirement applied. LL and DD stand for the long-long and downstream-downstream combination of the $\mu\pi$ tracks, respectively.

| m_N , GeV | semileptonic LL | semileptonic DD | leptonicBu LL | leptonicBc LL |
|-------------|------------------|------------------|------------------|------------------|
| 1.6 | 88.23 ± 0.21 | 58.91 ± 0.34 | 93.41 ± 0.16 | 89.08 ± 0.29 |
| 2.0 | 90.18 ± 0.2 | 53.42 ± 0.4 | 94.47 ± 0.11 | 91.75 ± 0.09 |
| 3.0 | 93.46 ± 0.27 | 44.0 ± 0.79 | 95.51 ± 0.12 | 93.23 ± 0.07 |
| 4.0 | 94.35 ± 0.27 | 45.77 ± 1.03 | 95.65 ± 0.13 | 94.91 ± 0.07 |
| 5.0 | | | 93.41 ± 0.43 | 95.41 ± 0.08 |
| 5.5 | | | | 94.56 ± 0.08 |

Appendix A. Additional figures and tables

Table A.2 – HLT2 efficiency obtained for the different SS categories of MC samples with different HNL mass. HLT2 efficiency is provided in % with the statistical uncertainty evaluated in MC simulation with L0 and HLT1 requirements applied. LL and DD stand for the long-long and downstream-downstream combination of the $\mu\pi$ tracks, respectively.

| m_N , GeV | semileptonic LL | semileptonic DD | leptonicBu LL | leptonicBc LL |
|-------------|------------------|------------------|------------------|------------------|
| 1.6 | 24.01 ± 0.3 | 19.98 ± 0.36 | 27.51 ± 0.29 | 34.96 ± 0.47 |
| 2.0 | 34.38 ± 0.33 | 19.98 ± 0.44 | 36.38 ± 0.23 | 47.65 ± 0.17 |
| 3.0 | 76.75 ± 0.48 | 19.92 ± 0.96 | 72.08 ± 0.26 | 77.19 ± 0.12 |
| 4.0 | 90.93 ± 0.34 | 20.0 ± 1.22 | 88.14 ± 0.22 | 89.05 ± 0.1 |
| 5.0 | | | 97.98 ± 0.25 | 94.54 ± 0.08 |
| 5.5 | | | | 96.43 ± 0.07 |

A.2 MVA efficiencies

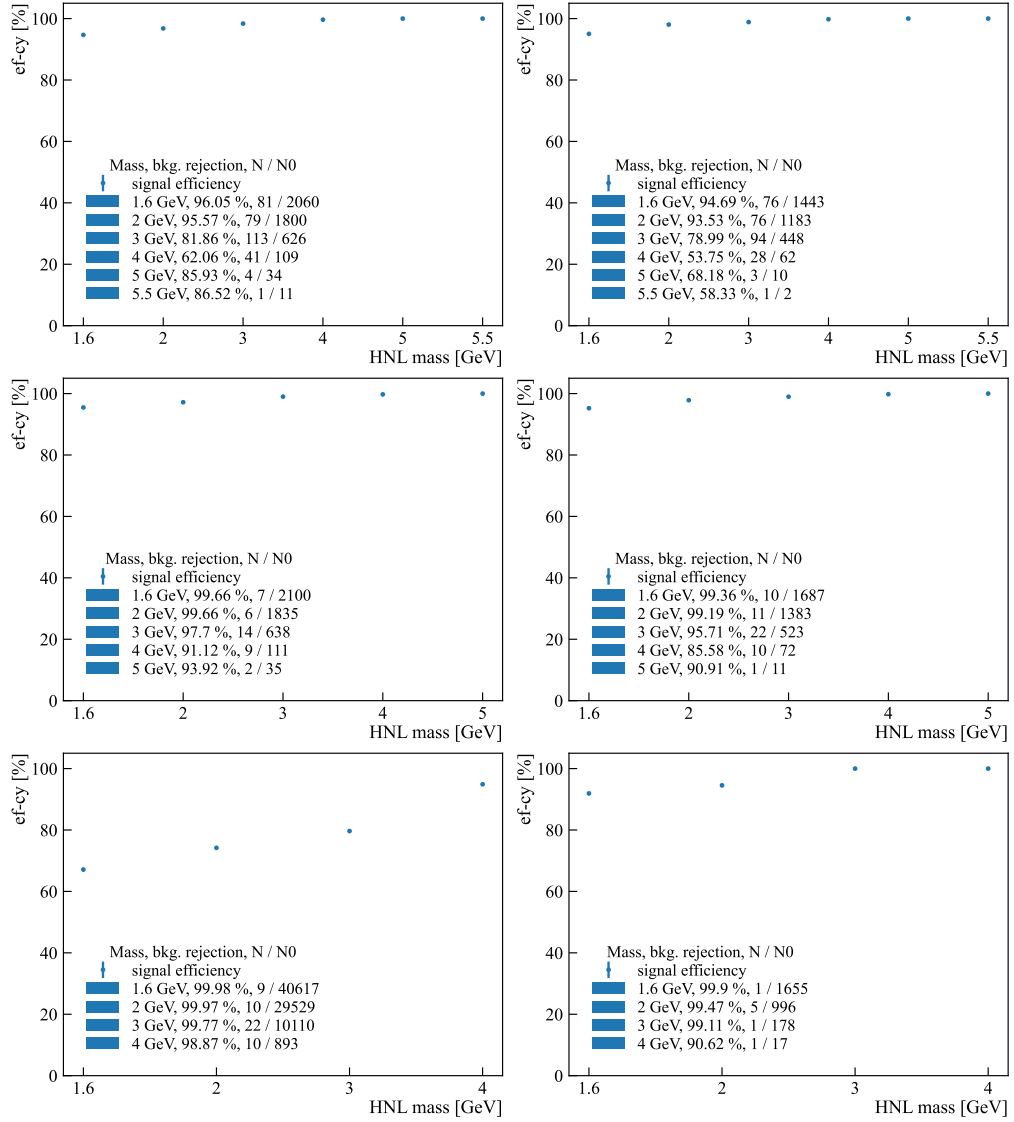


Figure A.1 – Categories names are in the following order: leptonic B_c , OS, long; leptonic B_c , SS, long; leptonic B_u , OS, long; leptonic B_u , SS, long; semileptonic, OS, long and semileptonic, SS, downstream categories

A.3 2D efficiency maps

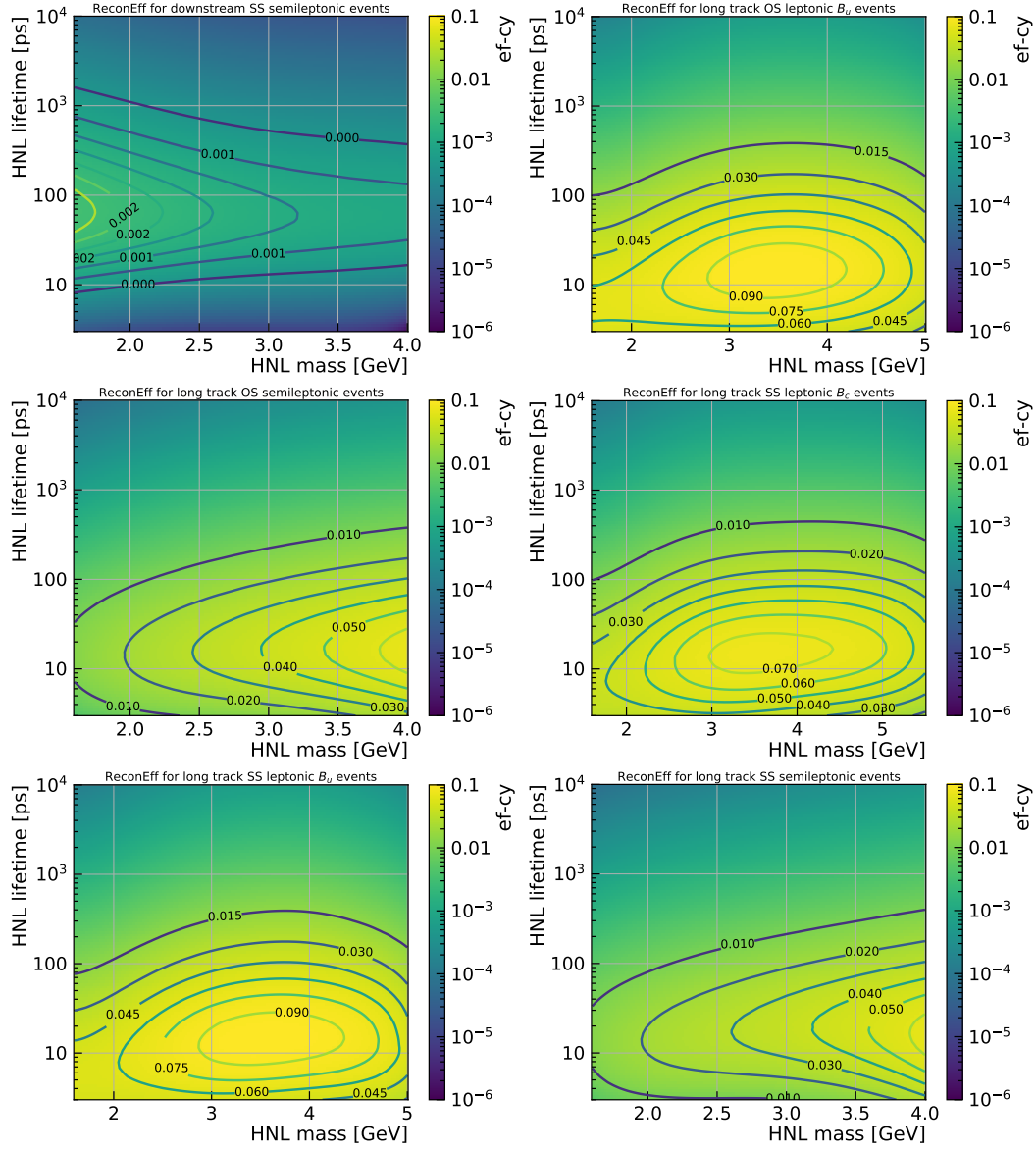
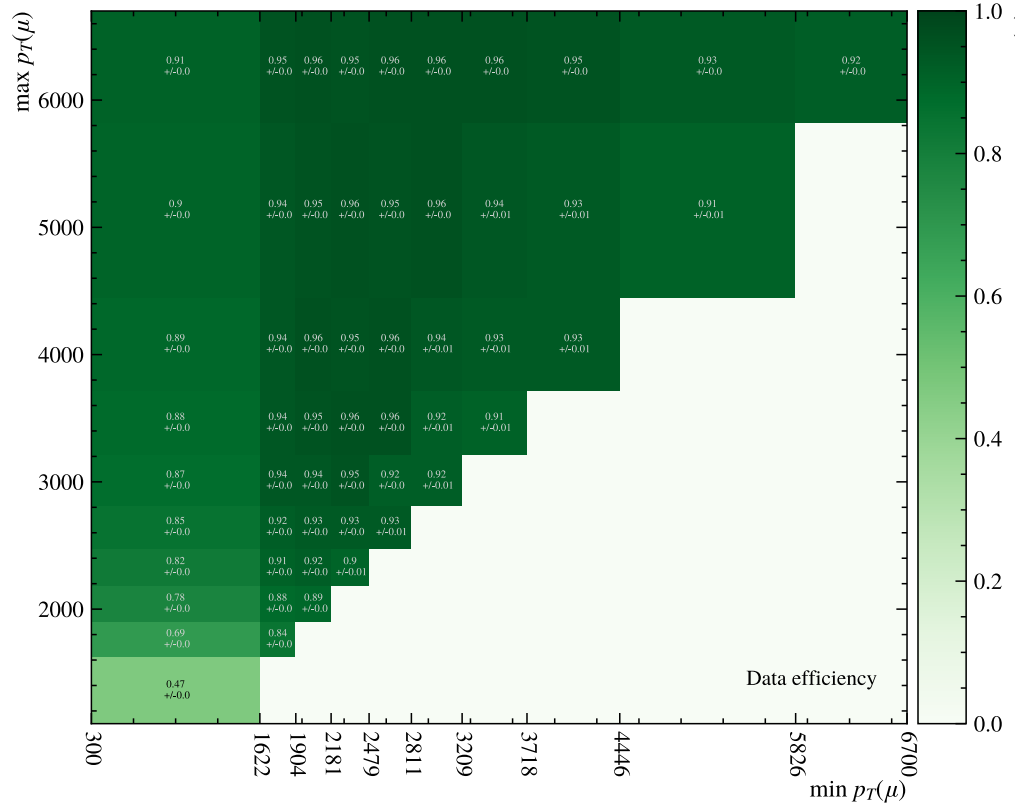


Figure A.2 – 2D efficiencies as a function of m_N and τ_N . Category names are in the figure titles.

A.4 2D L0 correction maps

Figure A.3 – 2D TIS-TOS efficiencies, $\varepsilon_{L0}^{\text{Data}}$, in data. The last p_T bin includes overflow.

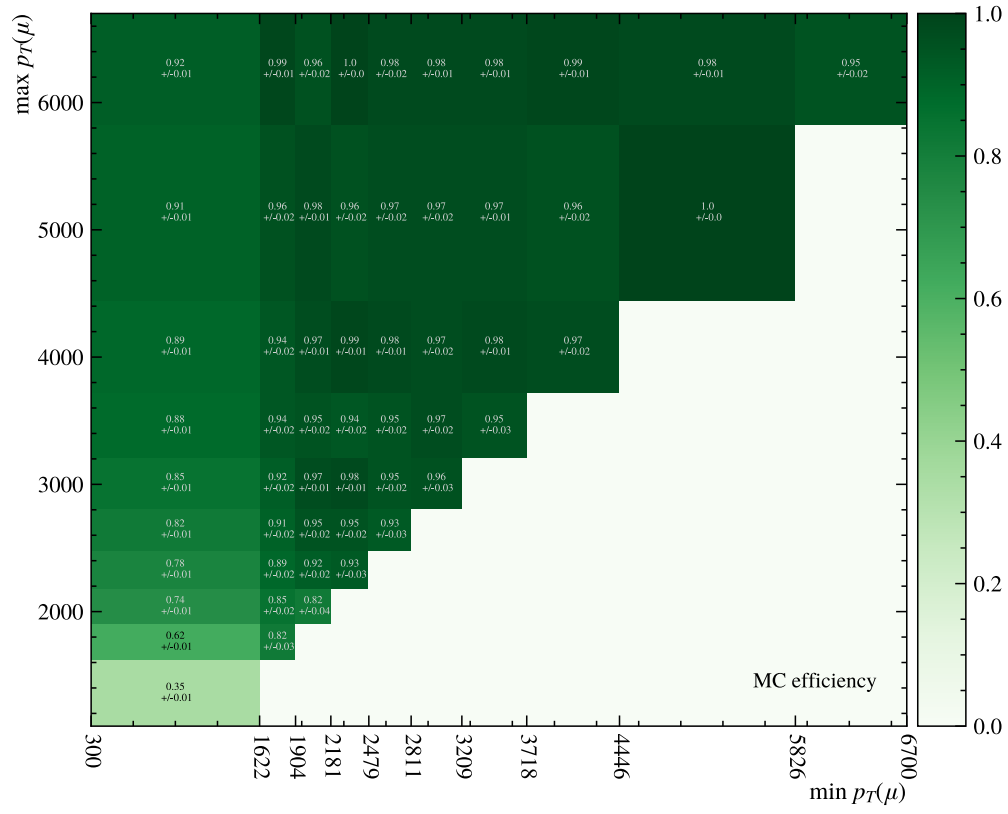


Figure A.4 – 2D TIS-TOS efficiencies, $\epsilon_{10}^{\text{MC}}$, in MC simulation. The last p_T bin includes overflow.

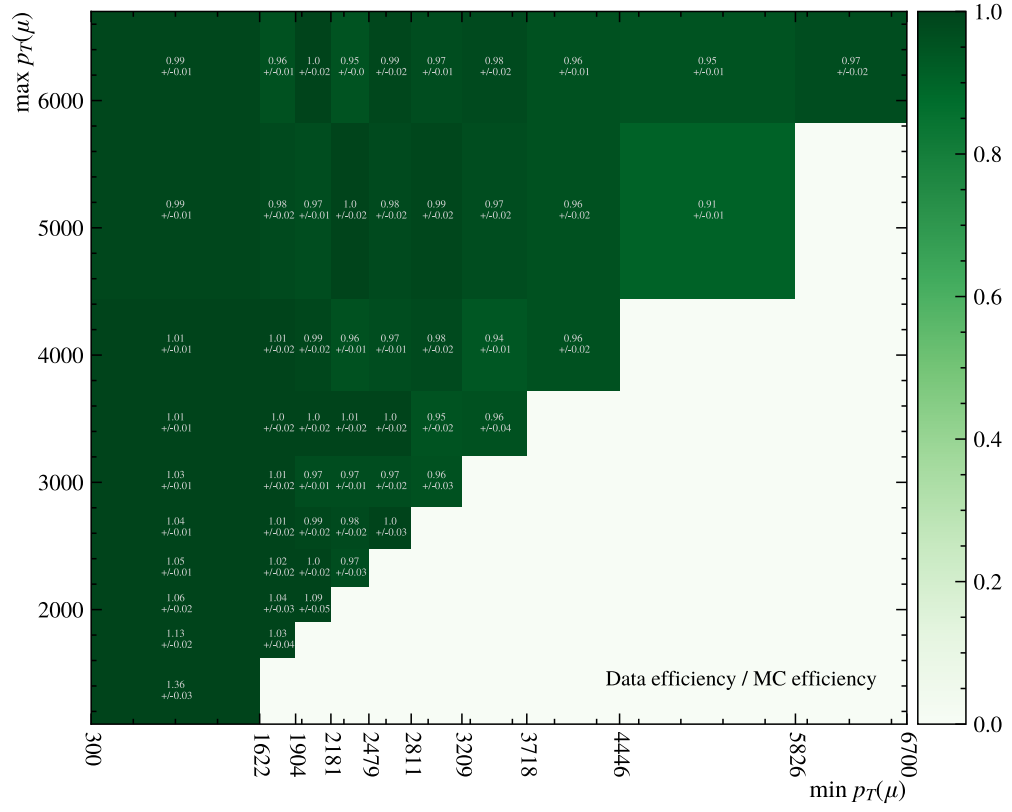


Figure A.5 – 2D TIS-TOS corrections w_{L0} . The last p_T bin includes overflow.

A.5 Mass fits

Figures in this Appendix report the HNL invariant mass fits in all the analysis categories.

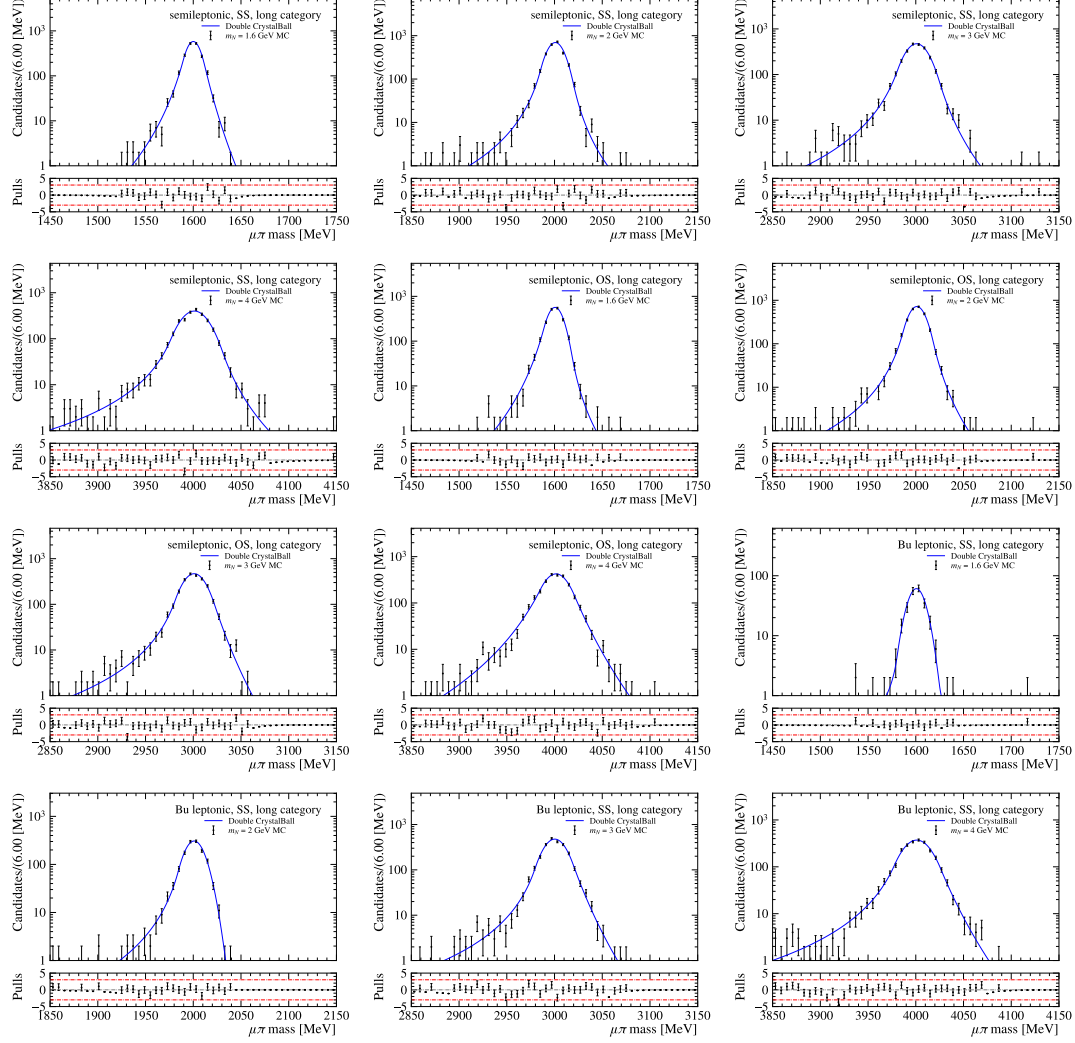


Figure A.6 – HNL MC mass fits

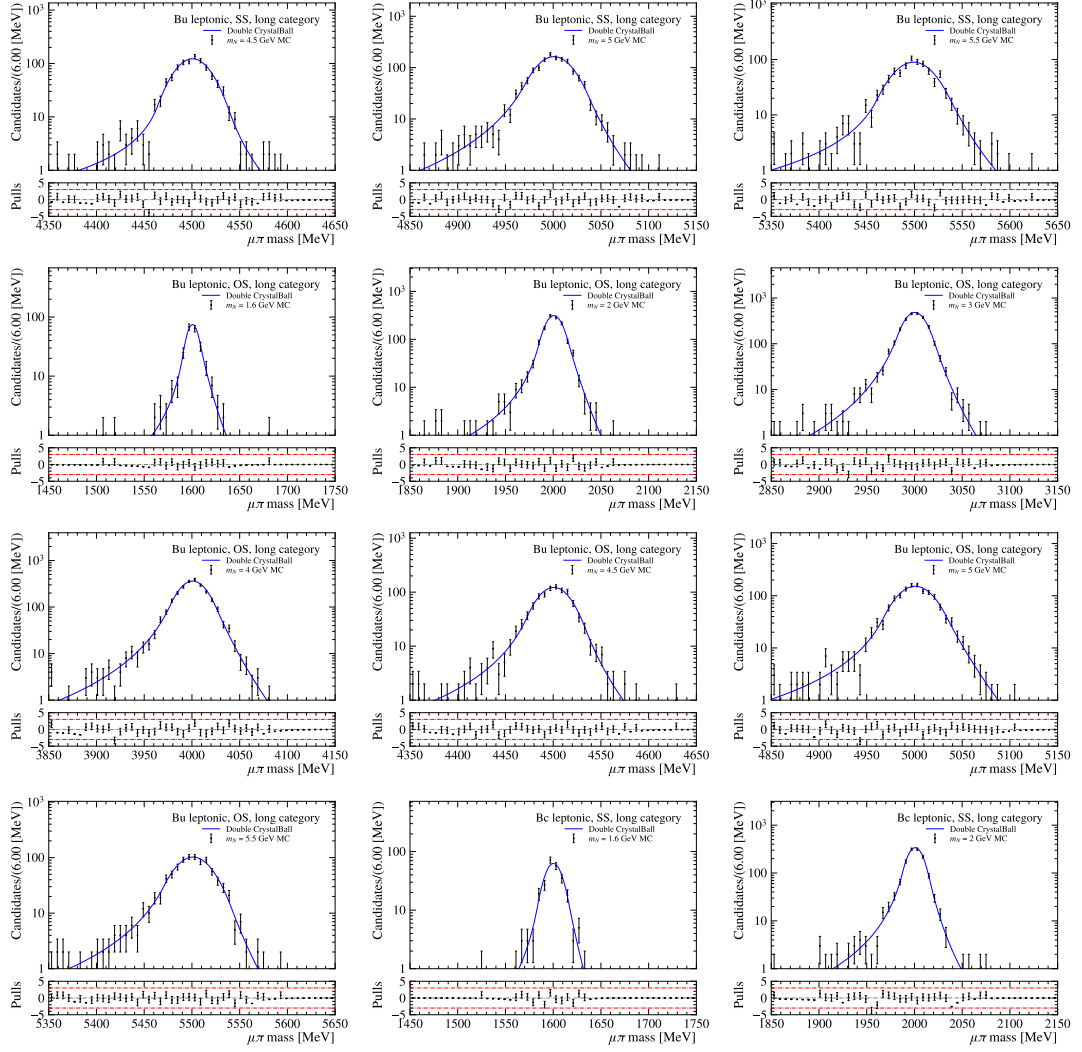


Figure A.7 – HNL MC mass fits

Appendix A. Additional figures and tables

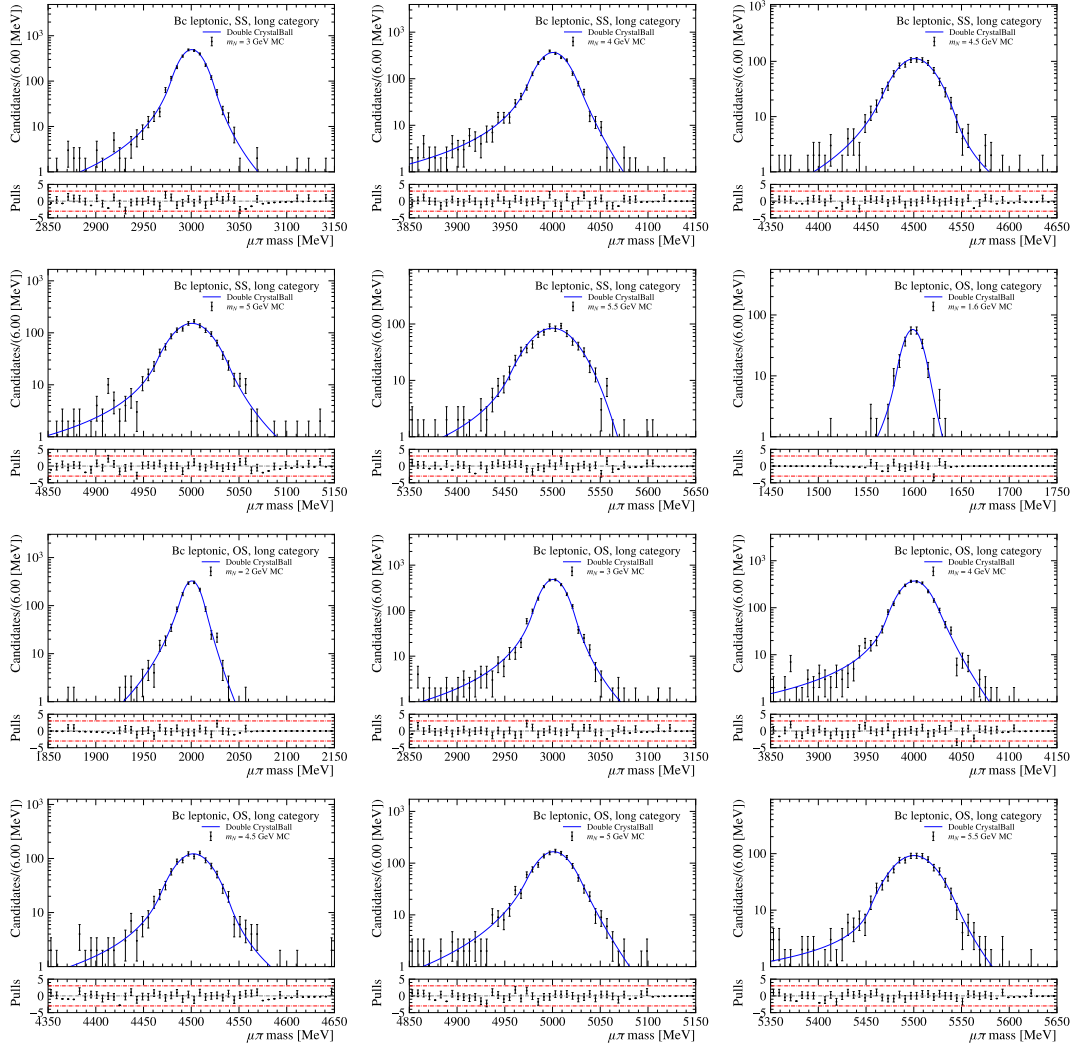


Figure A.8 – HNL MC mass fits

Bibliography

- [1] S. L. Glashow, *Partial-symmetries of weak interactions*, Nuclear Physics **22** (1961) 579.
- [2] S. L. Glashow, J. Iliopoulos, and L. Maiani, *Weak interactions with lepton-hadron symmetry*, Phys. Rev. D **2** (1970) 1285.
- [3] S. Abdus, *Weak and electromagnetic interactions*, doi: <https://doi.org/10.1142/9789812795915-0034> arXiv: <https://www.worldscientific.com/doi/pdf/10.1142/9789812795915-0034>.
- [4] S. Weinberg, *A model of leptons*, Phys. Rev. Lett. **19** (1967) 1264.
- [5] F. Englert and R. Brout, *Broken symmetry and the mass of gauge vector mesons*, Phys. Rev. Lett. **13** (1964) 321.
- [6] G. A. et al, *Observation of a new particle in the search for the standard model higgs boson with the ATLAS detector at the LHC*, Physics Letters B **716** (2012) 1.
- [7] S. C. et al, *Observation of a new boson at a mass of 125 GeV with the CMS experiment at the LHC*, Physics Letters B **716** (2012) 30.
- [8] W. Bonivento *et al.*, *Proposal to Search for Heavy Neutral Leptons at the SPS*, arXiv:1310.1762.
- [9] A. M. Abdullahi *et al.*, *The present and future status of heavy neutral leptons*, Journal of Physics G: Nuclear and Particle Physics **50** (2023) 020501.
- [10] Y. Fukuda *et al.*, *Evidence for oscillation of atmospheric neutrinos*, Physical Review Letters **81** (1998) 1562.
- [11] Q. R. Ahmad *et al.*, *Direct evidence for neutrino flavor transformation from neutral-current interactions in the sudbury neutrino observatory*, Physical Review Letters **89** (2002) .
- [12] Z. Maki, M. Nakagawa, and S. Sakata, *Remarks on the Unified Model of Elementary Particles*, Progress of Theoretical Physics **28** (1962) 870, arXiv: <https://academic.oup.com/ptp/article-pdf/28/5/870/5258750/28-5-870.pdf>.

Bibliography

- [13] I. Esteban *et al.*, *The fate of hints: updated global analysis of three-flavor neutrino oscillations*, Journal of High Energy Physics **2020** (2020) .
- [14] B. A. et al. *Long-baseline neutrino oscillation physics potential of the DUNE experiment*, The European Physical Journal C **80** (2020) .
- [15] Hyper-Kamiokande collaboration, K. Abe *et al.*, *Hyper-Kamiokande Design Report*, arXiv:1805.04163.
- [16] M. Aker *et al.*, *First direct neutrino-mass measurement with sub-eV sensitivity*, 2021.
- [17] S. Alam *et al.*, *Completed SDSS-IV extended baryon oscillation spectroscopic survey: Cosmological implications from two decades of spectroscopic surveys at the apache point observatory*, Physical Review D **103** (2021) .
- [18] T. Asaka, S. Blanchet, and M. Shaposhnikov, *The ν MSM, dark matter and neutrino masses*, Phys. Lett. B **631** (2005) 151, arXiv:hep-ph/0503065.
- [19] S. Dodelson and L. M. Widrow, *Sterile-neutrinos as dark matter*, Phys. Rev. Lett. **72** (1994) 17, arXiv:hep-ph/9303287.
- [20] A. Boyarsky *et al.*, *Sterile neutrino Dark Matter*, Prog. Part. Nucl. Phys. **104** (2019) 1, arXiv:1807.07938.
- [21] M. Fukugita and T. Yanagida, *Baryogenesis Without Grand Unification*, Phys. Lett. B **174** (1986) 45.
- [22] T. Asaka and M. Shaposhnikov, *The ν MSM, dark matter and baryon asymmetry of the universe*, Phys. Lett. B **620** (2005) 17, arXiv:hep-ph/0505013.
- [23] E. J. Chun *et al.*, *Probing Leptogenesis*, Int. J. Mod. Phys. A **33** (2018) 1842005, arXiv:1711.02865.
- [24] K. Bondarenko, A. Boyarsky, D. Gorbunov, and O. Ruchayskiy, *Phenomenology of GeV-scale Heavy Neutral Leptons*, JHEP **11** (2018) 032, arXiv:1805.08567.
- [25] T. Asaka, S. Blanchet, and M. Shaposhnikov, *The ν MSM, dark matter and neutrino masses*, Physics Letters B **631** (2005) 151.
- [26] NA3 collaboration, J. Badier *et al.*, *Mass and Lifetime Limits on New Longlived Particles in $300\text{-GeV}/c\pi^-$ Interactions*, Z. Phys. C **31** (1986) 21.
- [27] J. Dorenbosch *et al.*, *A search for decays of heavy neutrinos in the mass range 0.5–2.8 GeV*, Physics Letters B **166** (1986) 473.
- [28] Belle collaboration, D. Liventsev *et al.*, *Search for heavy neutrinos at Belle*, Phys. Rev. D **87** (2013) 071102, arXiv:1301.1105, [Erratum: Phys.Rev.D 95, 099903 (2017)].

-
- [29] DELPHI collaboration, P. Abreu *et al.*, *Search for neutral heavy leptons produced in Z decays*, Z. Phys. C **74** (1997) 57, [Erratum: Z.Phys.C 75, 580 (1997)].
 - [30] ATLAS collaboration, G. Aad *et al.*, *Search for heavy neutral leptons in decays of W bosons produced in 13 TeV pp collisions using prompt and displaced signatures with the ATLAS detector*, JHEP **10** (2019) 265, arXiv:1905.09787.
 - [31] CMS collaboration, A. Tumasyan *et al.*, *Search for long-lived heavy neutral leptons with displaced vertices in proton-proton collisions at $\sqrt{s}=13$ TeV*, JHEP **07** (2022) 081, arXiv:2201.05578.
 - [32] LHCb collaboration, R. Aaij *et al.*, *Search for Majorana neutrinos in $B^- \rightarrow \pi^+ \mu^- \mu^-$ decays*, Phys. Rev. Lett. **112** (2014) 131802, arXiv:1401.5361.
 - [33] B. Shuve and M. E. Peskin, *Revision of the LHCb Limit on Majorana Neutrinos*, Phys. Rev. D **94** (2016) 113007, arXiv:1607.04258.
 - [34] ATLAS collaboration, ATLAS collaboration, *Search for heavy neutral leptons in decays of W bosons using a dilepton displaced vertex in $\sqrt{s}=13$ TeV pp collisions with the ATLAS detector*, arXiv:2204.11988.
 - [35] CMS collaboration, A. M. Sirunyan *et al.*, *Search for heavy neutral leptons in events with three charged leptons in proton-proton collisions at $\sqrt{s}=13$ TeV*, Phys. Rev. Lett. **120** (2018) 221801, arXiv:1802.02965.
 - [36] CMS collaboration, A. M. Sirunyan *et al.*, *Search for heavy Majorana neutrinos in same-sign dilepton channels in proton-proton collisions at $\sqrt{s}=13$ TeV*, JHEP **01** (2019) 122, arXiv:1806.10905.
 - [37] E. Mobs, *The CERN accelerator complex - August 2018. Complexe des accélérateurs du CERN - Août 2018*, , General Photo.
 - [38] CMS collaboration, S. Chatrchyan, *The cms experiment at the cern lhc*, Journal of Instrumentation **3** (2008) S08004.
 - [39] ATLAS collaboration, G. Aad, *The atlas experiment at the cern large hadron collider*, Journal of Instrumentation **3** (2008) S08003.
 - [40] ALICE collaboration, K. Aamodt, *The alice experiment at the cern lhc*, Journal of Instrumentation **3** (2008) S08002.
 - [41] LHCb collaboration, R. Aaij *et al.*, *The lhcb detector at the lhc*, Journal of Instrumentation **3** (2008) S08005.
 - [42] LHCb collaboration, C. Elsässer, *$b\bar{b}$ production angle plots*, .
 - [43] LHCb collaboration, R. Aaij *et al.*, *Lhcb detector performance*, Int. J. Mod. Phys. A **30** (2015) 1530022.

Bibliography

- [44] D. Jacquet and F. Follin, *Implementation and experience with luminosity levelling with offset beam*, 2014. doi: 10.5170/CERN-2014-004.183.
- [45] LHCb collaboration, R. Aaij, *Measurements of the b^+ , b_0 , b_s^0 meson and λ_b^0 baryon lifetimes*, Journal of High Energy Physics **2014** (2014) .
- [46] LHCb VELO group, R. Aaij *et al.* , *Performance of the LHCb vertex locator*, Journal of Instrumentation **9** (2014) P09007.
- [47] LHCbSiliconTrackerGroup, M. t. Tobin, *The LHCb Silicon Tracker*, Nucl. Instrum. Methods Phys. Res. , A **831** (2016) 174.
- [48] C. A. Beteta *et al.*, *Monitoring radiation damage in the LHCb tracker turicensis*, Journal of Instrumentation **15** (2020) P08016.
- [49] LHCb collaboration, B.-M. *et al.* *LHCb inner tracker: Technical Design Report*, Technical design report. LHCb, CERN, Geneva, 2002. revised version number 1 submitted on 2002-11-13 14:14:34.
- [50] LHCb collaboration, B.-M. *et al.* *LHCb outer tracker: Technical Design Report*, Technical design report. LHCb, CERN, Geneva, 2001.
- [51] A. A. A. Jr *et al.*, *Performance of the lhcb muon system*, Journal of Instrumentation **8** (2013) P02022.
- [52] C. D. Anderson, *The positive electron*, Phys. Rev. **43** (1933) 491.
- [53] C. Lippmann, *Particle identification*, Nucl. Instrum. Methods Phys. Res. , A **666** (2011) 148, arXiv:1101.3276, 61 pages, 30 figures.
- [54] M. Adinolfi *et al.*, *Performance of the LHCb RICH detector at the LHC*, The European Physical Journal C **73** (2013) .
- [55] LHCb collaboration, *Trigger schemes*, <http://lhcb.web.cern.ch/lhcb/speakersbureau/html/TriggerScheme.html>.
- [56] S. Tolk, J. Albrecht, F. Dettori, and A. Pellegrino, *Data driven trigger efficiency determination at LHCb* , CERN, Geneva, 2014.
- [57] C. Bierlich *et al.*, *A comprehensive guide to the physics and usage of PYTHIA 8.3*, doi: 10.21468/SciPostPhysCodeb.8 arXiv:2203.11601.
- [58] C.-H. Chang, X.-Y. Wang, and X.-G. Wu, *BCVEGPY2.2: A newly upgraded version for hadronic production of the meson B_c and its excited states*, Comput. Phys. Commun. **197** (2015) 335, arXiv:1507.05176.
- [59] D. J. Lange, *The EvtGen particle decay simulation package*, Nucl. Instrum. Meth. **A462** (2001) 152.

-
- [60] N. Davidson, T. Przedzinski, and Z. Was, *PHOTOS interface in C++: Technical and physics documentation*, Comp. Phys. Comm. **199** (2016) 86, arXiv:1011.0937.
- [61] Geant4 collaboration, S. Agostinelli *et al.*, *Geant4: A simulation toolkit*, Nucl. Instrum. Meth. **A506** (2003) 250.
- [62] C. M. LHCb Collaboration, *LHCb PLUME: Probe for Luminosity MEasurement*, CERN, Geneva, 2021. doi: 10.17181/CERN.WLU0.M37F.
- [63] M. Schmelling, *Luminosity calibration for the leading bunch nobias-triggered data from the 2015 early measurement runs*, LHCb-INT-2017-015. CERN-LHCb-INT-2017-015, CERN, Geneva, 2017.
- [64] V. Balagura, *Van der Meer scan luminosity measurement and beam-beam correction*, The European Physical Journal C **81** (2021) .
- [65] LHCb collaboration, *Framework TDR for the LHCb Upgrade: Technical Design Report*, 2012.
- [66] S. Barsuk *et al.*, *Probe for Luminosity MEasurement in LHCb*, .
- [67] M. Brice, *LHCb beampipe and luminosity monitoring detectors near VELO*, , General Photo.
- [68] *Institute for scintillation materials national academy of sciences of ukraine*, .
- [69] G. Avoni *et al.*, *The new LUCID-2 detector for luminosity measurement and monitoring in ATLAS*, JINST **13** (2018) P07017.
- [70] H. Photonics, *Hamamatsu photonics*, 2021.
- [71] LHCb collaboration, *First absolute calibration of the PLUME online luminometer in Run 3*, .
- [72] LHCb collaboration, R. Aaij *et al.*, *Measurement of the B_c^- production fraction and asymmetry in 7 and 13 TeV pp collisions*, Phys. Rev. **D100** (2019) 112006, arXiv:1910.13404.
- [73] LHCb collaboration, R. Aaij *et al.*, *Measurement of the B^\pm production cross-section in pp collisions at $\sqrt{s} = 7$ and 13 TeV*, JHEP **12** (2017) 026, arXiv:1710.04921.
- [74] LHCb collaboration, R. Aaij *et al.*, *Measurement of b-hadron fractions in 13 TeV pp collisions*, Phys. Rev. **D100** (2019) 031102(R), arXiv:1902.06794.
- [75] The LHCb collaboration, *LHCb Luminosity Project*, 2023.
- [76] LHCb collaboration, R. Aaij *et al.*, *Precision luminosity measurements at LHCb*, JINST **9** (2014) P12005, arXiv:1410.0149.

Bibliography

- [77] LHCb collaboration, R. Aaij *et al.*, *Measurement of forward J/ψ production cross-sections in pp collisions at $\sqrt{s}=13$ TeV*, JHEP **10** (2015) 172, Erratum ibid. **05** (2017) 063, arXiv:1509.00771.
- [78] LHCb collaboration, R. Aaij *et al.*, *Measurement of the B_c^- meson production fraction and asymmetry in 7 and 13 TeV pp collisions*, Phys. Rev. D **100** (2019) 112006, arXiv:1910.13404.
- [79] LHCb collaboration, R. Aaij *et al.*, *Measurement of the B_c^- meson production fraction and asymmetry in 7 and 13 TeV pp collisions*, Phys. Rev. D **100** (2019) 112006, arXiv:1910.13404.
- [80] M. Williams, *Searching for a particle of unknown mass and lifetime in the presence of an unknown non-monotonic background*, Journal of Instrumentation **10** (2015) P06002.
- [81] G. Corti *et al.*, *Software for the LHCb experiment*, IEEE Trans. Nucl. Sci. **53** (2006) 1323.
- [82] R. Brun *et al.*, *Root-project: v6.18/02*, doi: 10.5281/zenodo.3895860.
- [83] H. Kolanoski, *Application of artificial neural networks in particle physics*, Nuclear Instruments and Methods in Physics Research Section A: Accelerators, Spectrometers, Detectors and Associated Equipment **367** (1995) 14, Proceedings of the 7th International Wire Chamber Conference.
- [84] A. Paszke *et al.*, *Pytorch: An imperative style, high-performance deep learning library*, in *Advances in Neural Information Processing Systems* 32, pp. 8024–8035. Curran Associates, Inc., 2019.
- [85] CDF Collaboration and D0 Collaboration, e. a. Aaltonen, *Evidence for a particle produced in association with weak bosons and decaying to a bottom-antibottom quark pair in higgs boson searches at the tevatron*, Phys. Rev. Lett. **109** (2012) 071804.
- [86] P. Baldi *et al.*, *Parameterized neural networks for high-energy physics*, Eur. Phys. J. C **76** (2016) 235, arXiv:1601.07913.
- [87] V. Nair and G. Hinton, *Rectified linear units improve restricted boltzmann machines*, *vinod nair*, **27**, 807–814, 2010.
- [88] Z. Zhang and M. R. Sabuncu, *Generalized cross entropy loss for training deep neural networks with noisy labels*, 2018.
- [89] D. P. Kingma and J. Ba, *Adam: A method for stochastic optimization*, 2017.
- [90] M. Balandat *et al.*, *Botorch: Programmable bayesian optimization in pytorch*, 2020.
- [91] G. Punzi, *Sensitivity of searches for new signals and its optimization*, 2003.

-
- [92] G. A. Cowan, D. C. Craik, and M. D. Needham, *RapidSim: An application for the fast simulation of heavy-quark hadron decays*, Computer Physics Communications **214** (2017) 239.
- [93] L. Sestini *et al.*, *Measurement of differential $b\bar{b}$ and $c\bar{c}$ cross sections in the forward region of pp collisions at $\sqrt{s} = 13$ TeV*, .
- [94] M. Pivk and F. R. L. Diberder, : *A statistical tool to unfold data distributions*, Nuclear Instruments and Methods in Physics Research Section A: Accelerators, Spectrometers, Detectors and Associated Equipment **555** (2005) 356.
- [95] N. L. Johnson, *Systems of frequency curves generated by methods of translation*, Biometrika **36** (1949) 149.
- [96] W. Buttinger, *ABCD Guide: A Practical Guide to the ABCD Method*, 2018.
- [97] A. L. Read, *Presentation of search results: The $CL(s)$ technique*, J. Phys. G **28** (2002) 2693.
- [98] M. Baak, S. Gadatsch, R. Harrington, and W. Verkerke, *Interpolation between multi-dimensional histograms using a new non-linear moment morphing method*, Nuclear Instruments and Methods in Physics Research Section A: Accelerators, Spectrometers, Detectors and Associated Equipment **771** (2015) 39.
- [99] J. Eschle, A. Puig Navarro, R. Silva Coutinho, and N. Serra, *zfit: Scalable pythonic fitting*, SoftwareX **11** (2020) 100508.
- [100] G. Cowan, K. Cranmer, E. Gross, and O. Vitells, *Asymptotic formulae for likelihood-based tests of new physics*, Eur. Phys. J. C **71** (2011) 1554, arXiv:1007.1727, [Erratum: Eur.Phys.J.C 73, 2501 (2013)].
- [101] L. Heinrich, *hepsoftwarefoundation/talks: Hsf community whiteboard*, 2019. doi: 10.5281/zenodo.3549838.
- [102] M. Marinangeli and A. Bay, *Search for long-lived particles decaying to $e\mu\nu$* , .

Serhii CHOLAK

16.01.1996, Ukraine
Route de Crochy 18
1024 Écublens VD
Switzerland
+4178805606
serhii.cholak@cern.ch



I did my Bachelor's and Master's studies in Kyiv, Ukraine, during which I had numerous opportunities to gain expertise in simulation, detector R&D and data analysis in HEP. Currently, I am a Ph.D. student at EPFL, doing my thesis on data analysis with LHCb, as well as keeping a strong interest and involvement in the detector instrumentation activities of our lab.

EDUCATION

| | |
|--------------------------|--|
| <i>06.2019 - present</i> | PhD student in Experimental Particle Physics <i>EPFL, Lausanne, High Energy Physics Laboratory (LPHE), Search for Heavy Neutral Leptons with LHCb, Thesis director: Lesya Shchutska</i> |
| <i>2017-2019</i> | Master in Physics <i>Taras Shevchenko National University, Kyiv, Ukraine Master Thesis: Simulation of the radiation shielding and parameters of detector systems in High Energy Physics.</i> |
| <i>2013-2017</i> | Bachelor in Physics <i>Taras Shevchenko National University, Kyiv, Ukraine Bachelor Thesis: The ProRad experiment. Importance of low momentum points in the proton radius measurement.</i> |

SKILLS AND COMPETENCES

Programming Languages

| | |
|----------------------------|-----------|
| <i>Advanced skills</i> | Python |
| <i>Intermediate skills</i> | C++, bash |
| <i>Basic skills</i> | Fortran |

HEP software

| | |
|----------------------------|---|
| <i>Advanced skills</i> | Zfit, ROOT, FLUKA, scikit-hep, hepstats |
| <i>Intermediate skills</i> | OPERA (EM simulation) |
| <i>Basic skills</i> | GEANT4, LabView |

Data analysis and ML software

| | |
|----------------------------|------------------------|
| <i>Advanced skills</i> | Pandas, NumPy, PyTorch |
| <i>Intermediate skills</i> | Tensorflow |

Languages

| | |
|----------------------|------------------|
| <i>Native tongue</i> | Ukrainian |
| <i>Fluent</i> | English, Russian |
| <i>Intermediate</i> | French |

INTERNSHIPS/RESEARCH EXPERIENCE

- 06.2019 - present* **PhD student in Experimental Particle Physics, EPFL**
- Development of the full analysis chain for the search of inclusively produced HNLs with LHCb data
 - Evaluation of the PETsys TOFPET2 ASIC SIPM Readout System in the SciFi detector prototype for the SND@LHC experiment: energy calibration, laser-based measurement of the time offset of each channel and coincidence time resolution.
 - Characterisation of prototypes for the PLUME detector in the beam tests and lab setups. Technical coordination of the PLUME detector and piquet duties during LHCb operation.
- 07.2018 - 09.2018* **CERN Summer Student Program**
- Development of the M2 beam line and EHN2 hall design in FLUKA for the radiation shielding studies
 - Preliminary simulation results for the radiation map of the 2018 high intensity hadron beam
- 02.2018 - 04.2018* **Master's project internship, IPNO, France**
- Energy resolution measurement of the BGO crystal using cosmic muons
 - Simulation of the energy deposition of cosmic muons in scintillator with GEANT4
- 07.2017 - 09.2017* **HGS-HIRe Summer Student Program at GSI, Germany**
- Study of the large aperture magnets assembly inaccuracy and simulation of induced field distortions
 - Field interference of large aperture magnets in the Collector Ring and its affects on beam dynamics
- 09.2016 - 11.2016* **Bachelor's project internship, IPNO, France**
- Simulation of the shielding and geometrical parameters of the ProRad experiment with FLUKA

TEACHING EXPERIENCES

- 2019 - present* **Teaching assistant in High Energy Physics Laboratory, EPFL**
- Supervision of a students laboratory course, individual analysis and group hardware projects.

TALKS AT SCHOOLS AND CONFERENCES

- 06.2022* **Annual meeting of Swiss Physical Society, Fribourg**
Inclusive search for HNLs at LHCb with Run 2 data
- 05.2022* **33rd Rencontres de Blois, France**
Probes of the Dark sector from the LHCb experiment
- 01.2022* **CHIPP winter school of particle physics, Switzerland**
Search for Heavy Neutral Leptons with LHCb
- 09.2021* **6th Summer School INFIERI, Madrid, Spain**
Evaluation of the PETsys TOFPET2 ASIC SIPM Readout System in the Scintillating Fibre Tracker (SciFi) prototype
- 07.2020* **6th Machine Learning in High Energy Physics summer school**
by Yandex School of Data Analysis, Lausanne, online